ATP- and voltage-dependent gating of P2X2 receptor analyzed by voltage-clamp fluorometry using fluorescent unnatural amino acid

Andriani, Rizki Tsari

SOKENDAI (The Graduate University for Advanced Studies)
School of Life Science
Departement of Physiological Sciences

2019

Table of Contents

Abbreviations 3
Summary 5
Introduction 8
P2X receptor characteristics and physiological roles 8
Molecular architecture of P2X receptor 9
Structural rearrangements of P2X receptor upon ATP binding 10
Complex gating of P2X2 receptor 11
Voltage-clamp fluorometry 13
Materials and Methods 15
Ethical approval 15
Molecular biology 15
Preparation of *Xenopus laevis* oocyte 16
Channel expression and electrophysiological recording of *r*P2X2 16
Expression of Anap incorporated *r*P2X2, *Ci*-VSP and *Shaker* B K^+ channel 17
SIK inhibitor application 18
Voltage-clamp fluorometry (VCF) recording 19
Data analysis 20
Statistical Analysis 21
Three dimensional structural modelling of rat P2X2 22
Results 23
Negative and positive control VCF experiments using Anap to confirm that the system is working in P2X2 receptor 23
Fluorescence changes of Anap at A337 and I341 in the transmembrane 2 domain upon ATP and voltage application 24
SIK inhibitor treatment improved VCF optical signal 25
Fluorescence changes of Anap at I341 upon ATP and voltage application exhibit a fast kinetics and linear voltage-dependence 28

Fluorescence changes of Anap at A337 upon ATP and voltage application also exhibit a fast kinetics and linear voltage-dependence 29

Fluorescence change of Anap at A337 upon voltage change was observed also in 0 ATP condition and was [ATP]-dependent 30

Anap fluorophore could exhibit electrochromic effect in site-specific manner in P2X2 receptor 33

A337 in TM2 might interact with F44 in TM1 to stabilize the open state of P2X2 receptor 35

Discussion 39

SIK inhibitor treatment improved VCF-fUAA optical signal 40

Voltage-dependent fluorescence changes of Anap at A337 and I341 were not related to hyperpolarization-induced conformational change but rather reflected a phenomenon related to electrochromic effect 41

The focused electric field at A337 was observed both in the absence and presence of ATP 44

Anap fluorophore could exhibit electrochromic effect in a site-specific manner in P2X2 receptor 44

Interaction between A337 in TM2 and F44 in TM1 in the open (ATP-bound) state is important for the complex gating 45

Mechanisms of P2X2 receptor complex gating 48

Concluding Remarks 50

Acknowledgements 51

References 53

Table 61

Figure 64

Abbreviations

$5\text{-}HT_{3A}$	5-hydroxytryptamine (serotonin) receptor 3A subtype
aaRS	Amber suppressor tRNA/aminoacyl-tRNA synthetase pair
AMPA receptor	α-amino-3-hydroxy-5-methyl-4-isoxazolepropionic acid / glutamate ionotropic receptor
Anap	3-(6-Acetylnaphthalen-2-ylamino)-2-aminopropanoic acid sodium salt
ATP	Adenosine-5'-triphosphate
Ci-VSP	*Ciona intestinalis* voltage-sensing phosphatase
CNS	Central nervous system
Di-1-ANEPIA	1-[3-(Iodoacetyl) amino propyl]-4-[β-(2-dimethylamino)-6-naphthyl] vinyl pyridinium bromide
DMSO	Dimethyl sulfoxide
ECD	Extracellular domain
fUAA	Fluorescent unnatural amino acid
$GABA_A$ receptor	Gamma-aminobutyric acid type A
$GABA_C$ receptor	Gamma-aminobutyric acid type C
HG-9-91-01	Salt-inducible kinase inhibitor 1
*h*P2X3	Human purinergic receptor P2X subtype 3
nAChR	Nicotinic acetylcholine receptor
K2P	Two pore domain potassium channel
M2 receptor	Muscarinic acetylcholine receptor M2 subtype
MTSET	2-(Trimethylammonium)ethyl methanethiosulfonate
MTS-TAMRA	MTS-5(6)-carboxytetramethylrhodamine
NINS	National Institutes of Natural Sciences

P2X receptor	Purinergic receptor P2X
*r*P2X2	*Rattus novergicus* purinergic receptor P2X subtype 2
Shaker B K_v	*Shaker* family voltage-dependent potassium channel
SIK inhibitor	Salt-inducible kinase inhibitor
TM	Transmembrane domains
TMRM	Tetramethylrhodamine maleimide
VCF	Voltage-clamp fluorometry
WT	Wild type
*zf*P2X4	Zebrafish purinergic receptor P2X subtype 4

Summary

P2X2 is a homotrimeric ligand-gated ion channel activated by extracellular ATP. P2X2 receptor is widely distributed in variety of cell types with main distribution in smooth muscles, central nervous system (CNS), retina, chromaffin cells, autonomic and sensory ganglia. P2X2 receptor regulates neurotransmission by both pre- and post-synaptic actions. Based on the crystal structure of zebrafish P2X4 and human P2X3, P2X purinoreceptors are known to have a topology with two transmembrane (TM) domains, a large extracellular ligand binding loop, and intracellular N and C termini. The extracellular domain connecting the two TMs constitutes the largest part of the polypeptide.

One of the interesting characteristics of P2X2 receptor is that it has a complex gating consists of (1) [ATP]-dependent gating and also (2) voltage-dependent gating in spite of the absence of a canonical voltage sensor domain, in clear contrast to the typical voltage-gated channels which have a voltage sensor domain within the structure. It remains unknown how the structural rearrangements occur during the voltage dependent gating. Besides, the detail of the structural rearrangements upon ATP binding in the pore region remains controversial. It is because there is a discrepancy between the two ATP-bound open state from the two solved crystal structures, *zf*P2X4 and *h*P2X3. The *h*P2X3 structure showed longer transmembrane domains than *zf*P2X4 and it includes cytoplasmic domains. The present study aims at analyzing the structural rearrangements of the rat P2X2 receptor upon (1) ATP- and (2) voltage-dependent gating, by voltage-clamp fluorometry (VCF) using fluorescent unnatural amino acid (fUAA) probe.

A usage of fUAA as a probe, made it possible to label any residues within the protein including intracellular region which is not accessible by conventional VCF fluorophores such as Alexa-488 maleimide. Moreover, direct incorporation of the fUAA will increase the

labelling efficiency and also prevent non-specific labelling. The fUAA used here, named *3-(6-acetylnaphthalen-2-ylamino)-2-aminopropionic acid* (Anap), was incorporated into the rat P2X2 protein by using *in vivo* non-sense suppression method where the tRNA Anap-CUA and tRNA-synthetase pair is used to introduce Anap in amber nonsense codon mutation. TAG mutation was introduced to various positions in P2X2 receptor, one at a time including extracellular domain, extracellular linker, transmembrane domains, as well as intracellular domains. A plasmid DNA containing tRNA Anap-CUA and tRNA-synthetase pair was injected to the nucleus of *Xenopus laevis* oocyte. Subsequently, the rat P2X2 cRNA in which the target site was mutated to a TAG codon and Anap were co-injected to the cytoplasmic region of the oocyte on the following day. In addition to that, to improve the VCF recording optical signal by decreasing the intrinsic background fluorescence of oocytes, a small molecule kinase inhibitor named HG-9-91-01 (SIK inhibitor) was applied. ATP- and voltage-evoked current as well as Anap fluorescence signal in the functional Anap mutant P2X2 receptors were successfully recorded simultaneously.

VCF analyses using Anap as a probe to overcome the limitations by the usage of conventional fluorophore with the application of SIK inhibitor to improve the VCF optical signal brought the following findings. (1) Anap was successfully incorporated into P2X2 receptor shown by simultaneously recorded (i) ATP- and voltage- evoked current as well as (ii) Anap fluorescence signal. (2) SIK inhibitor treatment improved VCF-fUAA optical signal. (3) Voltage-dependent fluorescence changes of Anap was observed only at Ala337 and Ile341 in TM2 domain. (4) The changes showed a linear voltage-dependence, and exhibited fast kinetics in ms order which might indicate a phenomenon related to electrochromic effect. (5) The observed electrochromic effect at Ala337 and Ile341 implied that there is a focused electric field at these positions. (6) Voltage-dependent fluorescence change at Ala337 was larger in the absence of ATP than in the presence of ATP, reflecting the ATP-dependent change of the

focused electric field. (7) Mutagenesis studies at Ala337 and Phe44 suggested that the interaction between Ala337 in TM2 and Phe44 in TM1 in the open (ATP-bound) state is important for the complex gating of P2X2 receptor.

Introduction

P2X receptor characteristics and physiological roles

P2X receptors are a ligand-gated cation channel which open upon the binding of extracellular ATP. P2X receptors consist of 7 sub-classes (P2X1 – P2X7) in which each subunit assembles to form trimeric homomers (Fig. 1A) or heteromers (e.g. P2X2/P2X3). The channel of interest in the present study is P2X2 receptor. P2X2 receptor is mainly distributed in smooth muscles, central nervous system (CNS), retina, chromaffin cells, autonomic and sensory ganglia. P2X2 receptor is widespread in the CNS and has been found at both pre- and postsynaptic sites. P2X2 together with P2X4 regulate neurotransmission by both pre-synaptic and post-synaptic actions (Burnstock, 2003).

Recent studies showed that P2X2 receptors has an important roles in auditory transduction specifically in hair cells and supporting cells. Studies in human showed that a dominant negative polymorphism V60L which is located at the extracellular end of the transmembrane domain 1 (TM1) resulted in progressive hearing loss (Yan et al., 2013). Additionally, P2X2 knock out mice also showed hearing loss phenotype and have been used in studies to show that P2X2 in the cochlea is involved in adaptation to elevated sound levels (Housley et al., 2013).

P2X2 receptors also have a cross-inhibition effect on some receptor channels such as nicotinic acetylcholine receptors (nAChRs), $GABA_{A,}$ and $GABA_{C}$ receptors (Khakh et al., 2002; Boue-Grabot et al., 2004 a&b). Even though the details mechanism is still not clear, P2X2 was shown to inhibit the opening of those receptors when they are co-expressed, mimicking the expression pattern in native cells. Interaction between P2X2 and other receptor may also contribute to the trafficking in certain neurons. For instance, a study showed that P2X2 receptors help the trafficking of serotonin receptors ($5\text{-}HT_{3A}$) in hippocampal neurons to target

this receptor to dendrites (Emerit et al., 2016). Another study showed the activation of P2X2 receptors in hippocampal neurons triggers dynamin-dependent internalization of AMPA receptors. These findings highlight the critical role of post-synaptic P2X2 receptors in regulating the surface expression of AMPARs (Pougnet et al., 2014).

Molecular architecture of P2X receptor

Based on the crystal structure of zebrafish P2X4 (Kawate et al., 2009; Hattori & Gouaux, 2012) and human P2X3 (Mansoor et al., 2016), P2X purinoreceptors are known to have a topology with two transmembrane (TM) domains, a large extracellular ligand binding loop, and intracellular N and C termini (Fig. 1B). The extracellular domain (ECD) connecting the two TMs constitutes the largest part of the polypeptide. Each subunit of P2X receptor resembles the shape of a dolphin which consists of head, upper body, dorsal fin, left flipper, right flipper and lower body regions, corresponding to the large ECD and fluke that corresponds to the two TM domains in the structure (Fig. 1C). The ECD contains the ATP binding site and ten conserved cysteine residues which form five disulfide bonds. The TM domain contains the pore for ion permeation, whereas the intracellular domains are known to regulate the function and trafficking of the receptor (Chaurmont et al., 2004; Bernier et al., 2012).

Comparison between the *h*P2X3 structure and previously published *zf*P2X4 structures shows the longer transmembrane domains and the cytoplasmic domain of *h*P2X3 (Fig. 1D). The most striking differences are in the open state structure where *h*P2X3 contains the residues in cytoplasmic regions which were truncated in the open state structure of *zf*P2X4. This cytoplasmic residues forms a domain termed ‘cytoplasmic cap’ whose function is to stabilize the open state. Moreover, the apo structure comparison between *zf*P2X4 and *h*P2X3 reveals several unique features of the *h*P2X3 including a more complete transmembrane domain,

different residues defining the pore constriction, and a Mg^{2+} ion bound in the head domain (Mansoor et al., 2016).

Structural rearrangements of P2X receptor upon ATP binding

Upon ATP binding, P2X receptor undergoes major structural rearrangements with the most striking movements occurring at two major locations (1) the three ATP binding sites which are located at the interfaces of the three subunits and (2) at the extracellular linker region (lower body) which links ECD to the TM helices (Fig. 1C). There are three lateral portals that are defined as 'fenestrations'. These fenestrations, which are located just directly above the ion channel pore, are open when ATP binds to the receptor. In other words, the lateral fenestrations are the pathway through which hydrated ions enter and exit from the receptor (Kawate, et al., 2009; Hattori & Gouaux, 2012).

The structure of TM helices are thought to be altered remarkably, upon the transition from closed to open state, involving both intra- and inter subunit interactions, which results in major movement in the fenestrations. However, a question about whether or not the ATP-bound structure provides the accurate blueprint of the native open channel pore of P2X receptor has been raised recently. This is because (1) the crevices that is proposed to be formed between TM helices of adjacent subunits were denied by a recent molecular dynamics study (Heymann et al., 2013), (2) The inner portion of TM2 helices was proposed to be narrowed upon ATP binding based on metal bridging experiment (Kracun et al., 2010; Li et al., 2010) but it is not shown in ATP-bound structure, and (3) Intracellular domain was truncated for the crystallization, which may misrepresent the functioning structure of the pore. Thus, ATP-bound *zf*P2X4 structure might represent a non-native open channel state (Habermacher et al., 2016).

The question about the structure of TM helices in *zf*P2X4 ATP-bound state was also raised by the newly solved *h*P2X3 structure which has more complete TM domains including

the cytoplasmic region. In *h*P2X3 structure, I323 (I332 in P2X2) defines the extracellular gate in the closed state and T330 (T339 in P2X2) defines the cytoplasmic gate. When ATP binds and the receptor undergoes structural change to the open state, lower body flexes and pulls TM2 to rotate outward. This rotation reorients the position of I323 away from the pore and moves towards the extracellular surface. Simultaneously, T330 also rotates away from the pore center.

The movement of TM2 to open the channel in *zf*P2X4 was described as a purely rigid-body transformation (Hattori & Gouaux, 2012). In contrast, based on the solved crystal structure of *h*P2X3, in addition to rigid-body transformation to open the channel, there is a transition from an α-helix to a 3-10 helix in TM2 which centered within the sequence G333-V334-G335 (G342-V343-G344 in P2X2) (Mansoor et al., 2016). This change is thought to allow the movement of TM2 which associated with channel opening or desensitization.

The comparison between closed state and open state of *h*P2X3 revealed that residues in the cytoplasmic region of *h*P2X3 formed 'cytoplasmic cap' whose function has been strongly proposed to stabilize the open state. This cytoplasmic cap includes elements of secondary structure from both termini, including two sequential β-strands from each of N-terminus and C-terminus. The formation of cytoplasmic cap fixes the cytoplasmic portion of TM2 in place, this then forces the helix to stretch to a 3-10 conformation and thus stabilizing pore opening.

Complex gating of P2X2 receptor

One of the most interesting characteristics of P2X2 receptor is the complex gating which not only depends on ATP as its ligand, like the common ligand-gated ion channel, but also it depends on voltage. Based on the two electrode voltage-clamp recording using *Xenopus* oocyte, in the presence of ATP there is a gradual increase in the inward current upon hyperpolarization. The conductance – voltage relationship shifted toward depolarized potentials with the increase

in [ATP]. Thus, the activation of P2X2 channel is voltage-dependent as well as [ATP]-dependent. (Fujiwara et al., 2009; Keceli & Kubo, 2009).

There is a possibility that the voltage-dependent gating of P2X2 might be due to voltage-dependent block/unblock by some positively charged ions or substances contained in the oocytes. Mg^{2+} as the main intracellular polyvalent cation and polyamines didn't block P2X2 channels (Zhou and Hume, 1998). Besides, this complex gating properties was also observed in other expression systems e.g. HEK293T cells (Fujiwara et al., 2009) and PC12 cells (Nakazawa et al., 1997) by whole cell patch clamp recording. The activation upon ATP and hyperpolarization was also observed by inside-out and whole cell patch clamp recording using blocker-free intracellular solution. Both showed a similar ATP- and voltage-dependent activation to the results from oocytes (Fujiwara et al., 2009). All the studies support that the observed activation upon hyperpolarization is the intrinsic properties of the channel and reflects gating of P2X2 depending both on [ATP] and voltage.

In the voltage-gated ion channels, the canonical voltage sensor domain (VSD) is included in its structure. Canonical VSD in voltage-gated ion channel is formed by the first four transmembrane helices (S1-S4) and the S4 region contains several positively charged amino acids residues in TM domain. The movement of the S4 region upon depolarization initiates a conformational change in the gate of the conducting pathway thus controlling the flow of ions.

It is of interest to know why and how P2X2 also has a voltage-dependent gating in spite of the absence of canonical VSD within its structure. It raised a question about the role of two transmembrane domains of this receptor during the complex gating by ATP and voltage. Furthermore, the structural rearrangements during [ATP] - and voltage-dependent gating of P2X2 receptor remain unknown. Besides, as mentioned above, the structural rearrangements upon ATP binding in the pore region remain controversial. It is because there is a difference between the two ATP-bound open state from the solved crystal structures of *zf*P2X4 and *h*P2X3.

Thus, the present study aims at analyzing the structural rearrangements of P2X2 receptor upon (1) ATP- and (2) voltage-dependent gating, by voltage-clamp fluorometry (VCF) using fluorescent unnatural amino acid (fUAA) as a probe.

Voltage-clamp fluorometry

Fluorometry has been used to analyze the structural rearrangements of proteins for a long time because the fluorescence intensity of many fluorophores highly depends on environmental factors such as hydrophobicity, collisional quenching, or anisotropy. Thus it is possible to monitor or capture the conformational changes of proteins as the changes in fluorescence intensity. By combining the fluorometry and voltage-clamp recording, it delivers such a powerful method to track down real time conformational changes within the ion channel structure when it is activated (Mannuzu et al., 1996; Pless & Lynch, 2008; Nakajo & Kubo, 2014; Talwar & Lynch, 2015). VCF recording is performed in mutated ion channel of interest where one of its residues is labeled by a fluorophore to report the structural rearrangements.

Conventional VCF probes such as Alexa-488 maleimide or tetramethylrhodamine maleimide (TMRM) have been used to label the cysteine residue on the extracellular side of the target ion channel introduced by mutation (Mannuzu et al., 1996; Pless & Lynch, 2008; Dekel et al., 2012; Nakajo & Kubo, 2014; Talwar & Lynch, 2015). There are some limitations as follows; (1) there is a difficulty to specifically label ion channels which have free cysteine residues other than the one that has been mutated to cysteine for probing. It will result in non-specific labeling. (2) The labeling efficiency is not 100% as many factors could affect it e.g. the environmental condition during labeling. (3) Conventional VCF probes cannot pass through the cytoplasmic membrane so that either the deeper part of the TM domain or intracellular domain cannot be labeled.

Incorporation of fluorescent unnatural amino acid into ion channel and receptor protein could overcome the limitations caused by conventional fluorophore in VCF recording. *3-(6-acetylnaphthalen-2-ylamino)-2-aminopropanoic acid* (Anap) is one of the fluorescent unnatural amino acids. Anap can be site-specifically incorporated into any positions of proteins at the introduced TAG codon with high efficiency using an orthogonal amber suppressor tRNA/aminoacyl-tRNA synthetase (aaRS) pair as shown in Fig. 2 (Lee et al., 2009; Chatterjee et al., 2013). The relatively small size of Anap also made a minimum perturbation to the protein structure (Sakata et al., 2016). In the present study, VCF analysis using fUAA was performed.

Materials and Methods

Ethical approval

All animal experiments were approved by the Animal Care Committee of the National Institutes of Natural Sciences (NINS, Japan) and performed obeying its guidelines.

Molecular biology

Wild type (WT) *Rattus novergicus* P2X2 (*r*P2X2) receptor cDNA (Brake et.al, 1994) was subcloned into BamH1 site of pGEMHE. TAG or any single amino acid mutation and/or double mutations were introduced using a Quikchange site-directed mutagenesis kit (Agilent Technologies). The introduced mutations were confirmed by DNA sequencing. mMESSAGE T7 RNA transcription kit (Thermo Fisher Scientific) was used to transcribe WT and mutant *r*P2X2 cRNAs from plasmid cDNA linearized by Nhe1 restriction enzyme (Toyobo). The tRNA-synthetase/Anap-CUA encoding plasmid was obtained from Scripps Research Institute. Salt form of fUAA Anap was used (Futurechem).

Ciona intestinalis voltage-sensing phosphatase (*Ci*-VSP) with a mutation in the gating loop of the phosphatase domain (F401Anap) was used as a positive control (Sakata et al., 2016). mMESSAGE SP6 RNA transcription kit (Thermo Fisher Scientific) was used for cRNA transcription of *Ci*-VSP. TAG mutation was also introduced to *Shaker* B K^+ channel, with a deletion of the N-terminal inactivation moiety (residues 6–46 in the N terminal cytoplasmic domain, Hoshi et al., 1990) and with a mutation of T449V which diminishes the C-type inactivation (Lopez-Barneo et al., 1993), to further examine the electrochromic effect of Anap fluorophore. mMESSAGE T7 RNA transcription kit (Thermo Fisher Scientific) was used to transcribe Anap mutants of *Shaker* B Δ6-46 T449V cRNAs from plasmid cDNA linearized by Kpn1 restriction enzyme (Toyobo).

Preparation of *Xenopus laevis* oocyte

0.15% tricaine (Sigma-Aldrich) was used as an anesthetic reagent for *Xenopus laevis* before surgical operation for isolation of oocytes. After the final collection, the frogs were humanely sacrificed by decapitation. Follicular membranes were removed from isolated oocytes by collagenase treatment (2 mg ml^{-1}; type 1; Sigma-Aldrich) for 6.5 hours. Oocytes were then rinsed and stored in frog Ringer's solution (88 mM NaCl, 1 mM KCl, 2.4 mM $NaHCO_3$, 0.3 mM $Ca(NO_3)_2$, 0.41 mM $CaCl_2$, 0.82 mM Mg_2SO_4, and 15 mM HEPES pH 7.6 with NaOH) containing 0.1% penicillin-streptomycin at 17 ^oC.

Channel expression and electrophysiological recording of *r*P2X2

Xenopus oocytes injected with 0.5 ng of WT *r*P2X2 cRNA and incubated for 2 days at 17 ^oC showed a high expression level phenotype of WT *r*P2X2 that has less voltage dependence than those of low expression level of P2X2 ($I < 4.0$ μA at -60 mV, Fujiwara and Kubo, 2004). To achieve low expression level, oocytes were injected with 0.05 ng of WT *r*P2X2 cRNA and incubated for 1-2 days. For *r*P2X2 mutants, oocytes were injected with 0.5 ng – 2.5 ng of cRNA and incubated for 1-3 days depending on the desired expression level.

Voltage clamp for macroscopic current recording was performed by using an amplifier (OC-725C; Warner Instruments), a digital-analogue analogue-digital converter (Digidata 1440, Molecular Devices), and pClamp10.3 software (Molecular Devices). In TEVC recording, borosilicate glass capillaries (World Precision Instruments) was used with a resistance of 0.2–0.5 MΩ when filled with 3 M KOAc and 10 mM KCl. P2X2 bath solution contained 95.6 mM NaCl, 1 mM $MgCl_2$, 5 mM HEPES, and 2.4 mM NaOH at pH 7.35 – 7.45. Ca^{2+} was not included in the bath solution in order to avoid the inactivation of the receptor and secondary intracellular effects, e.g. activation of Ca^{2+} dependent chloride channel currents, (Ding and Sachs, 2000).

ATP disodium salt (Sigma-Aldrich) was prepared in various concentrations (1 μM, 3 μM, 10 μM, 30 μM, 100 μM, 300 μM, 1 mM, and 3 mM) by dissolving it in the bath solution. For recording using step pulses protocol, ATP was applied by two ways depending on the purpose of the experiments and the phenotype of the mutants. (1) Direct application using motorized pipette (Gilson pipetman) which was set to exchange the whole bath solution with ligand-based solution. 2000 μL (five times larger than the bath volume) of ligand-based solution was applied. (2) Perfusion of a recording chamber using a perfusion system set (ISMATEC pump). In both cases overflowed bath solution was continuously removed using a suction pipette by negative air pressure. Oocytes were held at -40 mV and voltage step pulses were applied in the range from +40 mV to -140 mV. Tail currents were recorded at -60 mV to measure conductance-voltage (G-V) relationship. Recordings were performed at room temperature (24±2 ^{o}C).

Expression of Anap incorporated *r*P2X2, *Ci*-VSP and *Shaker* B K^+ channel

For functional expression of channels which incorporated Anap, 1.25 ng of cDNA encoding the tRNA synthetase/Anap-CUA pair was injected into the nucleus of defolliculated *Xenopus* oocytes located in the center of the animal pole (Kalstrup & Blunck 2013). Oocytes were then incubated for 24 hours at 17 ^{o}C to allow tRNA transcription and synthetase expression. Subsequent step was performed in the minimization of light exposure as it may excite the fluorophore. Either 1.4 – 5.4 ng of *r*P2X2 cRNA, 8.2 ng of *Ci*-VSP cRNA, or 1.4 -2.7 ng of *Shaker* B cRNA in which the target site was mutated to a TAG codon, was co-injected with 23 nL of 1 mM Anap. A schematic drawing of the incorporation of Anap into oocyte expression system is represented in Fig. 2. Oocytes were incubated in frog Ringer's solution (containing 0.1% penicillin-streptomycin) for 1-3 days (*r*P2X2) or 3-5 days (*Ci*-VSP) or 2-3 days (*Shaker* B) depending on the desired expression level. In the absence of either tRNA synthetase/Anap-

CUA plasmid or fUAA Anap, no channel expression was detected in *r*P2X2 Anap mutants, confirming that functional channels are expressed only when they successfully incorporated fUAA.

SIK inhibitor application

HG 9-91-01 / SIK inhibitor (MedChem Express) was dissolved in DMSO to make a stock solution of 10 mM and kept as aliquot at -80 ^{o}C. SIK inhibitor was diluted before use with RNase-free water (Otsuka) into certain concentrations for injection to oocytes. Various concentrations of SIK inhibitor was injected into oocyte*'s* nucleus to determine the most effective concentration to improve the optical recording of VCF-fUAA experiment. SIK inhibitor was mixed and co-injected with either (1) tRNA synthetase/Anap-CUA plasmid (nuclear injection) or (2) cRNA + Anap (cytoplasmic injection). 300 nM defined as the amount of the co-injected SIK inhibitor in mixed solution. For instance, the actual concentration of SIK inhibitor is 600 nM for 1:1 mixture with 2.5 ng tRNA synthetase/Anap-CUA plasmid. As the volume of the oocyte nucleus is ~40 nL, and it can tolerate 15-20 nL of injected volume (Lin-Moshier and Marchant, 2013) so the final concentration of SIK inhibitor inside the oocyte nucleus was ~150 nM.

First of all *Ci*-VSP F401Anap, the positive control in the present study, was used to confirm reproducible and apparent effects in the initial optimization experiments. The most effective concentration of SIK inhibitor was determined to be 300 nM. Next, 300 nM of SIK inhibitor was co-injected to either nucleus or cytoplasmic of the oocytes and were incubated for different days. This resulted in three test groups: (1) nuclear injection with 2 days incubation; (2) nuclear injection with 3 days incubation; and (3) cytoplasmic injection with 2 days incubation. Cytoplasmic injection needs concentration adjustment since the volume of an

oocyte is ~1 μL. To make the concentration inside the oocyte 150 nM, so the injected amount was 3 μM. Control groups consist of two non-treated oocytes, incubated for either 2 or 3 days.

Follow up experiment was done using P2X2 A337Anap/R313W mutant after the optimum concentration, injection method, and incubation days were determined from *Ci*-VSP experiment. This experiment was performed to conclude whether SIK inhibitor treatment also works in VCF-fUAA recording of P2X2 receptor. 300 nM of SIK inhibitor was co-injected into the nucleus of the oocyte. Oocytes were then incubated for 2-3 days after the following cytoplasmic injection to co-inject channel cRNA and Anap.

Voltage-clamp fluorometry (VCF) recording

Oocytes for VCF-fUAA recording needed to be minimized from light exposure. Oocytes were placed in a recording chamber with the animal pole facing upward. For ATP evoked current recording, gap free protocol was applied with the holding potential at -80 mV. ATP was applied by perfusion system as described above. For voltage evoked current recording, oocytes were held at -40 mV or +20 mV in some cases. The step pulses were applied from +40 mV to -140 mV.

Initially, after ATP was applied by perfusion system and the channel was activated, voltage step pulses were applied to the same oocyte. Later on, two recordings (ATP application and voltage application) were performed separately in different oocytes. Meanwhile, for VCF recordings in the absence and presence of ATP using voltage step pulses in some mutants (A337Anap, A337Anap/R313F, and A337Anap/R313W) were performed in the same oocytes.

For the voltage step application, ATP was applied directly. As bath volume was measured to be 600 μL, 20 μL ATP of 30 times higher concentration was applied directly to the bath solution. For *Ci*-VSP voltage-clamp recording, cells were clamped at -60 mV and the step pulses were applied from -80 mV to +160 mV every 3 seconds. For *Shaker* B, cells were

clamped at -100 mV and the step pulses were applied from -100 mV to +60 mV with 10-mV increments.

The fluorometric recordings were performed with a water immersion objective lens (Olympus XLUMPLAN FL 20x/1.00) to collect the emission light from the voltage-clamped oocytes. The light from xenon arc lamp (L2194-01, Hamamatsu Photonics) was applied through a band-pass excitation filter (330-360 nm for Anap). In the case of the excitation of Anap to minimize the photobleaching during ATP-application recording, intensity of the excitation light was decreased to 1.5% by ND filters (U-25ND6 and U-25ND25 Olympus), whereas for step pulses recording the intensity of the excitation light was decreased to 6% (U-25ND6 Olympus). Emitted light was passed through the band pass emission filter (Brightline, Semrock) of 420–460 nm and 460–510 nm (Lee et al., 2009; Sakata et al., 2016). The emission signals were detected by two photomultipliers (H10722-110; Hamamatsu Photonics). The detected emission intensities were acquired by the Digidata 1332 (Axon Instruments) and pClamp 10.3 software (Molecular Devices) at 10 kHz for ATP application and 20 kHz for voltage application. In the case of *Ci*-VSP and *Shaker* B, the detected emission were acquired at 10 kHz. To improve signal to noise ratio, VCF recording in step pulses protocol was repeated 20 times for each sample for P2X2 and 3 times for *Ci*-VSP and *Shaker* B. Averaged data were used for data presentation and analysis.

Data analysis

Two electrode voltage-clamp data were analyzed by using Clampfit 10.5 software (Molecular Devices) and Igor Pro 5.01 (Wavemetrics). Analyses of conductance-voltage (G-V) relationship of P2X2 were obtained from tail currents recording at -60 mV and fitted to a two-state Boltzmann equation using Clampfit:

$$I = I_{min} + \frac{I_{max} - I_{min}}{1 + e^{\frac{ZF}{RT}\left(V - V_{1/2}\right)}} \quad (1)$$

where I_{min} and I_{max} are defined as the limits of the amplitudes in fittings, Z is defined as the effective charge, $V_{1/2}$ is the voltage of half activation, F is Faraday's constant, and T is temperature in Kelvin.

In the case of P2X2, Normalized conductance-voltage (G-V) relationships were plotted using:

$$G/G_{max} = I/I_{min} = 1 - (1 + e^{ZF(V-V_{1/2})/RT})^{-1} (1 - I_{max}/I_{min}) \quad (2)$$

In the case of voltage-clamp fluorometry data, the gradual decline of fluorescent recording traces due to the photobleaching was compensated by subtracting the expected time-lapse decrease in bleached component calculated from the trace's bleaching rate (R) by assuming that the fluorescence is linear. Arithmetic operations were performed by Igor Pro 5.01 for ATP evoked fluorescent signals.

Compensated data = Recorded F data + R * point number (3)

In the case of fluorescent traces from voltage application for both P2X2, *Ci*-VSP, and *Shaker* B arithmetic operations were performed by Clampfit.

[Compensated trace] = [Recorded F trace] x (1 – (R x [time])) (4)

Where [time] is the value of the point given by Clampfit. All the compensated traces were then normalized by setting each baseline (F signal at -40 mV or at +20 mV depending on the holding potential) level to be 1 to calculate the % F change ($\Delta F/F$; $\Delta F = F_{-140mV} - F_{baseline}$; $F = F_{baseline}$). The data were expressed as mean±s.e.m with n indicating the number of samples.

Statistical Analysis

Statistical analysis was performed by either one-way ANOVA, two-sample t-test, or paired t-test. Following Tukey post hoc test one-way ANOVA, was applied. The data were expressed as mean ± s.e.m with n indicating the number of samples. Values $p<0.05$ were defined as statistically significant. *, **, *** denote values of $p < 0.05$, 0.01 and 0.001, respectively. All

the statistical analysis and the bar graphs were performed and generated with Origin version 2017 (OriginLab; student version).

Three dimensional structural modelling of rat P2X2

Homology modelling was performed using a web-based environment for protein structure homology modelling SWISS-MODEL (Arnold et al., 2006; Biasini et al., 2014) based upon sequence alignment of amino acids of *r*P2X2 (NM_053656) and crystal structure of *h*P2X3 (Protein Data Bank accession number 5SVJ and 5SVK for closed and ATP-bound open state, respectively) (Mansoor et al., 2016). All the structural data presented in this study were generated using PyMOL molecular graphics system ver. 1.3 (Schrödinger, LLC; educational version). Protein visualization was generated using Protter: interactive protein feature visualization and integration with experimental proteomic data (Omasits et al., 2014).

Results

Negative and positive control VCF experiments using Anap to confirm that the system is working in P2X2 receptor

As the initial VCF using fUAA, negative and positive controls were tested to confirm that the system used in this study is working. For negative control experiments, there are two kind of conditions that were applied to the injection to oocytes; (1) P2X2 TAG mutation cRNA (D315Anap) and Anap, without plasmid (tRNA synthetase/tRNA Anap-CUA) (2) P2X2 TAG mutation cRNA (D315Anap) without Anap and plasmid (Fig. 3). Macroscopic currents for both of the injected groups were recorded by using gap-free protocol with holding potential at -80 mV as well as step pulses protocol as mentioned in Materials and Methods section. 100 μM ATP which gives maximum response was applied. Anap fluorescence signals were also recorded simultaneously with the currents at both 420-460 nm (440 nm) and 460-510 nm (500 nm). VCF experiments were performed at least for 2 different batches of oocytes (n=5-7 for each group). Both groups showed extremely small current (<200 nA) and also relatively low fluorescence intensity which is most likely come from the autofluorescence of oocyte (Fig. 3). The results verified that only P2X2 channels which incorporated with Anap in the presence of tRNA-synthetase and tRNA Anap-CUA pair were expressed on the membrane.

Ciona intestinalis voltage-sensing phosphatase (*Ci*-VSP) was used for positive control experiment (Fig. 4) since it was reported to give strong and highly reproducible fluorescence signal change upon depolarization (Sakata et al., 2016). Mutation was originally introduced at F401 (gating loop of the phosphatase domain). F401Anap *Ci*-VSP were expressed in oocytes and since it is a phosphatase, there wasn't any current recorded. Only the fluorescence signals at 440 nm and 500 nm were recorded simultaneously upon voltage step pulses to depolarized potential (Fig. 4). In VCF, changes in fluorescence signal of Anap are assumed as the local

conformational changes of the protein region at which the fluorophore is introduced. Based on the crystallographic studies of voltage-sensing phosphatase, this movement of the gating loop in phosphatase domain is controlled by its voltage sensor (Liu et al., 2012). Fluorescence changes were observed at both wavelengths ($\Delta F/F=1.5\pm0.2\%$ at 440nm, $\Delta F/F=5.3\pm0.7\%$ at 500nm, n=9) and the change exhibited the same tendency reported in the previous study (Sakata et al., 2016). Interestingly, fluorescence changes observed at F401Anap have bidirectional changes depending on each wavelength (downward at 440 nm and upward at 500 nm). To dates, this kind of changes haven't been analyzed thoroughly and is thought to have a possibility to reflect multiple states of the catalytic region in VSP (Sakata et al., 2016). Depolarization-induced fluorescence changes were detected in most of the recorded cells, indicating that the reproducibility of fluorescence change is high in *Ci*-VSP. Anap system was confirmed to work in the *Xenopus* oocytes expression system as well as the VCF setup used in this study.

Fluorescence changes of Anap at A337 and I341 in the transmembrane 2 domain upon ATP and voltage application

Since P2X2 receptor does not have a canonical voltage-sensing domain (VSD), as a starting point in the present study, Anap mutant scanning was done by introducing TAG mutation one at a time in all regions of P2X2 receptor including cytoplasmic N-terminus (8 positions), TM1 (20 positions), Extracellular domain (ECD, where the ATP binding site is located, 25 positions), TM2 (24 positions), and cytoplasmic C-terminus (19 positions) (Fig. 5A, B). VCF combined with Anap made it possible to label the residues located at lower TM domains and intracellular regions which are not accessible by conventional fluorophores such as Alexa-488. The whole part of TM1 and TM2 of the receptor was scanned as this is the transmembrane spanning domains in which a non-canonical voltage sensor might be located.

From the total of 96 position of Anap mutant scanning in P2X2 receptor (Fig. 5A, B), many of them showed fluorescence changes upon ATP application but not voltage application as summarized in Table 1. VCF recording solely upon ATP application was not performed at each scanned position as this is not the major focus in the present study. As major and overall structural movement occurs upon the binding of ATP during the channel transition from close to open state in P2X receptor (Kawate et al., 2009; Hattori & Gouaux, 2012; Mansoor et al., 2016), it was expected that fluorescence change upon ATP application occurs at many positions which labeled by Anap. Most of the Anap fluorescence changes followed the P2X2 current during ATP application, and the changes most likely indicate the ATP evoked structural rearrangements at around the labeled residues (Fig. 6).

In contrast, surprisingly only two positions out of 96 scanning positions located at TM2 domain showed Anap fluorescence changes in response to voltage stimuli. The two positions are A337 ($\Delta F/F=0.5\pm0.2\%$ upon voltage change from +40 mV to -140 mV at 440 nm, n=3, Fig. 7A) and I341 ($\Delta F/F=0.3\pm0.2\%$ upon voltage change from +40 mV to -140 mV at 440 nm, n=3, Fig. 7B). Although the Anap fluorescence changes were observed after the application of 10 μM ATP and voltage step pulses which were shown at A337 and I341, there are two problems regarding the VCF-fUAA experiment at P2X2 receptor as follows: (1) The fluorescence signal change is close to the limit of detection ($\Delta F/F = <1\%$), makes it hard to perform further analysis e.g. F-V relationship because signal to noise ratio is low; (2) The incidence of fluorescence change is also low. Thus, at this point, further analysis to determine what kind of structural movements the fluorescence changes are associated with, could not be performed.

SIK inhibitor treatment improved VCF optical signal

To overcome the problems of low incidence of successful detection of fluorescence changes and below detection limit of fluorescence changes, small molecule kinase inhibitor, namely SIK

inhibitor (HG-9-91-01), was applied by injecting into the oocytes to decrease the intrinsic background fluorescence in the oocytes (Lee & Bezanilla, 2019). This inhibitor promotes the UV-independent skin pigmentation by the increase in the production of melanin (Mujahid et al., 2017). It resulted in the darker surface of the animal pole of the oocytes. As the intrinsic background fluorescence in the oocytes is decreased, the percentage of fluorescence change is expected to increase.

Optimization of SIK inhibitor treatment in VCF experiment was done by two subsequent ways. (1) The optimal concentration of SIK inhibitor injected to the oocytes to give a maximum effect in decreasing the intrinsic fluorescence background of the oocytes. (2) The optimal injection condition, which depends on two aspects: the location of microinjection in the oocytes (nuclear or cytoplasmic) and the length of incubation days.

Ci-VSP F401Anap, the positive control in this present study, was used to give reproducible and distinct results (Fig. 8). Oocytes were pre-treated with two concentrations of SIK inhibitor (30 nM and 300 nM, which reflects the concentration of injected solution). 300 nM SIK application increases the percentage of fluorescence change more than 2 times higher than the non-treated one ($\Delta F/F$= 10.5%±2.4 at 500 nm, n=6 and $\Delta F/F$= 3.2%±0.8, n=8 respectively, Fig. 8A, C). In the case of *Ci*-VSP, as the biggest fluorescence changes between the two wavelengths (440 nm and 500nm) always observed at 500 nm (Fig. 4) (Sakata et al., 2016), thus all the statistical analysis were performed only from the fluorescence signal changes at 500 nm. The statistical significance ($p<0.05$) was shown by one-way ANOVA with Tukey post-hoc test (Fig. 8D). Application of 30 nM SIK inhibitor didn't give any remarkable increase in the percentage of fluorescence change compared to control group ($\Delta F/F$= 6.3%±1.9, n=6, Fig. 8B). This showed that 300 nM SIK inhibitor treatment into the oocytes could decrease the intrinsic background fluorescence of the oocytes thus increase the percentage of the fluorescence change.

Subsequently, second optimization experiments were performed (Fig. 8E). All of following experiments used 300 nM SIK inhibitor. Control groups consist of non-treated oocytes which were incubated for either 2 or 3 days. Nuclear injection group only consists of oocytes which were incubated for 3 days. Cytoplasmic injection groups consist of oocytes which were incubated for either 2 or 3 days. Oocytes with SIK inhibitor injected into the nucleus and incubated for 3 days gave the largest fluorescence changes among other groups ($\Delta F/F$= 10.5%±2.4 at 500 nm, n=6). Non-treated oocytes with 2 days incubation resulted in 4.6%±0.5 (n=12). Non-treated oocytes with 3 days incubation resulted in 3.2%±0.8 (n=8). On the other hand, oocytes with SIK inhibitor injected into the cytoplasm resulted in 4.5%±0.7 (n=8) for 2 days incubation and 6.4%±1.3 (n=5) for 3 days incubation. These results suggested that the most optimal condition for SIK inhibitor treatment is nuclear injection with 300 nM SIK inhibitor and 3 days incubation (Fig. 8E).

After the optimal concentration, injection method, and incubation days were determined from *Ci*-VSP experiment, SIK inhibitor was then applied in P2X2 A337Anap/R313W mutant (Fig. 9). This experiment was performed to examine if SIK inhibitor treatment also works in VCF-fUAA recording of P2X2 receptor, the main target in the present study. 300 nM SIK inhibitor treatment didn't give any significant difference in terms of the percentage of the fluorescence change compared to the control group ($p=0.76$ analyzed by two-sample t-test with $\Delta F/F$= 0.7%±0.3 at 440 nm, n=7 and $\Delta F/F$= 0.8%±0.2 at 440 nm, n=12 for control and 300 nM SIK inhibitor treatment group, respectively, Fig. 9A-C). In the analysis of the incidence of detectable change of Anap fluorescence between two groups, the one treated with 300 nM SIK inhibitor showed a higher percentage incidence than the control group (300 nM SIK inhibitor application = 80%, n=12 (Fig. 9E) and control = 57%, n=7 (Fig. 9D). These results showed that in the case of P2X2, SIK inhibitor treatment improved the incidence of detectable Anap

fluorescence change. Therefore, it was decided to use SIK inhibitor in all the following experiments.

Fluorescence changes of Anap at I341 upon ATP and voltage application exhibit a fast kinetics and linear voltage-dependence

By applying 300 nM SIK inhibitor, a clearer and more frequent Anap fluorescence change could be detected at the position of I341 in the TM2 ($\Delta F/F$= 0.7%±0.2 at 440 nm, n=3, Fig. 10A) upon ATP and voltage application. G-V relationship by the application of 10 μM ATP of this mutant was not different from wild type as shown at Fig. 10B. A further analysis regarding the fluorescence change was then performed to elucidate what kind of structural movements this fluorescence change at I341 is associated with.

F-V relationship of I341Anap upon voltage step pulses in the presence of 10μM of ATP from +40 mV to – 160 mV with a holding potential at -40 mV showed a linear voltage-dependence ($y = 0.007x - 0.039$; $R^2 = 0.99$, n=3, Fig. 10D). Besides, fluorescence change occurred almost instantaneously in less than 5 ms time scale (Fig. 10C). It showed that the kinetics of $\Delta F/F$ are very rapid and faster than the time course of voltage-dependent current activation. This also correlate well with the speed of the actual membrane potential change achieved by voltage clamp. These analyses of fluorescence changes at I341 indicated that the downward fluorescence change is not associated with the protein conformational change which usually shown by the gradual increase of F-V following the G-V to either depolarized or hyperpolarized potential. These changes are rather thought to be due to a phenomenon related to electrochromic effect.

Electrochromic effect is a shift in the fluorophore emission spectrum because of an interaction of the fluorophore electronic state with the local electric field (Dekel et al., 2012). It has two distinctive characteristics: (1) fast kinetics of fluorescent change (ΔF-fast); (2) linear

voltage-dependence of F-V relationship (Asamoah et al., 2003). The electrochromic effect shown in some voltage-sensitive dyes which are used to directly detect the change of membrane potential by attaching it to the cell membrane. If the fluorophore is directly attached to certain positions within ion channels / receptors as shown by studies in *Shaker* B K^+ channel (Asamoah et al., 2003) and M_2 muscarinic receptor (Dekel et al., 2012), the detection of electrochromic effect implies that there is a local convergence of the electric field at the position where the fluorophore is attached. Thus, the observed fluorescence change at the position of I341 in P2X2 receptor reflects the electrochromic effect, implying that there is a focused electric field at I341 in TM2 domain during the complex gating of P2X2 receptor.

Fluorescence changes of Anap at A337 upon ATP and voltage application also exhibit a fast kinetics and linear voltage-dependence

Based on the previous results without the treatment of SIK inhibitor, A337Anap at TM2 domain showed low incidence of successful detection and had rather small percentage of the fluorescence change (Fig. 7A), making it hard to do further analysis. By the application of 300 nM SIK inhibitor, a more frequent and improved signal to noise ratio of fluorescence changes could be observed at A337 ($\Delta F/F$= 1.6%±0.2 at 440 nm, n=4, Fig. 11A). VCF recording was performed by the application of 10 μM ATP and voltage step pulses from +40 mV to -140 mV with a holding potential at +20 mV. G-V relationship for this mutant showed that a large fraction of the channel are already open at 10 μM ATP application compared to wildtype (Fig. 11B), because of the high density of the channel expressed shown by a rather big current amplitude (> 20 μA). A previous study showed that P2X2 channel properties are correlated with the expression level (Fujiwara & Kubo, 2004). Nonetheless, we still could see a weak voltage-dependent relaxation during hyperpolarization, thus this fluorescence change still reflects an event occurring at around the position of A337 when the receptor senses the change

in membrane voltage. Furthermore, in the case of lower expression level, this mutant showed a phenotype like wildtype. For the purpose of VCF experiment, however generally high expression level is needed to observe a fluorescence change.

F-V relationship of A337Anap also showed a linear voltage-dependence ($y = 0.011x - 0.126$; $R^2 = 0.99$, n=4, Fig. 11D). Moreover, fluorescence change also occurred almost instantaneously in less than 5 ms time scale (Fig. 11C). It showed that the kinetics of $\Delta F/F$ are far faster than the time course of voltage-dependent current activation. This kinetics reflects the time course of the actual membrane potential. Thus, the fluorescence changes observed at the position of A337 in TM2 domain also aren't correlated with hyperpolarization-induced conformational change. The changes rather due to a similar phenomenon observed at the position of I341 which related to electrochromic effect. This implies that there is also a focused electric field at the position of A337 as Anap is directly attached to this position. Taken together, the observed fluorescence changes at I341 and A337 in TM2 domain implies that there is an electric field convergence at both positions close to each other which could be critical for the complex gating.

Fluorescence change of Anap at A337 upon voltage change was observed also in 0 ATP condition and was [ATP]-dependent

To ensure that the fluorescence changes observed at A337 upon voltage change is not due to the change of ion flux like in the case of K2P K^+ channel (Schewe et al., 2013), recording with voltage step pulses application was performed in the absence of ATP. In the same cells, two kind of VCF recordings were done as follows: (1) voltage-step pulses application in the absence of ATP; (2) voltage-step pulses application in the presence of 10 μM ATP.

When the voltage step pulses were applied in the absence of ATP, fluorescence change was observed ($\Delta F/F = 1.9\% \pm 0.4$ at 440 nm, n=4, Fig. 12A, C). The changes also exhibited fast

kinetics and a linear voltage dependence ($y = 0.007x - 0.098$; $R^2 = 0.99$). When the voltage step pulses were applied to the same cell in the presence of 10 μM ATP, a similar fluorescence change was observed ($y = 0.003x - 0.051$; $R^2 = 0.98$). ΔF/F in the absence of ATP was larger than that in the presence of ATP (ΔF/F= 0.7%±0.1 at 440 nm, n=4, Fig. 12B, C). It can be seen in the superimposed fluorescence traces of 0 ATP and 10 μM ATP at -140 mV (Fig.11D) which was significantly different ($p<0.05$, paired t-test, Fig 12C). When F-V in each condition was plotted together (Fig. 12E), it also showed that the focused electric field at the position of A337 was stronger in the absence of ATP than in the presence of 10 μM ATP.

However, A337Anap mutant showed a high basal activity when the expression level was high. As observed in the current traces in no ATP, some of the channels expressed were already open (Fig. 12A). Thus, the fluorescence changes in 0 ATP might just represent the focused electric field in the presence of ATP which had been observed by the previous experiments. To record ΔF in the closed state with little current in no ATP, additional mutation was introduced which suppresses the basal activity by stabilizing the closed state.

The extracellular linker plays important roles in transmitting the signal from the ATP binding pocket (ECD domain) to the TM domains, as shown by mutagenesis study using tandem trimeric constructs in P2X2 receptor to investigate how the signal from ATP activation is transmitted within the receptor (Keceli and Kubo, 2014). A mutation of R313 at extracellular linker in β-14 which directly links the ATP binding site in ECD domain and TM2 domain to phenylalanine or tryptophan showed a strong phenotype by stabilizing the closed state of P2X2 receptor, as can be seen in the G-V relationship in 100 μM ATP (Figs. 13A, B; 15A, B; for R313F and R313W respectively). This mutation was introduced on top of A337Anap (A337Anap/R313F or A337Anap/R313W) to confirm whether the focused electric field already presents at the position of A337 even when the channel is mostly closed in 0 ATP.

Both results from VCF recording of A337Anap/R313F (Figs. 13,14) and A337Anap/R313W (Figs. 15,16) confirmed that the focused electric field already present at A337 even when the channel is closed. VCF recording in the absence of ATP for A337Anap/R313F showed a remarkable Anap fluorescence changes along with mostly closed channels with only small current when the voltage step pulses was applied ($\Delta F/F$= 2.6%±0.3 at 440 nm, n=8; Fig. 13C, E). 30 μM ATP application resulted in smaller fluorescence changes than those in 0 ATP condition ($\Delta F/F$= 1.7%±0.2 at 440 nm, n=8; Fig. 13D, E).

These series of experiments confirmed that the focused electric field at the position of A337 was stronger in the absence of ATP than in the presence of ATP as shown by: (1) superimposed fluorescence traces at -160 mV for both conditions (Fig. 13F) which has been analyzed to be significantly different ($p<0.05$, paired t-test, Fig 13E). (2) A linear voltage dependence of F-V relationship in the absence of ATP ($y = 0.006x - 0.062$; $R^2 = 0.99$) and in the presence of 30 μM of ATP ($y = 0.004x - 0.044$; $R^2 = 0.99$) (Fig. 13G).

It is of interest to know whether the concentration of ATP affects the focused electric field at A337. Therefore, a higher concentration of ATP (100 μM) was tested for the same series of experiments. Fluorescence changes were also larger in the absence of ATP ($\Delta F/F$= 2.4%±0.3 at 440 nm, n=8 Fig. 14A, C) and smaller in the presence of 100 μM ATP ($\Delta F/F$= 0.9%±0.1 at 440 nm, n=8 Fig. 14B, C). The superimposed traces at -140 mV were analyzed to be significantly different ($p<0.001$ for both, paired t-test, Fig. 14C, D). The fluorescence change was shown to become smaller with the increase in [ATP], by comparing fluorescence changes in the presence of 30 μM and 100 μM ATP. Besides, linear F-V relationship for 0 ATP ($y = 0.006x - 0.0917$; $R^2 = 0.99$) compared with linear F-V relationship for 100 μM ATP ($y = 0.003x - 0.045$; $R^2 = 0.98$ showed that the focused electric field was far weaker (Fig. 14E).

Similar series of experiments were also done using A337Anap/R313W construct (Fig. 15A, B) as this showed a similar phenotype as A337Anap/R313F. A337Anap/R313W also

showed a remarkable Anap fluorescence changes with only small current when the voltage step pulses were applied in the absence of ATP (ΔF/F= 2.8%±0.7 at 440 nm, n=5; Fig. 15C, E). When 30 μM of ATP was applied, the fluorescence changes were smaller than in 0 ATP condition (ΔF/F= 1.8%±0.4 at 440 nM, n=5; Fig. 15D, E). These series of experiments also further confirmed that the focused electric field at the position of A337 was stronger in the absence of ATP than in the presence of ATP shown by: (1) superimposed fluorescence traces at -140 mV for both conditions (Fig. 15F). Even though this is not significantly different, the fluorescence change had a tendency to be smaller than in the absence of ATP (p=0.07, paired t-test, Fig 15E); and (2) A linear voltage dependence of F-V relationship in the absence of ATP ($y = 0.006x - 0.074$; $R^2 = 0.99$) and in the presence of 30 μM of ATP ($y = 0.004x - 0.049$; $R^2 = 0.99$) (Fig. 15G).

Higher concentration of ATP (100 μM) was also tested for A337Anap/R313W. The results also showed fluorescence changes were larger in the absence of ATP (ΔF/F= 2.6%±0.4 at 440 nm, n=5, Fig. 16A, C) than in the presence of 100 μM ATP (ΔF/F= 0.9%±0.2 at 440 nm, n=5; Fig. 16B, C). The superimposed traces in the absence and presence of 100 μM ATP at -140 mV were shown in Fig. 16D and has been analyzed to be significantly different ($p<0.001$, paired t-test, Fig. 16C). The linear F-V relationship in 0 ATP ($y = 0.006x - 0.069$; $R^2 = 0.99$) and in 100 μM ATP ($y = 0.003x - 0.061$; $R^2 = 0.98$) showed that the focused electric field is also far weaker in 100 μM ATP. Taken together, these results from two constructs suggest that the focused electric field at A337 is [ATP]-dependent and stronger in the absence of ATP.

Anap fluorophore could exhibit electrochromic effect in site-specific manner in P2X2 receptor

Thus far, there were no reports that Anap fluorophore could exhibit electrochromic effect especially in a site-specific manner. This raised a fundamental question if Anap can truly detect

a site-specific electrochromic effect. The study in *Shaker* K^+ channel showed Di-1-ANEPIA could exhibit electrochromic effect in a site-specific manner (Asamoah et al., 2003). Di-1-ANEPIA is a derivative of ANEP chromophore, which has been shown as an electrochromic fluorophore, with the modification to produce two functional domains: the ANEP chromophore that has been proven to be a sensitive molecular indicator of transmembrane electrical events (Zhang et al., 1998) and a sulfhydryl-reactive moiety to which cysteine residues covalently bind (Asamoah et al., 2003). Anap has only been reported as an environmentally sensitive fluorophore (Lee et al., 2009; Chatterjee et al., 2013) but none reported that Anap is an electrochromic fluorophore.

Therefore, an approach to support that Anap could exhibit electrochromic effect is needed. Next the electrochromic effect of Anap was further examined by making it incorporated to the various positions which have been reportedly to show a site-specific electrochromic effect in *Shaker* K^+ channel and see if it also could report a similar electrochromic effect. TAG mutation was introduced to *Shaker* K^+ channel with the deletion of the N-terminal inactivation ball (residues 6–46 in the N terminal domain, Hoshi et al., 1990) also with T449V which diminishes the C-type inactivation (Lopez-Barneo et al., 1993). As Anap size is small and directly linked to the backbone of the protein (Lee et al., 2009; Kalstrup & Blunck, 2013; Chatterjee et al., 2013), there might be a slight positional difference from the cys-attached fluorophore. For this reason, positions at S3-S4 linker and some in the S4 region of *Shaker* K^+ channel were scanned (Fig. 17A).

TAG mutation was introduced one at a time to 10 positions in S3-S4 linker (V345, S346, K350, Q352, and M356), S4 region (A359, R362, R365, and R368), and S5-S6 linker (F425) (Fig. 17A). VCF-fUAA recording was performed by applying voltage step pulses from -100 mV to +60 mV with 10 mV increments from the holding potential of -100 mV. Results supporting that Anap has electrochromic properties were not observed. From 10 scanning

positions, only one position at the top of S4 region (A359) reported fluorescence change (ΔF/F= 2.4%±0.5 at 440 nm, n=4, Fig. 17B). Based on F-V relationship (Fig. 17C), this fluorescence changes reported depolarization-induced conformational changes of S4 as reported before in *Shaker* K^+ channel VCF-fUAA study (Kalstrup & Blunck, 2013).

Site-specific electrochromic effect is heavily based on the orientation of the fluorophore (Asamoah et al., 2003). Since the precise orientation of each fluorophore is different and also unknown in different positions or different channel proteins, it still remains possible that Anap could detect locally focused electric field by the electrochromic effect, based on the VCF results in P2X2 receptor.

A337 in TM2 might interact with F44 in TM1 to stabilize the open state of P2X2 receptor

A337 in TM2 was shown to be possibly located in the focused electric field by the results of VCF recording using Anap as fluorophore. This electric field convergence could provide us with a clue about the mechanisms of the complex gating of this receptor. Hence, various single amino acid mutations were introduced at the position of A337, and their electrophysiological properties were analyzed focusing on the [ATP]-dependent gating and also voltage-dependent gating properties (Fig. 18).

Mutations to A337R, A337K, and A337D had severe effects. When the voltage step pulses were applied in 300 μM ATP, these mutants almost lacked sensitivity to voltage (Fig. 18A). A337E, A337Y, and A337F showed voltage sensitivity with different activation kinetics. The most striking ones are A337Y and A337F. The activation evoked by a voltage step was clearly different from wildtype, whereas A337E mutation had a less severe effect. G-V relationship at 30 μM ATP for mutants and wildtype were analyzed (Fig. 18C). Normalization was done based on the maximum conductance at the highest ATP concentration (300 μM) from each construct. Here we could also see that the mutants of A337Y and A337F preferred to be

in the closed state. As the activation kinetics and gating properties were altered by the introduction of mutation at A337, this position was shown to be critical for P2X2 receptor complex gating.

Next, it was aimed to find the counter-part in TM1 domain which A337 might have interaction with during the complex gating. Based on the homology modelling of *r*P2X2 in the closed and open state, F44 in TM1 domain was shown to move towards A337 when the receptor is open (Fig. 19B, C). Various single amino acid mutations were then introduced at F44 and their [ATP]-dependent and voltage-dependent gating were analyzed (Fig. 19A).

Mutation to positively charged residues resulted in a non-functional channel and/or has a very low expression level, as the recording on day 4 didn't evoke any response to the highest concentration of ATP used in this study (300 μM). Mutation to negatively charged residues (F44E, F44D) and aromatic residues (F44Y, F44W) greatly changed the ATP-evoked response (Fig. 19A). All four mutants still opened upon the application of ATP but current decay appeared to be faster than wildtype. In addition to that, mutation to F44A also strikingly changed the gating. It showed a relatively high basal current in the absence of ATP and further responded to ATP application. Voltage-dependent gating was also changed, as seen in the lack of tail current, showing that this mutant might have a constitutive activity with rectified permeation properties (Fig. 19A).

F44 is conserved only in P2X2 and P2X3. Other subtypes of P2X receptor like P2X1, P2X4, P2X6, and P2X7 except P2X5 have valine at the corresponding position (Fig. 20A). Thus, F44V mutation was also introduced. 10 μM of ATP could activate F44V but resulted in faster current decay than wildtype (Fig. 20B). Voltage step pulses were applied during the course of current decay because there was no clear steady-state (Fig. 20C). Nonetheless, it could still be observed how the mutation at F44V changed the voltage-dependent gating. G-V relationship of F44V in 10 μM ATP showed that this mutant was far less sensitive to voltage

than wildtype (Fig. 20D). Taken together, all the mutations introduced at the position F44 showed that this residue is very important for the proper ATP- and voltage-dependent gating of P2X2 receptor.

Additionally, as the introduced single amino acid mutations at both A337 and F44 altered the gating of P2X2 it is of interest to know whether the introduction of swap mutation into A337/F44 would rescue the wildtype phenotype. The phenotype of F44A/A337F was similar to F44A and the wildtype phenotype couldn't be rescued (Fig. 21). When the voltage step pulses were applied, the swapped mutation still showed altered gating with almost no voltage-dependent activation even though the mutant it responded normally to the ATP application. It is possible that an interaction between A337 and F44 could not be properly formed in the swapped mutant.

Based on the aforementioned results above: (1) homology modelling results suggested that F44 moves towards A337 in the open state upon the binding of ATP (Fig. 19B, C; Fig. 22C, D); (2) mutagenesis studies showed that A337 and F44 are important for the gating of P2X2 receptor. Next an artificial electrostatic bridge was introduced between A337 and F44 to prove there is an interaction between them in the ATP-bound open state. Various paired electrostatically charged residues were introduced to A337 and F44, in order to see if the artificial electrostatic bridge would have been formed. F44E/A337R pair showed a constitutive activity. This paired mutant already opened before ATP application and didn't give any response when the ATP was applied (Fig. 22A). When the voltage step pulses were applied, this mutant lacks the sensitivity to voltage with a rectified permeation property (Fig. 22A). The results confirmed that A337 in TM2 domain might interact with F44 in TM1 to stabilize the open state of P2X2 receptor.

VCF-fUAA experiments suggested that A337 and I341 are in the focused electric field. This focused electric field at A337 is [ATP]-dependent and stronger in the absence of ATP.

From the homology modeling of *r*P2X2, in the open state upon ATP binding F44 moves into the converged electric field. Mutation studies showed that A337 and F44 are important for the gating and might interact to stabilize the open state. Taken together, these results might give an insight on the mechanisms of P2X2 receptor complex gating as well as the roles of each TM domain.

Discussion

The initial aim of this study was to detect the ATP- and voltage-dependent structural rearrangements of P2X2 receptor. For this purpose, a fluorescent unnatural amino acid, Anap, was incorporated into P2X2 protein in *Xenopus* oocyte expression system by a genetic method, to overcome the limitations by the usage of conventional fluorophore (e.g. Alexa-488) for VCF analyses. This approach brought the following findings. (1) Anap was successfully incorporated into P2X2 receptor shown by simultaneously recorded (i) ATP- and voltage- evoked current as well as (ii) Anap fluorescence signal. (2) SIK inhibitor (HG-9-91-01) treatment improved VCF-fUAA optical signal (Figs. 8, 9). (3) Anap was introduced to 96 positions of P2X2 in total, one at a time, and voltage-dependent fluorescence changes of Anap was observed only at A337 and I341 in the TM2 domain. (4) The changes showed a linear voltage-dependence and exhibited extremely fast kinetics in ms order. It looks as if the fluorescence signals directly respond to membrane voltage itself, indicating a phenomenon related to electrochromic effect rather than protein structure rearrangements (Figs. 10, 11). (5) The electrochromic effect observed only at A337 and I341 and not at other residues implies that the electric field of the membrane is converged at these positions. (6) The focused electric field at A337 was observed both in the absence and presence of ATP. And it was stronger in the absence of ATP, reflecting ATP dependent structural changes (Figs. 12-16). (7) Mutagenesis studies at A337 and F44 showed that the interaction between A337 in TM2 and F44 in TM1 in the ATP-bound open state is important for the complex gating (Figs. 18-23). (8) It is possible that F44 swings into the focused electric field and that the interaction between A337 and F44 upon ATP binding, which contributes to the opening, might be under the control of membrane voltage.

SIK inhibitor treatment improved VCF-fUAA optical signal

Xenopus oocytes are the standard expression system for VCF experiments as they generally generate less autofluorescence than mammalian cells due to its darker animal pole as well as they offer a large surface area to maximize the emissions intensity (Manuzzu et al., 1996; Pless & Lynch 2008; Talwar & Lynch 2015). However, in some cases, optical measurements are also currently limited in sensitivity, which could be due to the high intrinsic background fluorescence of oocytes in the 300 – 500 nm wavelength range. This could decrease the signal-to-noise ratio since the VCF recordings are performed in this range (Lee & Bezanilla 2019).

Melanin is a dark-pigmented molecule which plays a role in protection from UV radiation (Costin & Hearing 2007). Melanin is expressed intrinsically in oocytes which made its animal pole darker than its vegetal pole. Thus the animal pole has less autofluorescence compared to the vegetal pole or the mammalian cells. SIK inhibitor was used to artificially increase the melanin content of the oocyte to further decrease the endogenous fluorescence signal in VCF recording (Lee & Bezanilla 2019). SIK inhibitor (HG-9-91-01) induced MITF, the master regulator of pigment genes, which promotes UV-independent skin pigmentation (Mujahid et al., 2017).

A previous study showed that the application of 100 μM SIK inhibitor increased the voltage-dependent fluorescence signal in *Shaker* K^+ channel which was labeled by ATTO 425 fluorophore. This is mainly due to the decrease in background fluorescence by the effect of SIK inhibitor (Lee & Bezanilla 2019). In the present study, there were some obstacles in the initial VCF-fUAA recordings where the signals were poorly generated and resulted in small fluorescence changes as well as the low incidence of the detectable changes (Fig. 7A, B). This might be due to the intrinsic background fluorescence of the oocytes, as the Anap fluorophore emits the maximum emission at 440 nm. SIK inhibitor treatment was thus applied in this study.

The application of 300 nM SIK inhibitor improved the optical signal as the fluorescence change was two times larger than the non-treated one in the VCF recordings of *Ci*-VSP which was labeled by Anap fluorophore (Fig. 8A-E). In the case of P2X2, SIK inhibitor treatment didn't significantly increase the percentage of fluorescence change of VCF recordings but rather improved the signal-to-noise ratio in that it increased the incidence of successful detection of change (Fig. 9A-E).

The discrepancy of the amount of the SIK inhibitor concentration which were used in two studies might be due to the different site of injection in the oocytes. In Anap experiment, SIK inhibitor was co-injected into the nucleus instead of cytoplasm and was incubated longer than the reported one. Regardless, even though the concentration used was different, both results showed the increase in the optical recording as: (1) the percentage of the fluorescence signal change and/or (2) the incidence of fluorescence change detection were higher, which were thought to be due to the decrease of the intrinsic background fluorescence of the oocyte.

Voltage-dependent fluorescence changes of Anap at A337 and I341 were not related to hyperpolarization-induced conformational change but rather reflected a phenomenon related to electrochromic effect

It was reported that the activation of P2X2 channel not only depends on [ATP] but also depends on voltage. In the presence of ATP at a steady state, there is a gradual increase in the hyperpolarization-induced inward current. (Nakazawa et al., 1997; Zhou & Hume, 1998; Nakazawa & Ohno, 2005; Fujiwara et al., 2009; Keceli & Kubo, 2009). According to the solved crystal structures of *zf*P2X4 and *h*P2X3 (Kawate et al., 2009; Hattori & Gouaux, 2012; Mansoor et al., 2016), P2X receptor doesn't possess a canonical voltage-sensing domain. The canonical VSD in voltage-gated ion channels consists of transmembrane segment of S1-S4 (Jiang et al.,

2003; Swartz 2008). Thus, the voltage-sensing mechanism in P2X2 receptor which is a part of the complex gating remains unsolved.

In P2X2 receptor, it was reported previously that upon binding of ATP, the occupied binding site indirectly interacts with the extracellular end of the TM regions to trigger conformational changes for gating in a voltage-dependent manner (Keceli & Kubo, 2009). The extracellular linker plays important roles in transmitting the signal from the ATP binding pocket (ECD domain) to the TM domains (Cao et al., 2007; Kawate et al., 2011; Du, J et al., 2012; Stelmashenko et al., 2014). This was also shown by mutagenesis study using tandem trimeric constructs in P2X2 receptor to investigate how the signal from ATP activation is transmitted within the receptor (Keceli and Kubo, 2014). Thus, Anap mutant scanning was done in all regions of the receptor, especially highlighting the entire TM1 and TM2 domain as the most possible candidate which is responsible for voltage sensing mechanism.

VCF-fUAA recording in this study scanned as many as 96 positions. There were only two positions, A337 and I341, located in TM2 domain which reported Anap fluorescence change upon voltage changes (Figs. 10, 11). The voltage-evoked fluorescence changes at A337 and I341 showed two distinct characteristics: (1) F-V relationship upon voltage step pulses showed a linear voltage-dependence. (2) Fluorescence change occurred almost instantaneously in less than 5 ms time scale. It showed that the kinetics of $\Delta F/F$ are very rapid and faster than the time course of voltage-dependent current activation (ΔF-fast). These analysis of fluorescence changes at A337 and I341 indicated that the fluorescence change is not associated with the protein conformational changes. Rather, these kind of changes are thought to be due to a phenomenon related to electrochromic effect.

Electrochromic effect is an intrinsic properties exhibited by voltage-sensitive fluorescent dye or electrochromic probes to directly detect the transmembrane potentials (Loew, 1982; Zhang et al., 1998). By standard electrochromic probes in lipid bilayer, it is hard to sense

the electrical potential that directly act on the voltage-sensing machinery (Asamoah et al., 2003). It is because the local electric field at a certain position of lipid bilayer is not steep enough.

On the other hand, previous VCF studies in *Shaker* K^+ channel using modified electrochromic probes (Asamoah et al., 2003) and in M_2 muscarinic receptor using TMRM (Dekel et al., 2012) showed that electrochromic effect could also be observed when the fluorophore is directly attached at a certain position within the ion channel / receptor. It didn't report conformational changes of protein at a position where the fluorophore was attached, but rather implied that there is an electric field convergence (Asamoah et al., 2003).

Another VCF study using MTS-TAMRA in canonical VSD containing membrane protein named hTMEM266 also reported the linear F-V and ΔF-fast. These characteristics of fluorescence change were observed at most of the introduced positions located in the S3-S4 linker and the top of S4 segment (Papp et al., 2019). It was stated, however, that the observed ΔF-fast is not due to direct electrochromic effect because the study showed evidences supporting ΔF-fast was instead associated with the rapid voltage-dependent conformational rearrangements in μs time scale.

In the case of hTMEM266, if the observed fluorescence changes were instead interpreted as electrochromic effect, it is hard to imagine if the electric field was converged at so many positions. Conversely, in P2X2 receptor there were only two adjacent positions which exclusively showed ΔF-fast and linear F-V relationship. Moreover, the linearity of F-V relationship in hTMEM266 study was not necessarily linear compared to the observed fluorescence changes in P2X2. Even though other possibilities could still remain, the most possible explanation to interpret the results observed in this study is that the fluorescence change is associated with electrochromic phenomenon. Thus, the observed fluorescence change at the position of A337 and I341 in P2X2 receptor reflects the electrochromic effect, implying that there is a focused electric field convergence at A337 and I341 in TM2 domain.

The focused electric field at A337 was observed both in the absence and presence of ATP

VCF-fUAA recording with voltage step pulses in the absence of ATP was performed to test whether the fluorescence changes upon voltage change observed at A337 is not due to the ion-flux like in the case of K2P K^+ channel (Schewe et al., 2013). Results showed that Anap fluorescence changes were also observed even in the absence of ATP, implying that the focused electric field is already present in the absence of ATP. This focused electric field was even stronger in the absence of ATP than in the presence of ATP (Fig. 12).

As A337Anap mutant has a relatively high basal activity even in the absence of ATP, additional mutation at extracellular linker at β-14 was introduced in order to suppress the basal activity and to better analyze the focused electric field in the closed state. The residue that is important for ATP evoked gating is located at the upper ends of β strands of β-14 in body domain which is connected directly to TM2 (Cao et al., 2007; Kawate et al., 2011; Du, J et al., 2012; Stelmashenko, et al., 2014). A mutant of R313 at β-14 to either phenylalanine or tryptophan altered the channel gating as it became harder to open compared to wildtype (Fig. 13A, B; Fig. 15A, B).

The results of A337Anap/R313F and A337Anap/R313W mutants with lower basal activity in the absence of ATP further confirmed that focused electric field is already present in the closed state. This focused electric field was [ATP]-dependent and stronger in the absence of ATP (Figs. 13-16).

Anap fluorophore could exhibit electrochromic effect in a site-specific manner in P2X2 receptor

The study in *Shaker* K^+ channel showed Di-1-ANEPIA fluorophore could exhibit electrochromic effect in a site-specific manner where it directly attached through cysteine binding at certain positions in the canonical VSD (S1-S4 region) of *Shaker* K^+ channel

(Asamoah et al., 2003). However, Anap had only been reported as an environmentally sensitive fluorophore, suitable to detect structural rearrangement of proteins, but none had reported that Anap is a voltage-sensitive fluorophore (Lee et al., 2009; Chatterjee et al., 2013). From the positive control using *Ci*-VSP it confirmed that Anap is an environmentally sensitive fluorophore which could detect the change in surrounding environment when the conformational changes upon depolarization (Fig. 4). This raised a fundamental question if Anap can truly detect a site-specific electrochromic effect as observed in the present study.

The ability of Anap to detect the electrochromic effect in a site-specific manner was further examined by making Anap incorporated to various positions of *Shaker* K^+ channel at which a site-specific electrochromic effect by Di-1-ANEPIA was observed. The results couldn't support that Anap has electrochromic properties, as none of 10 introduced positions showed similar results observed in Di-1-ANEPIA fluorophore (Fig. 17). As Anap is small in size and directly linked to the backbone of the protein (Lee et al., 2009; Kalstrup & Blunck, 2013; Chatterjee et al., 2013), the exact position might differ from the cys-attached Di-1-ANEPIA fluorophore.

Interaction between A337 in TM2 and F44 in TM1 in the open (ATP-bound) state is important for the complex gating

Specific function of each transmembrane domain of P2X receptor had been defined before the crystal structure was solved. TM1 had a role in binding-gating process as site-directed mutagenesis study in this region alters agonist selectivity of channel gating (Haines et al., 2001). This was strengthened by alanine substitution mutagenesis of each residue in TM1, some of which resulted in altered potencies, and two mutants were active even in the absence of agonist (Y43A and F44A) (Li et al., 2004). This was further supported by the study which showed that

the lower part of body domain connected to TM1 (β1 and β-8) is involved in ATP evoked gating (Stelmashenko et al., 2014).

In contrast, TM2 contains residues that regulate specific properties of ion flow through the channel including conductance where N333, which is believed to be involved in the channel pore, plays an essential role in permeation through P2X2 receptor (Nakazawa et al., 1998; Khakh et al., 2005) and gating (Khakh et al., 1999; Li et al., 2008; Virginio et al., 2009). Cys-accessibility study using P2X2 receptor showed that TM2 lines the central ion-conduction pore, while TM1 is positioned peripheral to TM2 and the flow of ions is minimized in the closed-state by a gate formed by the external region of TM2 (Li et al., 2008). However, the contribution of each transmembrane domain of P2X receptor in the complex gating which involves ATP and also voltage has not been defined yet. The present study showed that the interaction between A337 in TM2 and F44 in TM1 in the focused electric field in the ATP-bound open state is important for the complex gating of P2X2 receptor.

Several Cys accessibility approaches were performed in TM2 domain to analyze the ATP-evoked gating mechanism of P2X receptors. Some of them were on P2X2 receptor (Li, et al., 2008; Li, et al., 2010; Kracun, et al., 2010). A337 Cys mutants were first reported to be not modified by thiol reactive compounds (MTSET) both in the presence or absence of ATP, indicating that these residues are not involved either in the lining of the pore in the open state or in the gate of P2X2 (Li, et al., 2008). Meanwhile in other study using Ag^{+}, a smaller thiol reactive ions with higher accessibility, A337C was modified both in the absence and presence of ATP (Li et al., 2010). These results suggest that narrow water-phase is penetrated down to this position, which is consistent with the results in this study that there is a focused electric field at A337. Mutagenesis study suggested that this position is important for the complex gating as mutation to A337F and A337Y altered the channel gating as well as the activation kinetics upon the application of ATP and voltage (Fig. 18).

On the other hand, mutagenesis study at the position of F44 suggested the importance of F44 for decelerating the current decay in the presence of ATP. Most of the mutants (F44E, F44D, F44W, F44Y and F44V) had a faster current decay compared to wildtype. F44A showed a slight activity in the absence of ATP with further activation by ATP application (Figs. 19-20). These results go well with previously reported studies that F44A is basically active even in the absence of agonist (Li et al., 2004; Keceli & Kubo 2009).

F44C was reported to have a slow voltage-dependent activation by low [ATP] and have a constitutive activity even at depolarized potential in higher [ATP] (Keceli & Kubo, 2009). Another study reported that by mutating F44 to cysteine resulted in a 10-fold increase in sensitivity to ATP. A direct effect of F44C mutation to channel gating was also indicated by the ATP-evoked current which deactivated slowly upon wash-out of ATP which is consistent with slowed channel closing (Jiang et al., 2001). Taken together with the results in the present study, F44 is important for the proper ATP- and voltage dependent gating.

In the homology modelling of *r*P2X2 which derived from the crystal structure of *h*P2X3, F44 undergoes a major structural rearrangements from the closed to open state. In the closed state, this position facing to the other side of the TM2, but upon the ATP binding TM1 rotates and F44 tilts toward TM2, in a close proximity of A337 (Fig. 19B, C). The introduction of an artificial electrostatic bridge in the F44E/A337R double mutant induced the constitutive activity in the absence of ATP and at all voltages, confirming the dynamic interaction between A337 and F44 during the complex gating of the receptor (Fig. 22).

Additionally, F44 is found only in the P2X2 and P2X3 subunits. In other P2X family members, the residue is mostly valine or either leucine or isoleucine (Fig. 20A). F44V mutation showed an interesting effect in term of the receptor complex gating. When voltage step pulses were applied in the presence of ATP, this mutant is active at all voltages with no voltage-dependent activation (Fig. 20B, C). This raised a question if the complex gating is a property

of P2X2 and P2X2/3 heteromultimer only, as other P2X subtypes have valine at the corresponding position (Fig. 20A). Further analysis in other subtypes could strengthen the importance of F44 in the voltage-dependent activation.

Mechanisms of P2X2 receptor complex gating

Present study aims at defining the roles of TM domains of P2X2 receptor in the receptor complex gating involving [ATP] and voltage, using VCF and mutagenesis study approach, the followings are shown. First, the VCF results in the closed state showed that there is voltage-dependent fluorescence changes which can be due to the electrochromic effect, implying the presence of focused electric field at the position of A337. Second, in the ATP-bound open state, there were also indication of focused electric field at A337 and I341, which is weaker than that in the closed state. Third, in the ATP-bound open state, the position of F44 moves towards TM2, specifically to the proximity with A337. As shown by the artificial electrostatic bridge formation experiment (Fig. 22), the interaction between A337 and F44 is important for stabilizing the open state.

Taken together, the results provide us with a clue on the initiation of P2X2 complex gating based on two main findings in this study: (1) the electric field convergence at A337 and I341 (Fig. 23C) and (2) Movement of F44 towards A337 in TM2 domain upon ATP binding (Fig. 23 A, B). The stability of the interaction between A337 and F44 in the focused electric field will be influenced by voltage.

There are several ways in which proteins can sense voltage (Bezanilla, 2008): (1) charged residues as they can reorientate in the field like in the case of canonical VSD in voltage-gated ion channel; (2) side chains that have intrinsic dipole moment such as Tyr might also orientate in the electric field, like in the case of M_2 muscarinic receptor (Barchad-Avitzur et al., 2016); and (3) the α-helix with its intrinsic dipole moment represents a potential voltage-sensing

structure by reorientating in the field, although not yet identified as voltage sensor. Based on our findings, the interaction between A337 and F44 in the ATP-bound open state might be under the influence of the converged electric field. At this point, the detail about how the interaction contributes to the voltage sensing mechanism cannot be answered yet. Further analysis of the position of F44 will elucidate the mechanism of the complex gating of P2X2 receptor.

Concluding Remarks

To detect the ATP- and voltage-dependent structural rearrangements of the rat P2X2 receptor, a fluorescent unnatural amino acid, Anap, was directly incorporated into P2X2 protein in *Xenopus* oocyte expression system by a genetic method. This was done in order to overcome the limitations by the usage of conventional fluorophore for VCF analyses. This approach brought the following findings.

1. Anap was successfully incorporated into P2X2 receptor as shown by simultaneously recorded (i) ATP- and voltage- evoked current as well as (ii) Anap fluorescence signal.
2. Voltage-dependent Anap fluorescence changes were observe at A337 and adjacent I341 in TM2, which indicates there is an electric field convergence at both positions.
3. The focused electric field at A337 was observed both in the absence and presence of ATP, and it was stronger in the absence of ATP.
4. The interaction between A337 in TM2 and F44 in TM1 in the open (ATP-bound) state is important for the complex gating and it could be under the influence of the focused electric field.

Acknowledgements

First of all, I would like to express my sincere gratitude to Prof. Yoshihiro Kubo for the continuous support of my Ph.D study, for his patience, motivation, and immense knowledge. His guidance helped me in all the time of research and writing of this thesis.

I would like to thank Prof. David Julius (University of California, San Francisco) for generously providing cDNA encoding rat P2X2. I would also like to thank Prof. Yasushi Okamura (Osaka University) for generously providing cDNA encoding *Ci*-VSP mutants for VCF experiment, as well as Prof. Lily Jan (University of California, San Francisco) for the *Shaker* B K^+ channel cDNA.

I would like to thank former Kubo lab member Prof. Koichi Nakajo, as well as Dr. Michihiro Tateyama, Dr. Takushi Shimomura, and Dr. I-Shan Chen in Kubo lab for their insightful comments and continuous encouragements. I would like to thank former Kubo lab member Dr. Shinichiro Kume, my fellow lab members Liu Chang and Ki-ichi Hirazawa for the stimulating discussions, for the kind help, support and for the friendship. I would also like to thank Tomomi Yamamoto and Chizue Naito for their kind help in the lab.

I would like to thank Sarlita, Albert, Median, Anisa Pelangi, Fawzia, Zlata, Mega, Fitria, Defri, Qonita, Anisa Fitri and Dwi for their unconditional friendship and support throughout this thesis work.

Last but not the least, I would like to thank my family: my parents, my brothers, and all Atmadinata family members for their unconditional love and support.

References

Arnold, K., Bordoli, L., J, K., & Schwede, T. (2006). The SWISS Model workspace: a web-based environment for protein structure homology modelling *Bioinformatics, 22*, 195-201.

Asamoah, O. K., Wuskell, J. P., Loew, L. M., & Bezanilla, F. (2003). A Fluorometric Approach to Local Electric Field Measurements in a Voltage-Gated Ion Channel. *Neuron, 37*(1), 85-98.

Barchad-Avitzur, O., Priest, M. F., Dekel, N., Bezanilla, F., Parnas, H., & Ben-Chaim, Y. (2016). A Novel Voltage Sensor in the Orthosteric Binding Site of the M2 Muscarinic Receptor. *Biophysical Journal, 111*(7), 1396-1408.

Ben-Chaim, Y., Chanda, B., Dascal, N., Bezanilla, F., Parnas, I., & Parnas, H. (2006). Movement of 'gating charge' is coupled to ligand binding in a G-protein-coupled receptor. *Nature, 444*(7115), 106-109.

Bernier, L. P., Blais, D., Boue-Grabot, E., & Seguela, P. (2012). A dual polybasic motif determines phosphoinositide binding and regulation in the P2X channel family. *PLoS One, 7*(7), e40595.

Bezanilla, F. (2008). How membrane proteins sense voltage. *Nature Reviews Molecular Cell Biology, 9*, 323.

Biasini, M., Bienert, S., Waterhouse, A., Arnold, K., Studer, G., Schmidt, T., Bordoli, L., & Schwede, T. (2014). SWISS MODEL: modelling protein tertiary and quaternary structure using evolutionary information. *Nucleic Acid Research, 42*, 252-258.

Boue-Grabot, E., Emerit, M. B., Toulme, E., Seguela, P., & Garret, M. (2004). Cross-talk and co-trafficking between rho1/GABA receptors and ATP-gated channels. *J Biol Chem, 279*(8), 6967-6975.

Boue-Grabot, E., Toulme, E., Emerit, M. B., & Garret, M. (2004). Subunit-specific coupling between gamma-aminobutyric acid type A and P2X2 receptor channels. *J Biol Chem, 279*(50), 52517-52525.

Brake, A. J., Wagenbach, M. J., & Julius, D. (1994). New structural motif for ligand-gated ion channels defined by an ionotropic ATP receptor. *Nature, 371*(6497), 519-523.

Burnstock, G. (2003). Introduction: ATP and Its Metabolites as Potent Extracellular Agents *Current Topics in Membranes* (Vol. 54, pp. 1-27): Academic Press.

Cao, L., Broomhead, H. E., Young, M. T., & North, R. A. (2009). Polar residues in the second transmembrane domain of the rat P2X2 receptor that affect spontaneous gating, unitary conductance, and rectification. *J Neurosci, 29*(45), 14257-14264.

Cao, L., Young, M. T., Broomhead, H. E., Fountain, S. J., & North, R. A. (2007). Thr339-to-serine substitution in rat P2X2 receptor second transmembrane domain causes constitutive opening and indicates a gating role for Lys308. *J Neurosci, 27*(47), 12916-12923.

Chatterjee, A., Guo, J., Lee, H. S., & Schultz, P. G. (2013). A genetically encoded fluorescent probe in mammalian cells. *J Am Chem Soc, 135*(34), 12540-12543.

Chaumont, S., Jiang, L. H., Penna, A., North, R. A., & Rassendren, F. (2004). Identification of a trafficking motif involved in the stabilization and polarization of P2X receptors. *J Biol Chem, 279*(28), 29628-29638.

Coddou, C., Yan, Z., Obsil, T., Huidobro-Toro, J. P., & Stojilkovic, S. S. (2011). Activation and regulation of purinergic P2X receptor channels. *Pharmacol Rev, 63*(3), 641-683.

Costin, G.-E., & Hearing, V. J. (2007). Human skin pigmentation: melanocytes modulate skin color in response to stress. *The FASEB Journal, 21*(4), 976-994.

Dekel, N., Priest, M. F., Parnas, H., Parnas, I., & Bezanilla, F. (2012). Depolarization induces a conformational change in the binding site region of the M2 muscarinic receptor. *Proc*

Natl Acad Sci U S A, 109(1), 285-290.

Ding, S., & Sachs, F. (2000). Inactivation of P2X2 purinoceptors by divalent cations. *J Physiol, 522 Pt 2*(Pt 2), 199-214.

Du, J., Dong, H., & Zhou, H. X. (2012). Gating mechanism of a P2X4 receptor developed from normal mode analysis and molecular dynamics simulations. *Proc Natl Acad Sci U S A, 109*(11), 4140-4145.

Egan, T. M., Samways, D. S., & Li, Z. (2006). Biophysics of P2X receptors. *Pflugers Arch, 452*(5), 501-512.

Emerit, M. B., Baranowski, C., Diaz, J., Martinez, A., Areias, J., Alterio, J., Masson, J., Boue-Grabot, E., & Darmon, M. (2016). A New Mechanism of Receptor Targeting by Interaction between Two Classes of Ligand-Gated Ion Channels. *J Neurosci, 36*(5), 1456-1470.

Fujiwara, Y., Keceli, B., Nakajo, K., & Kubo, Y. (2009). Voltage- and [ATP]-dependent gating of the P2X(2) ATP receptor channel. *J Gen Physiol, 133*(1), 93-109.

Fujiwara, Y., & Kubo, Y. (2004). Density-dependent changes of the pore properties of the P2X2 receptor channel. *J Physiol, 558*(Pt 1), 31-43.

Habermacher, C., Martz, A., Calimet, N., Lemoine, D., Peverini, L., Specht, A., Cecchini, M., & Grutter, T. (2016). Photo-switchable tweezers illuminate pore-opening motions of an ATP-gated P2X ion channel. *Elife, 5*, e11050.

Haines, W. R., Migita, K., Cox, J. A., Egan, T. M., & Voigt, M. M. (2001). The first transmembrane domain of the P2X receptor subunit participates in the agonist-induced gating of the channel. *J Biol Chem, 276*(35), 32793-32798.

Hattori, M., & Gouaux, E. (2012). Molecular mechanism of ATP binding and ion channel activation in P2X receptors. *Nature, 485*(7397), 207-212.

Heymann, G., Dai, J., Li, M., Silberberg, S. D., Zhou, H. X., & Swartz, K. J. (2013). Inter- and

intrasubunit interactions between transmembrane helices in the open state of P2X receptor channels. *Proc Natl Acad Sci U S A, 110*(42), E4045-4054.

Hoshi, T., Zagotta, W., & Aldrich, R. (1990). Biophysical and molecular mechanisms of Shaker potassium channel inactivation. *Science, 250*(4980), 533-538.

Housley, G. D., Morton-Jones, R., Vlajkovic, S. M., Telang, R. S., Paramananthasivam, V., Tadros, S. F., Wong, A. C. Y., Froud, K. E., Cederholm, J. M. E., Sivakumaran, Y., Snguanwongchai, P., Khakh, B. S., Cockayne, D. A., Thorne, P. R., & Ryan, A. F. (2013). ATP-gated ion channels mediate adaptation to elevated sound levels. *Proc Natl Acad Sci U S A, 110*(18), 7494-7499.

Jiang, L. H., Rassendren, F., Spelta, V., Surprenant, A., & North, R. A. (2001). Amino acid residues involved in gating identified in the first membrane-spanning domain of the rat P2X(2) receptor. *J Biol Chem, 276*(18), 14902-14908.

Jiang, Y., Lee, A., Chen, J., Ruta, V., Cadene, M., Chait, B. T., & MacKinnon, R. (2003). X-ray structure of a voltage-dependent K+ channel. *Nature, 423*(6935), 33-41.

Kaczmarek-Hajek, K., Lorinczi, E., Hausmann, R., & Nicke, A. (2012). Molecular and functional properties of P2X receptors--recent progress and persisting challenges. *Purinergic Signal, 8*(3), 375-417.

Kalstrup, T., & Blunck, R. (2013). Dynamics of internal pore opening in K_V channels probed by a fluorescent unnatural amino acid. *Proc Natl Acad Sci U S A, 110*(20), 8272-8277.

Kawate, T., Michel, J. C., Birdsong, W. T., & Gouaux, E. (2009). Crystal structure of the ATP-gated P2X(4) ion channel in the closed state. *Nature, 460*(7255), 592-598.

Kawate, T., Robertson, J. L., Li, M., Silberberg, S. D., & Swartz, K. J. (2011). Ion access pathway to the transmembrane pore in P2X receptor channels. *J Gen Physiol, 137*(6), 579-590.

Keceli, B., & Kubo, Y. (2009). Functional and structural identification of amino acid residues of the P2X2 receptor channel critical for the voltage- and [ATP]-dependent gating. *J Physiol, 587*(Pt 24), 5801-5818.

Keceli, B., & Kubo, Y. (2014). Signal transmission within the P2X2 trimeric receptor. *J Gen Physiol, 143*(6), 761-782.

Khakh, B. S., & Egan, T. M. (2005). Contribution of transmembrane regions to ATP-gated P2X2 channel permeability dynamics. *J Biol Chem, 280*(7), 6118-6129.

Khakh, B. S., & North, R. A. (2012). Neuromodulation by extracellular ATP and P2X receptors in the CNS. *Neuron, 76*(1), 51-69.

Khakh, B. S., Zhou, X., Sydes, J., Galligan, J. J., & Lester, H. A. (2000). State-dependent cross-inhibition between transmitter-gated cation channels. *Nature, 406*(6794), 405-410.

Kracun, S., Chaptal, V., Abramson, J., & Khakh, B. S. (2010). Gated access to the pore of a P2X receptor: structural implications for closed-open transitions. *J Biol Chem, 285*(13), 10110-10121.

Lee, E. E. L., & Bezanilla, F. (2019). Methodological improvements for fluorescence recordings in Xenopus laevis oocytes. *J Gen Physiol, 151*(2), 264-272.

Lee, H. S., Guo, J., Lemke, E. A., Dimla, R. D., & Schultz, P. G. (2009). Genetic incorporation of a small, environmentally sensitive, fluorescent probe into proteins in Saccharomyces cerevisiae. *J Am Chem Soc, 131*(36), 12921-12923.

Li, M., Chang, T. H., Silberberg, S. D., & Swartz, K. J. (2008). Gating the pore of P2X receptor channels. *Nat Neurosci, 11*(8), 883-887.

Li, M., Kawate, T., Silberberg, S. D., & Swartz, K. J. (2010). Pore-opening mechanism in trimeric P2X receptor channels. *Nat Commun, 1*, 44.

Li, Z., Migita, K., Samways, D. S. K., Voigt, M. M., & Egan, T. M. (2004). Gain and Loss of Channel Function by Alanine Substitutions in the Transmembrane Segments of the Rat

ATP-Gated P2X2 Receptor. *The Journal of Neuroscience, 24*(33), 7378-7386.

Lin-Moshier, Y., & Marchant, J. S. (2013). Nuclear microinjection to assess how heterologously expressed proteins impact Ca2+ signals in Xenopus oocytes. *Cold Spring Harb Protoc, 2013*(3).

Liu, L., Kohout, S. C., Xu, Q., Muller, S., Kimberlin, C. R., Isacoff, E. Y., & Minor, D. L., Jr. (2012). A glutamate switch controls voltage-sensitive phosphatase function. *Nat Struct Mol Biol, 19*(6), 633-641.

Loew, L. M. (1982). Design and characterization of electrochromic membrane probes. *Journal of Biochemical and Biophysical Methods, 6*(3), 243-260.

Lopez-Barneo, J., Hoshi, T., Heinemann, S. H., & Aldrich, R. W. (1993). Effects of External Cations and Mutations in the Pore Region on C-Type Inactivation of *Shaker* Potassium Channels. *Receptor and Channels, 1*(1), 61-71.

Mannuzzu, L. M., Moronne, M. M., & Isacoff, E. Y. (1996). Direct Physical Measure of Conformational Rearrangement Underlying Potassium Channel Gating. *Science, 271*(5246), 213-216.

Mansoor, S. E., Lu, W., Oosterheert, W., Shekhar, M., Tajkhorshid, E., & Gouaux, E. (2016). X-ray structures define human P2X(3) receptor gating cycle and antagonist action. *Nature, 538*(7623), 66-71.

Mujahid, N., Liang, Y., Murakami, R., Choi, H. G., Dobry, A. S., Wang, J., Suita, Y., Weng, Q. Y., Allouche, J., Kemeny, L. V., Hermann, A. L., Roider, E. M., Gray, N. S., & Fisher, D. E. (2017). A UV-Independent Topical Small-Molecule Approach for Melanin Production in Human Skin. *Cell Reports, 19*(11), 2177-2184.

Nakajo, K., & Kubo, Y. (2014). Steric hindrance between S4 and S5 of the KCNQ1/KCNE1 channel hampers pore opening. *Nat Commun, 5*, 4100.

Nakazawa, K., Inoue, K., & Ohno, Y. (1998). An asparagine residue regulating conductance

through P2X2 receptor/channels. *European Journal of Pharmacology, 347*(1), 141-144.

Nakazawa, K., Liu, M., Inoue, K., & Ohno, Y. (1997). Voltage-Dependent Gating of ATP-Activated Channels in PC12 Cells. *Journal of Neurophysiology, 78*(2), 884-890.

Nakazawa, K., & Ohno, Y. (2005). Characterization of voltage-dependent gating of P2X2 receptor/channel. *European Journal of Pharmacology, 508*(1), 23-30.

Navarro-Polanco, R. A., Moreno Galindo, E. G., Ferrer-Villada, T., Arias, M., Rigby, J. R., Sanchez-Chapula, J. A., & Tristani-Firouzi, M. (2011). Conformational changes in the M2 muscarinic receptor induced by membrane voltage and agonist binding. *J Physiol, 589*(Pt 7), 1741-1753.

Omasits, U., Ahrens CH, Müller S, & B, W. (2014). Protter: interactive protein feature visualization and integration with experimental proteomic data. *Bioinformatics, 30*(6), 884-886.

Papp, F., Lomash, S., Szilagyi, O., Babikow, E., Smith, J., Chang, T. H., Bahamonde, M. I., Toombes, G. E. S., & Swartz, K. J. (2019). TMEM266 is a functional voltage sensor regulated by extracellular Zn(2). *Elife, 8*.

Pless, S. A., & Lynch, J. W. (2008). Illuminating the Structure and Function of Cys-Loop Receptors. *Clinical and Experimental Pharmacology and Physiology, 35*(10), 1137-1142.

Pougnet, J. T., Toulme, E., Martinez, A., Choquet, D., Hosy, E., & Boue-Grabot, E. (2014). ATP P2X receptors downregulate AMPA receptor trafficking and postsynaptic efficacy in hippocampal neurons. *Neuron, 83*(2), 417-430.

Sakata, S., Jinno, Y., Kawanabe, A., & Okamura, Y. (2016). Voltage-dependent motion of the catalytic region of voltage-sensing phosphatase monitored by a fluorescent amino acid. *Proc Natl Acad Sci U S A, 113*(27), 7521-7526.

Schewe, M., Nematian-Ardestani, E., Sun, H., Musinszki, M., Cordeiro, S., Bucci, G., de Groot,

B. L., Tucker, S. J., Rapedius, M., & Baukrowitz, T. (2016). A Non-canonical Voltage-Sensing Mechanism Controls Gating in K2P K(+) Channels. *Cell, 164*(5), 937-949.

Schmid, R., & Evans, R. J. (2019). ATP-Gated P2X Receptor Channels: Molecular Insights into Functional Roles. *Annual Review of Physiology, 81*(1), 43-62.

Stelmashenko, O., Compan, V., Browne, L. E., & North, R. A. (2014). Ectodomain movements of an ATP-gated ion channel (P2X2 receptor) probed by disulfide locking. *J Biol Chem, 289*(14), 9909-9917.

Swartz, K. J. (2008). Sensing voltage across lipid membranes. *Nature, 456*, 891.

Talwar, S., & Lynch, J. W. (2015). Investigating ion channel conformational changes using voltage clamp fluorometry. *Neuropharmacology, 98*, 3-12.

Vial, C., Roberts, J. A., & Evans, R. J. (2004). Molecular properties of ATP-gated P2X receptor ion channels. *Trends Pharmacol Sci, 25*(9), 487-493.

Virginio, C., MacKenzie, A., Rassendren, F. A., North, R. A., & Surprenant, A. (1999). Pore dilation of neuronal P2X receptor channels. *Nature Neuroscience, 2*(4), 315-321.

Yan, D., Zhu, Y., Walsh, T., Xie, D., Yuan, H., Sirmaci, A., Fujikawa, T., Wong, A. C. Y., Loh, T. L., Du, L., Grati, M. h., Vlajkovic, S. M., Blanton, S., Ryan, A. F., Chen, Z.-Y., Thorne, P. R., Kachar, B., Tekin, M., Zhao, H.-B., Housley, G. D., King, M.-C., & Liu, X. Z. (2013). Mutation of the ATP-gated P2X2 receptor leads to progressive hearing loss and increased susceptibility to noise. *Proc Natl Acad Sci U S A, 110*(6), 2228-2233.

Zhang, J., Davidson, R. M., Wei, M.-d., & Loew, L. M. (1998). Membrane Electric Properties by Combined Patch Clamp and Fluorescence Ratio Imaging in Single Neurons. *Biophysical Journal, 74*(1), 48-53.

Zhou, Z., & Hume, R. I. (1998). Two mechanisms for inward rectification of current flow through the purinoceptor P2X2 class of ATP-gated channels. *J Physiol, 507 (Pt 2)*, 353-364.

Table 1

No.	Domain	TAG mutation position	Fluorescence (F) change		Current (I) change	
			ATP-evoked F change	Voltage-evoked F change	ATP-evoked I change	Voltage-evoked I change
1	Extracellular Domain (ECD), around ATP-binding site	D209	+	-	+	+
2		A283	+	-	+	+
3		S284 (**)	-	-	-	-
4		S285	n.d.	-	+	+
5		G286	n.d.	-	+	+
6	ECD, in extracellular linker	K53	+	-	+	+
7		S54	+	-	+	+
8		Y55 (***)	n.d.	-	+	+
9		S58	+	-	+	+
10		E63	-	-	+	+
11		S65 (**)	-	-	-	-
12		I67	-	-	+	+
13		E91	n.d.	-	+	+
14		T105	n.d.	-	+	+
15		E167	n.d.	-	+	+
16		R304	n.d.	-	+	+
17		A309	n.d.	-	+	+
18		R313	-	-	+	+
19		I314	n.d.	-	+	+
20		D315	+	-	+	+
21		V316 (**)	-	-	-	-
22		I317	-	-	+	+
23		V318 (**)	-	-	-	-
24		H319	-	-	+	+
25		A322	n.d.	-	+	+
26		K324	-	-	+	+
27		F325	+	-	+	+
28	Transmembrane 2	S326	+	-	+	+
29		L327	-	-	+	+
30		I328	-	-	+	-
31		P329	-	-	+	+
32		T330	-	-	+	-
33		I331	+	-	+	+
34		I332	+	-	+	+
35		N333	-	-	+	+
36		L334	-	-	+	+
37		A335	+	-	+	+
38		T336 (**)	-	-	-	-
39		A337	+	+	+	+
40		L338	-	-	+	+
41		T339	-	-	+	-
42		S340 (***)	n.d.	n.d.	n.d.	n.d.
43		I341	+	+	+	+
44		G342 (***)	n.d.	n.d.	n.d.	n.d.
45		V343	+	-	+	+
46		G344	-	-	+* (1mM)	+* (1mM)
47		S345	-	-	+	+

No.	Domain	TAG mutation position	Fluorescence (F) change		Current (I) change	
			ATP-evoked F change	Voltage-evoked F change	ATP-evoked I change	Voltage-evoked I change
48	Transmembrane 2	F346	+	-	+	+
49		L347	-	-	+	+
50		C348 (**)	-	-	-	-
51		D349 (**)	-	-	-	-
52	Transmembrane 1	R34	n.d.	-	+	+
53		M35	+	-	+	+
54		V36	+	-	+	+
55		Q37	+	-	+	+
56		L38	n.d.	-	+	+
57		L39	n.d.	-	+	+
58		I40	n.d.	-	+	+
59		L41	n.d.	-	+	+
60		L42	n.d.	-	+	+
61		Y43	+	-	+	-
62		F44	-	-	-	-
63		V45	+	-	+	+
64		W46	+	-	+	+
65		Y47	+	-	+	-
66		V48	-	-	-	-
67		F49	+	-	+	+
68		I50	+	-	+	+
69		V51	+	-	+	+
70		Q52	-	-	+	+
71	Intracellular C terminal	W350 (**)	-	-	-	-
72		I351	-	-	+ (3mM)	+ (3mM)
73		F355	-	-	+	+
74		M356	-	n.d.	+ (****)	n.d.
75		N357 (**)	-	-	-	-
76		K358	-	n.d.	+ (****)	n.d.
77		N359	-	-	+	+
78		L361	-	-	+	+
79		Y362	-	n.d.	+ (****)	n.d.
80		S363	-	n.d.	+ (****)	n.d.
81		H364	-	-	+	+
82		F367	n.d.	n.d.	n.d.	n.d.
83		D368 (**)	-	-	-	-
84		V370	-	n.d.	+ (****)	n.d.
85		R371	+	-	+	+
86		T372	-	-	+	+
87		P373	+	-	+	+
88		K374	+	-	+	+
89	Intracellular N terminal	Y16 (**)	-	-	-	-
90		E17 (**)	-	-	-	-
91		T18 (**)	-	-	-	-
92		P19 (**)	-	-	-	-
93		K20 (**)	-	-	-	-
94		V24	-	n.d.	+ (****)	n.d.
95		N26	-	n.d.	+ (****)	+
96		V32	-	-	+	+

Table 1 List of introduced TAG mutations in P2X2 receptor for VCF analyses using Anap

Mutations were introduced one at a time in 96 positions within extracellular domain (ECD) near ATP-binding site and extracellular linker, transmembrane domains (TMs), intracellular N-terminal, and intracellular C-terminal. (+) indicates there was either ATP-evoked fluorescence (F) signal change, voltage-evoked F change, ATP-evoked current (I) change, or voltage-evoked I change. (-) indicates negative result. (**) indicates non-functional Anap mutant channel. (***) indicates mutants which have a very low expression level so that the VCF analyses could not be performed. (****) indicates the speed of current decay, where the mutant has fast desensitization phenotype. (n.d. = not determined)

Fig. 1

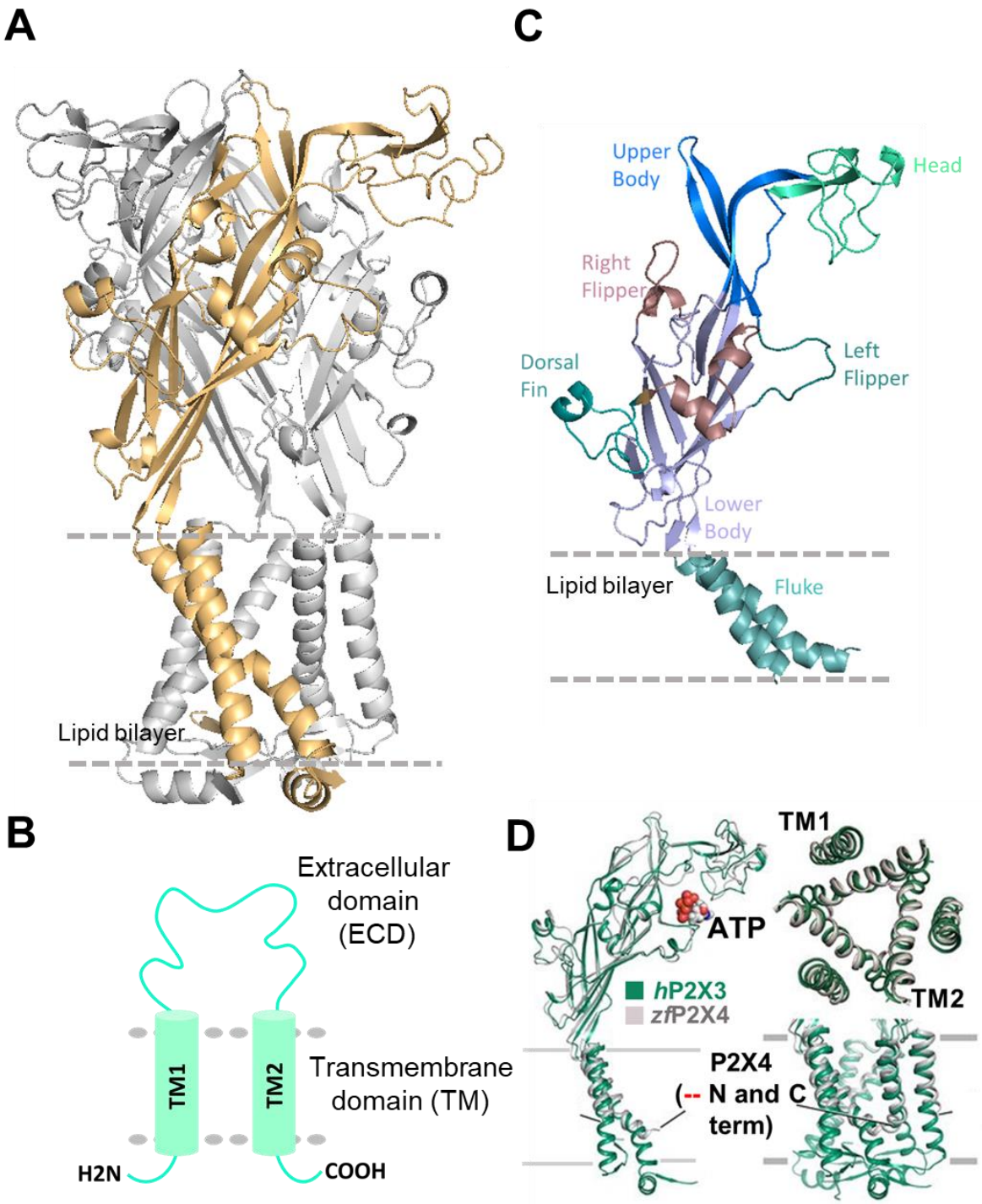
A
Lipid bilayer
C
Upper Body
Head
Right Flipper
Dorsal Fin
Left Flipper
Lower Body
Lipid bilayer
Fluke
B
Extracellular domain (ECD)
TM1
TM2
Transmembrane domain (TM)
H2N
COOH
D
TM1
ATP
hP2X3
zfP2X4
TM2
P2X4
(-- N and C term)

Fig. 1 Molecular architecture of P2X2 receptor

(A) Open state trimeric *r*P2X2 structure based on homology modeling from the open state *h*P2X3 crystal structure data (PDB ID: 5SVK; Mansoor et al., 2016). One subunit is represented in distinct color for clarity (gold). **(B)** Topology of P2X structure with two transmembrane (TM) domains, a large extracellular ligand binding loop, and intracellular N- and C- termini **(C)** One subunit of P2X receptor resembles the body of a dolphin consists of head, upper body, right flipper, dorsal fin, left flipper, and lower body region which forms large extracellular domain. Meanwhile fluke region depicts the two transmembrane domains (Kawate et al., 2009) (**D**) Superimposed crystal structures in the open state of *zf*P2X4 (grey) whose N- and C- termini were truncated for crystallization purpose (Hattori & Gouaux, 2012) and *h*P2X3 (green) with more complete TM domains and with intercellular regions (Mansoor et al., 2016).

Fig. 2

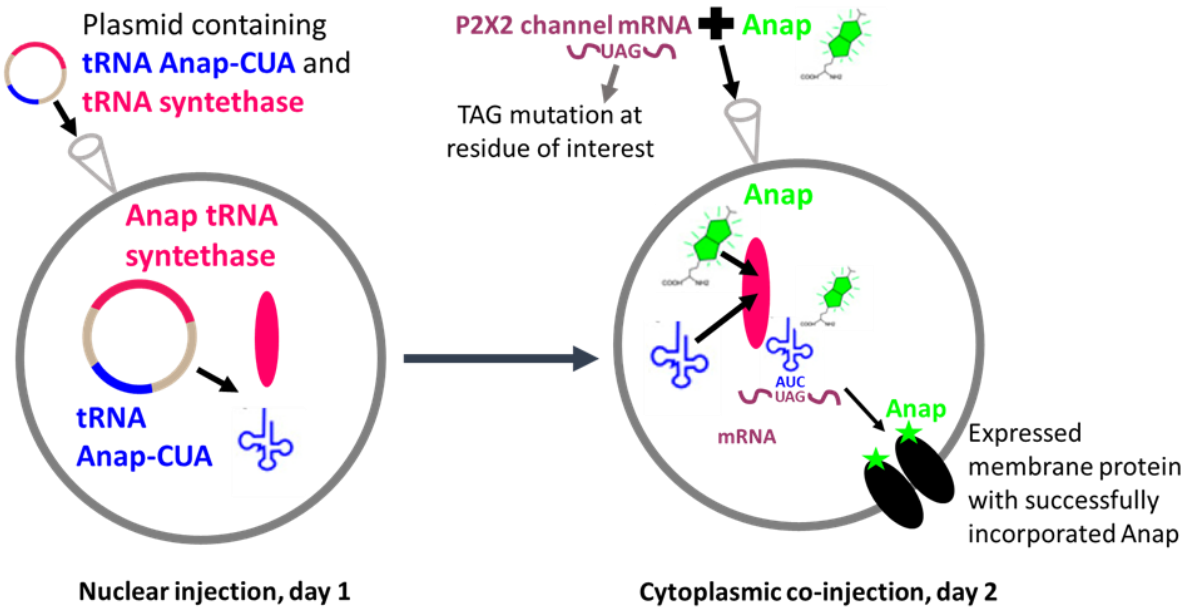
Plasmid containing
tRNA Anap-CUA and
tRNA syntethase
Anap tRNA
syntethase
tRNA
Anap-CUA
Nuclear injection, day 1
P2X2 channel mRNA
UAG
Anap
TAG mutation at
residue of interest
Anap
AUC
UAG
mRNA
Anap
Expressed
membrane protein
with successfully
incorporated Anap
Cytoplasmic co-injection, day 2

Fig. 2 *In vivo* nonsense Anap incorporation into protein in *Xenopus* expression system

Scheme depicted the principle of the direct incorporation of fUAA (Anap) into the ion channel protein. The plasmid containing tRNA Anap-CUA and tRNA synthase is injected into the nucleus of *Xenopus laevis* oocyte which is located on the animal pole. Oocytes are incubated for 1 day to enable the expression of the enzyme and tRNA. On the following day, channel cRNA with TAG mutation is co-injected with Anap into the cytoplasmic region of the oocytes. 1-3 days were needed for the incubation so that the expressed channel protein could successfully incorporate Anap for VCF recording.

Fig. 3

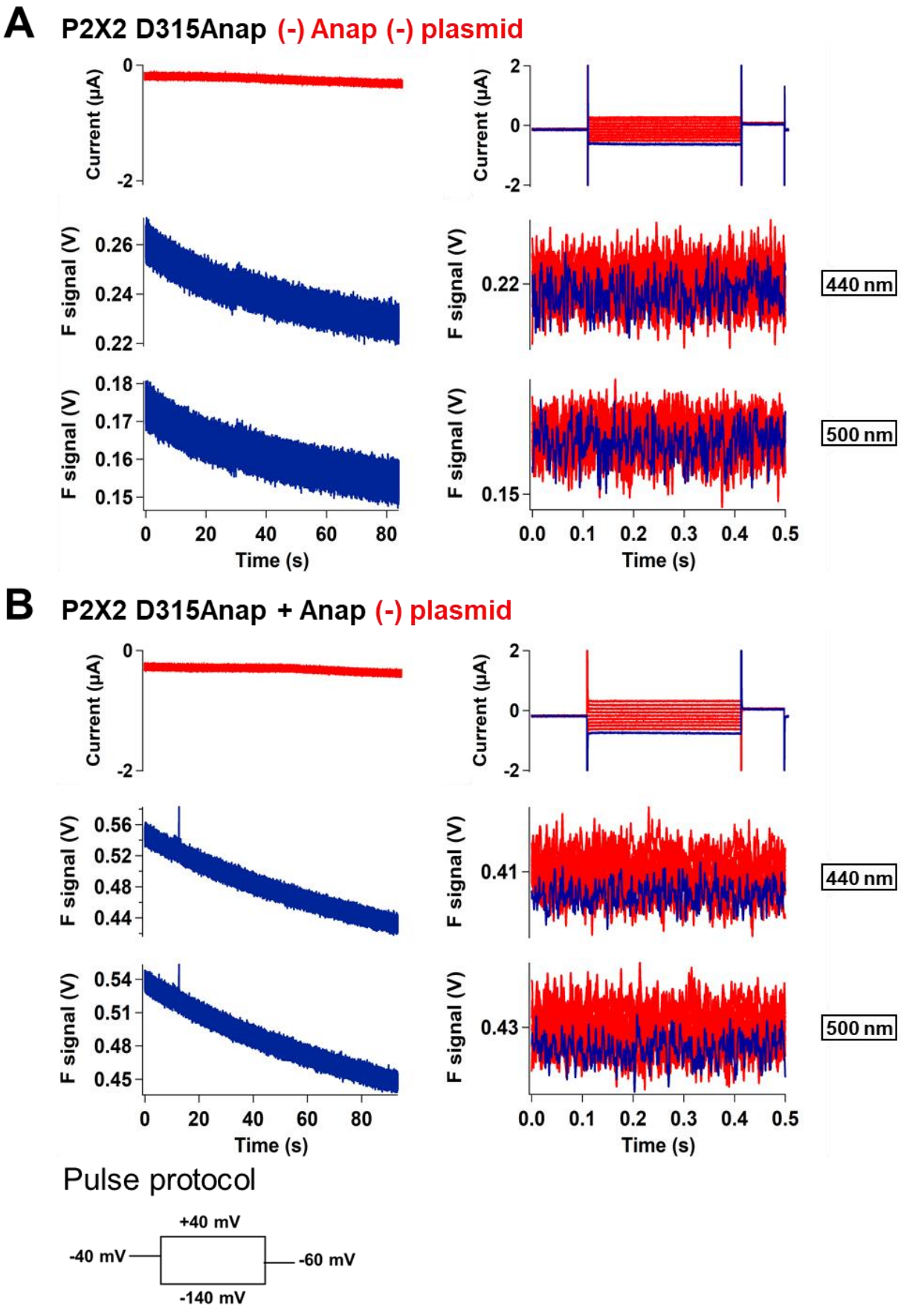
A
P2X2 D315Anap (-) Anap (-) plasmid
Current (μA)
F signal (V)
440 nm
500 nm
Time (s)
B
P2X2 D315Anap + Anap (-) plasmid
Current (μA)
F signal (V)
440 nm
500 nm
Time (s)
Pulse protocol
+40 mV
-40 mV
-60 mV
-140 mV

Fig. 3 Negative control of VCF experiments using Anap

(A, B) Representative current traces and fluorescence signals of negative control experiments for VCF-fUAA recording for each group. **(A)** Negative control group where P2X2 D315Anap was injected without both plasmid and Anap. **(B)** Negative control group where P2X2 D315Anap was injected with Anap but without plasmid. **(A, B)** There was no current expressed and no fluorescence signal in all negative experiments verifying that only channels incorporated with Anap which required p-Anap plasmid were expressed in the membrane.

Fig. 4

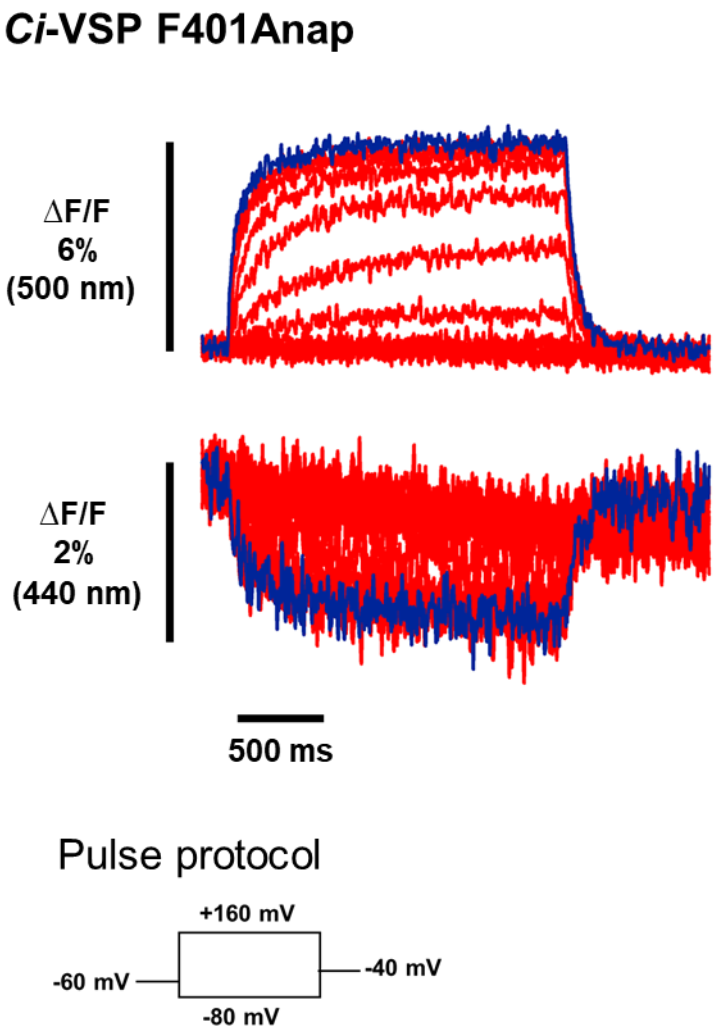
Ci-VSP F401Anap
ΔF/F
6%
(500 nm)
ΔF/F
2%
(440 nm)
500 ms
Pulse protocol
+160 mV
-60 mV
-40 mV
-80 mV

Fig. 4 Positive control of VCF experiments using Anap

Representative fluorescence signal of positive control experiments for VCF-fUAA recording using *Ciona intestinalis* voltage sensing phosphatase (*Ci*-VSP) at 500 nm and 440 nm, respectively. (*Ci*-VSP ΔF/F=5.3±0.7% at 500 nm, ΔF/F=1.5±0.2% at 440 nm, n=9). Cells were held at -60 mV and voltage step pulses were applied from -80 mV to +160 mV. Depolarization-induced fluorescence changes were detected in most of the recorded cells, indicating that the reproducibility of fluorescence change is high in the case of *Ci*-VSP. Anap methodology was confirmed to work in the *Xenopus* oocytes expression system as well as the VCF setup used in this study.

Fig. 5

A

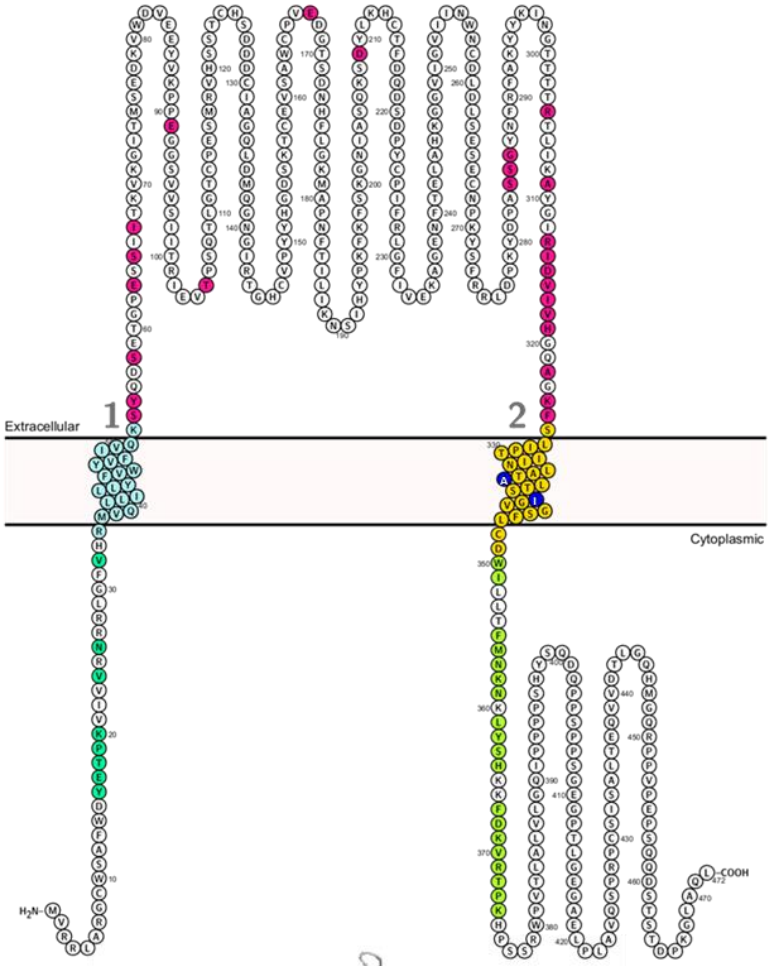
Extracellular
1
2
Cytoplasmic
H_2N-
COOH

B

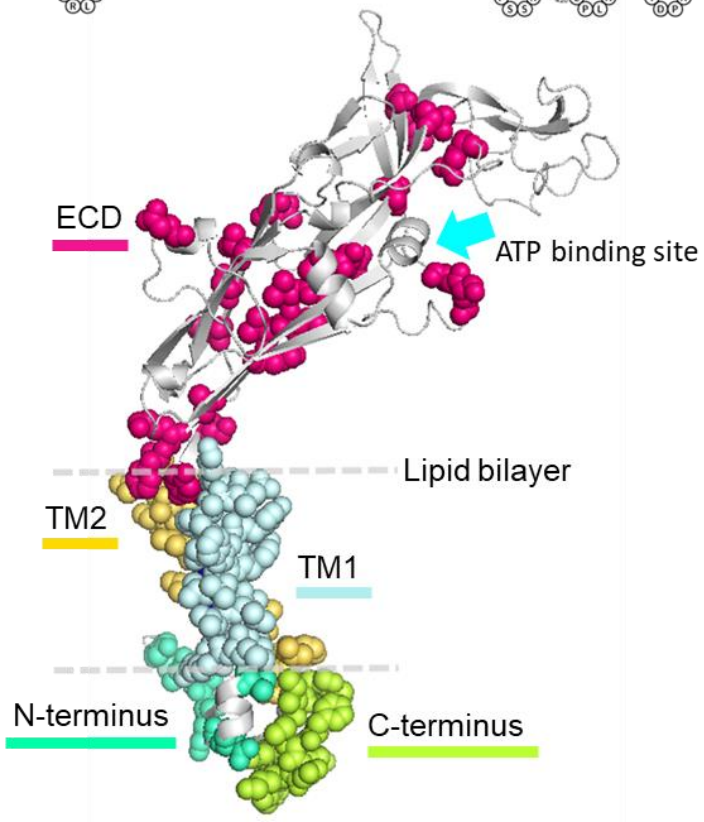
ECD
ATP binding site
Lipid bilayer
TM2
TM1
N-terminus
C-terminus

Fig. 5 Anap mutant scanning region in P2X2 receptor

(A, B) Protein visualization for Anap scanning region by individual amino acid residue representation **(A)** and within the protein structure **(B)**, respectively. Anap mutant scanning was done by introducing TAG mutation one at a time in all regions of P2X2 receptor (in total of 96 positions) which include N-terminus (8 positions), TM2 (24 positions), Extracellular domain (ECD, where the ATP binding site is located at, 25 positions), TM1 (20 positions), and C-terminus (19 positions). Voltage-dependent fluorescence changes of Anap were observed only at Ala337 and Ile341 in TM2 domain (colored by dark blue).

Fig. 6

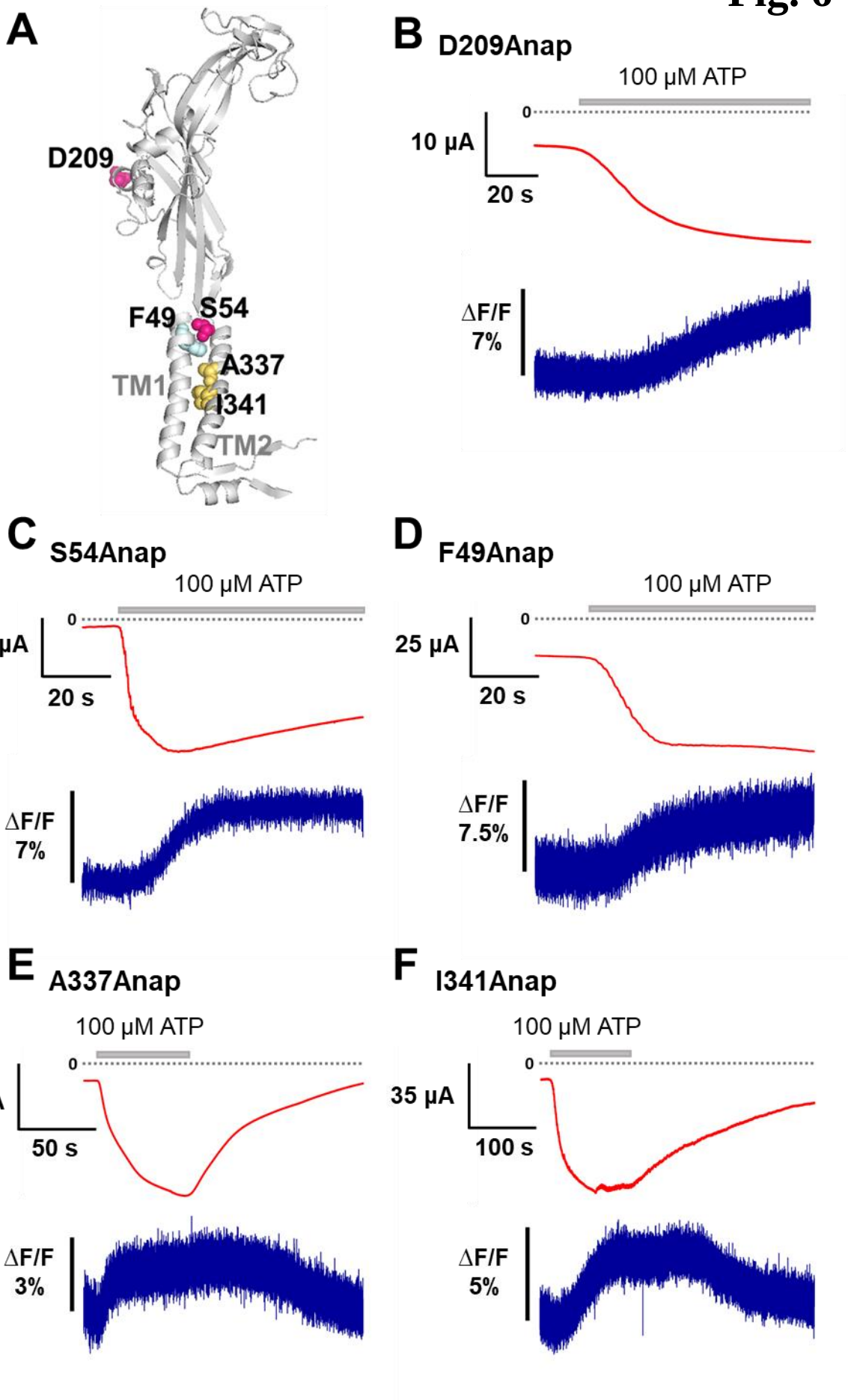
A
D209
F49
S54
A337
I341
TM1
TM2
B D209Anap
100 μM ATP
0
10 μA
20 s
ΔF/F
7%
C S54Anap
100 μM ATP
0
20 μA
20 s
ΔF/F
7%
D F49Anap
100 μM ATP
0
25 μA
20 s
ΔF/F
7.5%
E A337Anap
100 μM ATP
0
30 μA
50 s
ΔF/F
3%
F I341Anap
100 μM ATP
0
35 μA
100 s
ΔF/F
5%

Fig. 6 ATP-evoked Anap fluorescence signal changes at various positions in P2X2 receptor

(A) The representative sites of introduced TAG mutations in P2X2 receptor which showed ATP-evoked Anap fluorescence changes. **(B-F)** Representative current traces and fluorescence signal upon ATP application in the Anap mutants: D209Anap (dorsal fin, ECD), S54Anap (extracellular linker, ECD), F49Anap (TM1), A337Anap (TM2), and I341Anap (TM2), respectively. Most of the Anap fluorescence changes followed the P2X2 current during ATP application, and the changes most likely indicate the ATP-evoked structural rearrangements around the labeled residues.

Fig. 7

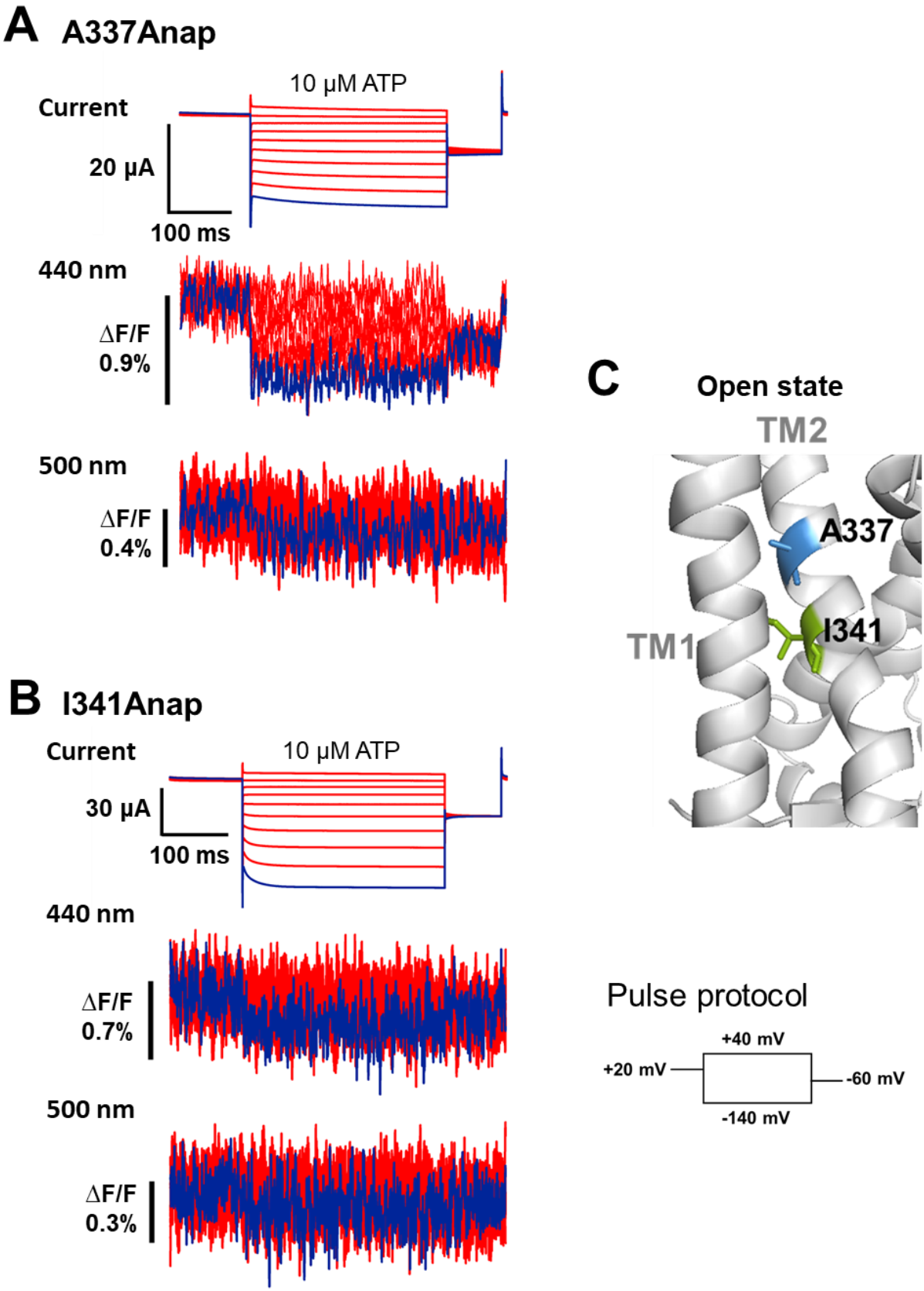
A
A337Anap
10 μM ATP
Current
20 μA
100 ms
440 nm
ΔF/F
0.9%
500 nm
ΔF/F
0.4%
B
I341Anap
Current
10 μM ATP
30 μA
100 ms
440 nm
ΔF/F
0.7%
500 nm
ΔF/F
0.3%
C
Open state
TM2
A337
I341
TM1
Pulse protocol
+40 mV
+20 mV
-60 mV
-140 mV

Fig. 7 Voltage-dependent Anap fluorescence signal changes at A337 and I341 in TM2 domain

(A, B) Representative current traces and fluorescence signal upon ATP and voltage application in Anap mutants (A337: ΔF/F=0.5±0.2% at 440 nm, n=3; I341: ΔF/F=0.3±0.2% at 440 nm, n=3; respectively) The fluorescence signal change is close to the limit of detection (ΔF/F = <1%), makes it hard to perform further analysis e.g. F-V relationship because signal to noise ratio was low. Moreover, the incidence of successful detection of fluorescence change was also low. Thus, further analysis to determine what kind of structural movements the florescence changes are associated with, had not been performed yet at this point. **(C)** The sites of the introduced TAG mutations at TM2 domain which gave voltage-evoked fluorescence changes.

Fig. 8

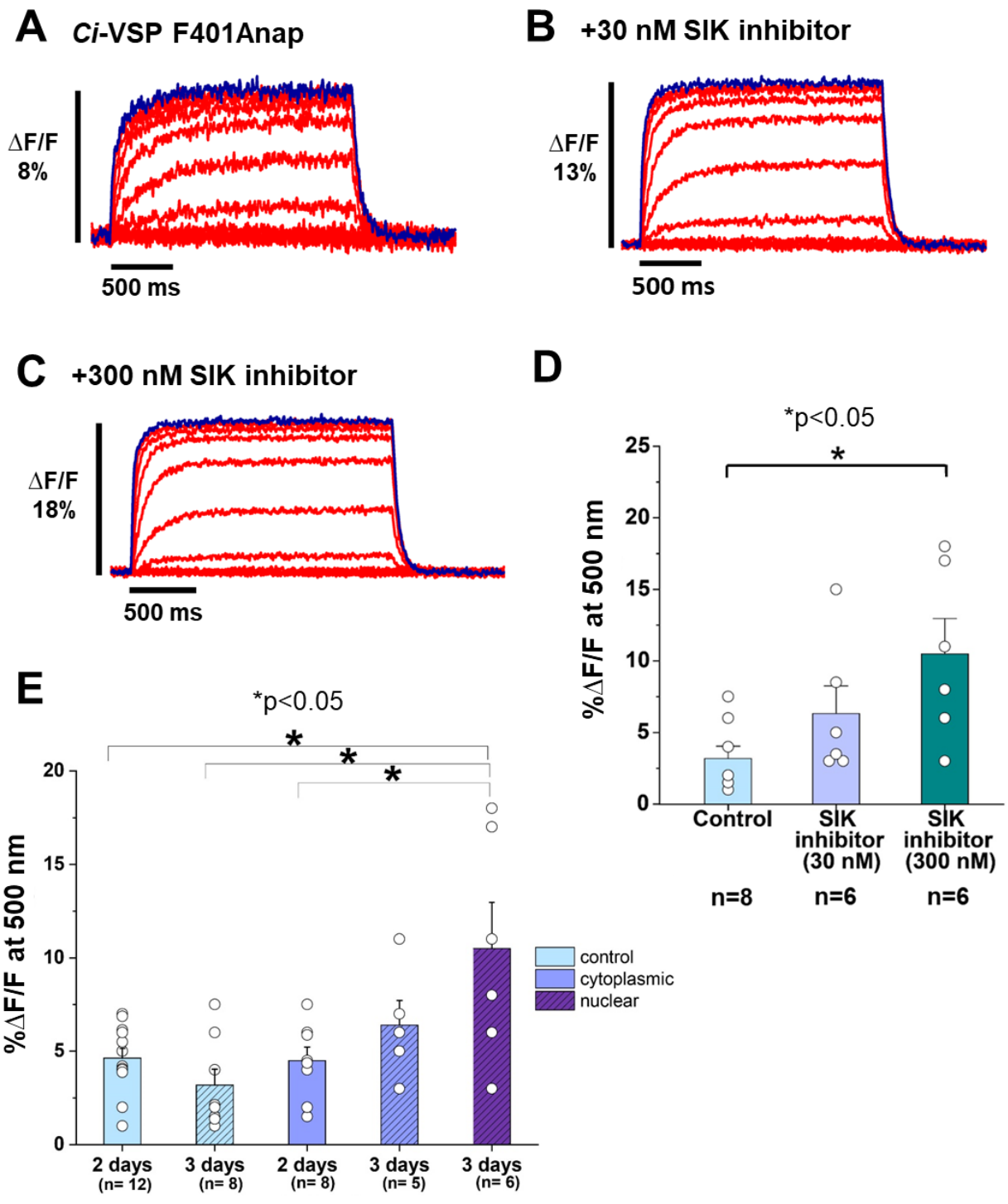
A
Ci-VSP F401Anap
ΔF/F
8%
500 ms
B
+30 nM SIK inhibitor
ΔF/F
13%
500 ms
C
+300 nM SIK inhibitor
ΔF/F
18%
500 ms
D
*p<0.05
%ΔF/F at 500 nm
Control
SIK inhibitor (30 nM)
SIK inhibitor (300 nM)
n=8
n=6
n=6
E
*p<0.05
%ΔF/F at 500 nm
2 days (n= 12)
3 days (n= 8)
2 days (n= 8)
3 days (n= 5)
3 days (n= 6)
control
cytoplasmic
nuclear

Fig. 8 SIK inhibitor application improved optical signal in *Ci*-VSP VCF-fUAA

300 nM SIK inhibitor treatment in VCF-fUAA recordings of *Ci*-VSP decreased the intrinsic background fluorescence of the oocytes, and increased the percentage of the fluorescence change. **(A)** Representative current traces and fluorescence signal of VCF recordings of *Ci*-VSP without SIK inhibitor treatment (ΔF/F= 3.2%±0.8 at 500 nm, n=8). **(B, C)** Representative current traces and fluorescence signal of the application of 30 nM and 300 nM SIK inhibitor (ΔF/F= 6.3%±1.9 at 500 nm, n=6 and ΔF/F= 10.5%±2.4 at 500 nm, n=6 respectively). **(D)** Comparison of non-treated (control) group (n=8), 30 nM (n=6), and 300 nM SIK inhibitor application (n=6); *, $p<0.05$ one-way ANOVA following Tukey post-hoc test for 300 nM compared to the control group. **(E)** Comparison of the incubation time and site of injection of SIK inhibitor treatment using 300 nM SIK inhibitor: control group with 2 days incubation (n=12), control group with 3 days incubation (n=8), SIK inhibitor treatment with cytoplasmic injection for 2 days incubation (n=8), with cytoplasmic injection for 3 days (n=5), with nuclear injection for 3 days (n=6); *, $p<0.05$ one-way ANOVA following Tukey post-hoc test. All error bars are ± s.e.m centered on the mean.

Fig. 9

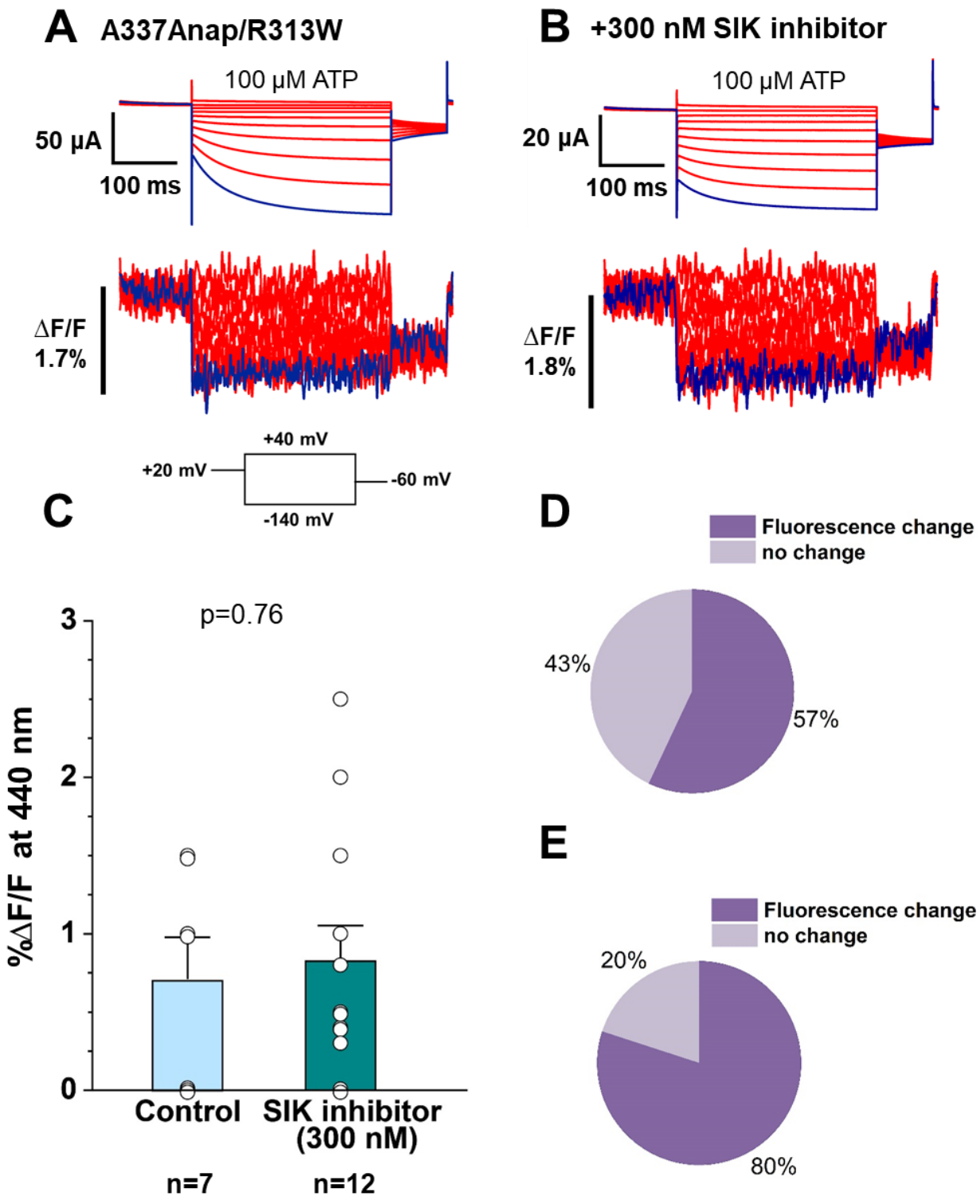
A
A337Anap/R313W
100 μM ATP
50 μA
100 ms
ΔF/F
1.7%
+40 mV
+20 mV
-60 mV
-140 mV
B
+300 nM SIK inhibitor
100 μM ATP
20 μA
100 ms
ΔF/F
1.8%
C
p=0.76
%ΔF/F at 440 nm
3
2
1
0
Control
SIK inhibitor
(300 nM)
n=7
n=12
D
Fluorescence change
no change
43%
57%
E
Fluorescence change
no change
20%
80%

Fig. 9 SIK inhibitor application improved optical signal in P2X2 VCF fUAA

300 nM SIK inhibitor treatment in VCF-fUAA recordings of P2X2 didn't give any significant difference in terms of the percentage of the fluorescence change compared to the control group. Nevertheless, SIK inhibitor treatment still improved the rate of incidence of Anap fluorescence change. **(A)** Representative current traces and fluorescence signal of VCF recordings of P2X2 receptor (A337Anap/R313W) without SIK inhibitor treatment (ΔF/F= 0.7%±0.3 at 440 nm, n=7). **(B)** Representative current traces and fluorescence signal with the application of 300 nM SIK inhibitor at P2X2 receptor A337Anap/R313W (ΔF/F= 0.8%±0.2 at 440 nm, n=12). **(C)** A comparison of non-treated (control) group (n=7) and 300 nM SIK inhibitor application (n=12) ($p = 0.76$, two sample t-test for 300 nM compared to the control group). **(D, E)** Incidence of detectable changes of Anap fluorescence for control group (57%, n=7) and 300 nM SIK inhibitor application (80%, n=12), respectively. All error bars are ± s.e.m centered on the mean.

Fig. 10

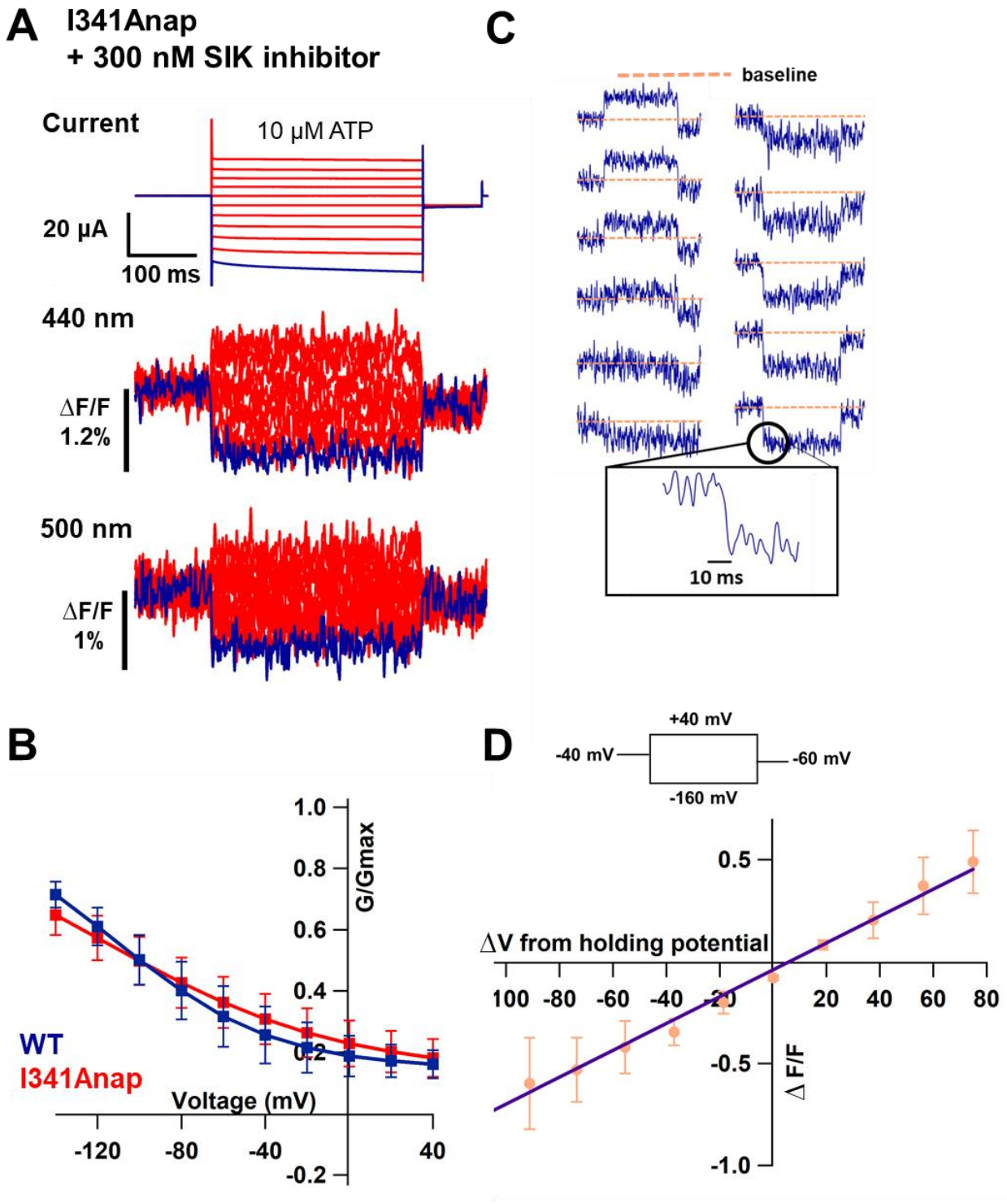
A
I341Anap
+ 300 nM SIK inhibitor
Current
10 μM ATP
20 μA
100 ms
440 nm
ΔF/F
1.2%
500 nm
ΔF/F
1%
C
baseline
10 ms
B
1.0
0.8
0.6
0.4
0.2
G/Gmax
WT
I341Anap
Voltage (mV)
-120
-80
-40
40
-0.2
D
+40 mV
-40 mV
-60 mV
-160 mV
0.5
ΔV from holding potential
100
-80
-60
-40
20
40
60
80
-0.5
-1.0
Δ F/F

Fig. 10 Anap fluorescence changes at I341 with SIK inhibitor implies electrochromic effect

Fluorescence changes of Anap at I341 were not related to hyperpolarization-induced conformational change but rather reflected a phenomenon related to electrochromic effect. **(A)** Representative current traces and fluorescence signal of VCF recordings at I341 with 300 nM SIK inhibitor treatment (ΔF/F= 0.7%±0.2 at 440 nm, n=3). **(B)** G-V relationship comparison between I341Anap (red) and wildtype (dark blue) for 10 μM ATP (n=3). Normalization was done based on the maximum conductance at the highest [ATP] (300 μM) for each construct. All error bars are ± s.e.m centered on the mean. **(C, D)** Fluorescence changes exhibited fast kinetics in ms order. Moreover, the changes showed a linear voltage-dependence, which might indicate a phenomenon related to electrochromic effect.

Fig. 11

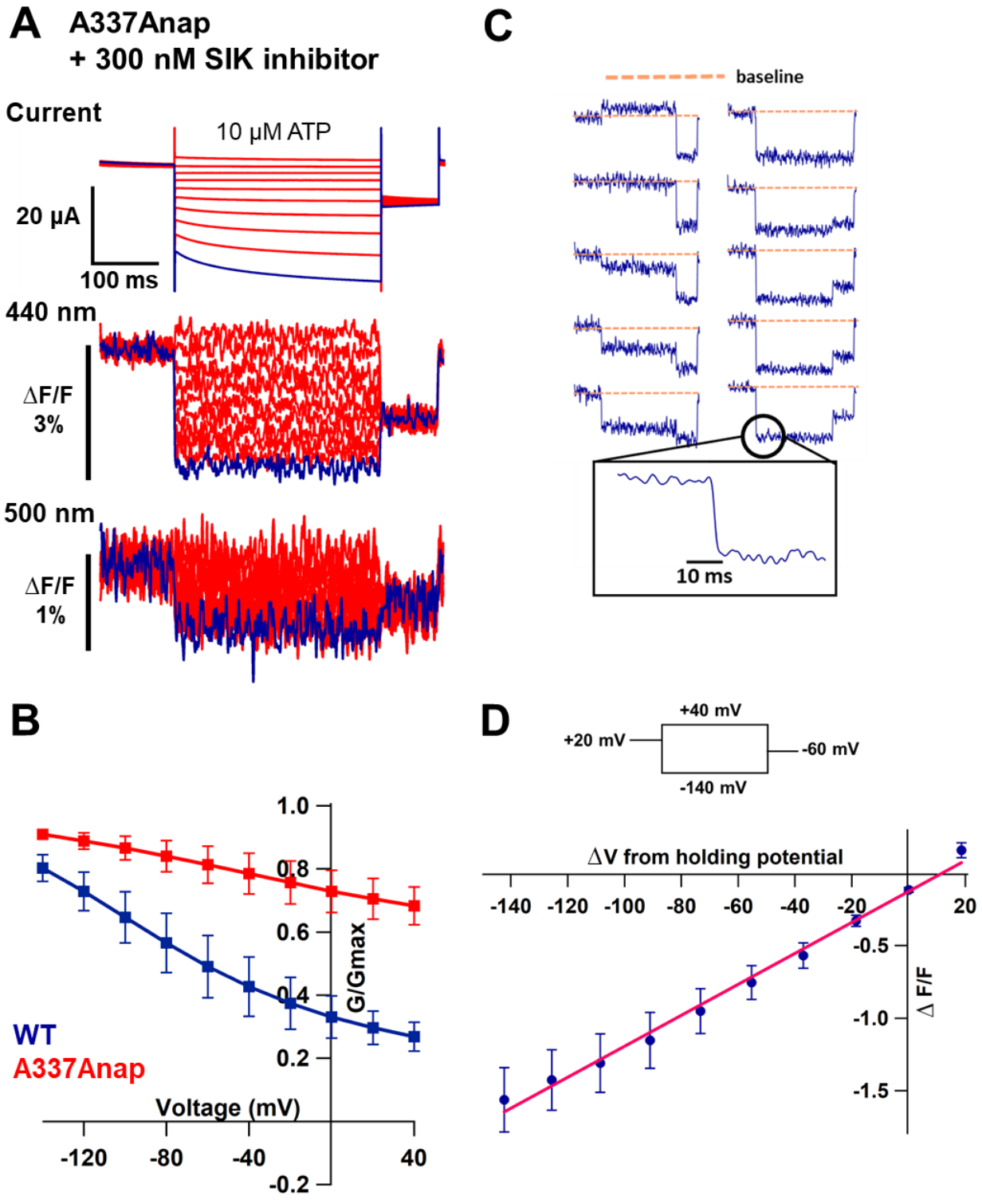
A
A337Anap
+ 300 nM SIK inhibitor
Current
10 μM ATP
20 μA
100 ms
440 nm
ΔF/F
3%
500 nm
ΔF/F
1%
C
baseline
10 ms
B
1.0
0.8
0.6
0.4
0.2
-0.2
G/Gmax
WT
A337Anap
Voltage (mV)
-120
-80
-40
40
D
+40 mV
+20 mV
-60 mV
-140 mV
ΔV from holding potential
-140
-120
-100
-80
-60
-40
-20
20
-0.5
-1.0
-1.5
Δ F/F

Fig. 11 Anap fluorescence change at A337 with SIK inhibitor also implies electrochromic effect

Fluorescence changes of Anap at A337 were also not related to hyperpolarization-induced conformational change but rather reflected a phenomenon related to electrochromic effect. **(A)** Representative current traces and fluorescence signal of VCF recordings at A337 with 300 nM SIK inhibitor treatment (ΔF/F= 1.6%±0.2 at 440 nm, n=4). **(B)** G-V relationship comparison between A337Anap (red) and wildtype (dark blue) for 10 μM ATP (n=4). Normalization was done based on the maximum conductance at the highest [ATP] (300 μM) for each construct. All error bars are ± s.e.m centered on the mean. **(C, D)** Fluorescence changes exhibited fast kinetics in ms order. Moreover, the changes showed a linear voltage-dependence, which might indicate a phenomenon related to electrochromic effect.

Fig. 12

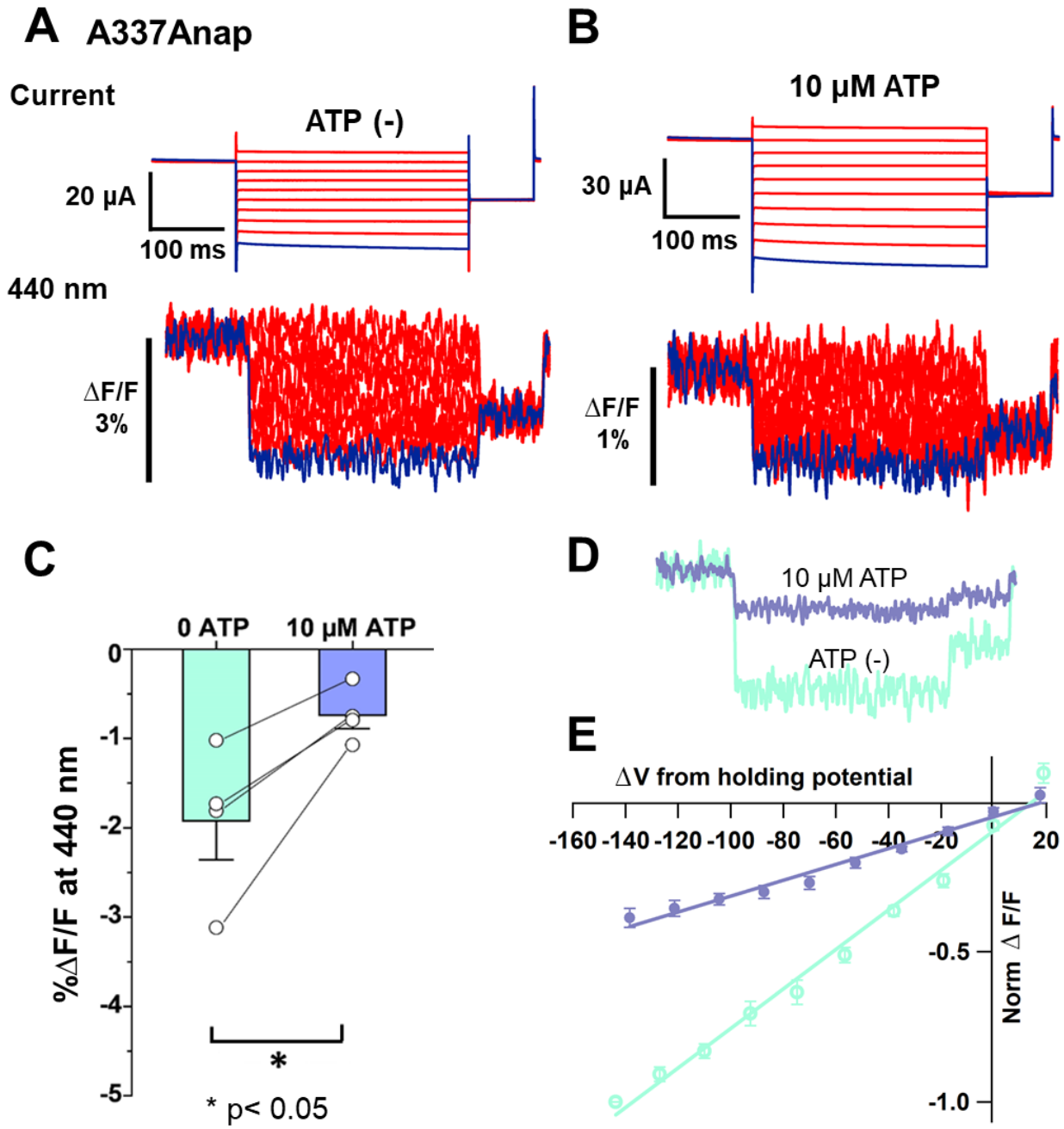
A
A337Anap
Current
ATP (-)
20 μA
100 ms
440 nm
ΔF/F
3%
B
10 μM ATP
30 μA
100 ms
ΔF/F
1%
C
0 ATP
10 μM ATP
%ΔF/F at 440 nm
0
-1
-2
-3
-4
-5
*
* p< 0.05
D
10 μM ATP
ATP (-)
E
ΔV from holding potential
-160 -140 -120 -100 -80 -60 -40 -20 20
Norm Δ F/F
-0.5
-1.0

Fig. 12 Anap fluorescence changes at A337 was observed both in the absence and presence of 10 µM ATP

Anap fluorescence changes at A337 were also observed even in the absence of ATP. This implied that the focused electric field is already present in the absence of ATP. The observed focused electric field was stronger in the absence of ATP than in the presence of ATP **(A, B)** Representative current traces and fluorescence signal of VCF recordings at A337 in the absence of ATP (ΔF/F= 1.9%±0.4 at 440 nm, n=4) and 10 µM ATP (ΔF/F= 0.7%±0.1 at 440 nm, n=4) **(C)** Comparison of the fluorescence changes in the absence and in the presence of 10 µM ATP (* $p<0.05$, paired t-test, n=4) **(D)** Superimposed fluorescence traces at -140 mV of 0 ATP (light green) and 10 µM ATP application (light purple) **(E)** F-V relationship comparison for 0 ATP (light green) and 10 µM ATP (light purple) with a holding potential +20 mV (n=4). Normalization was done based on the highest ΔF/F in each cell (in the absence of ATP). All error bars are ± s.e.m centered on the mean.

Fig. 13

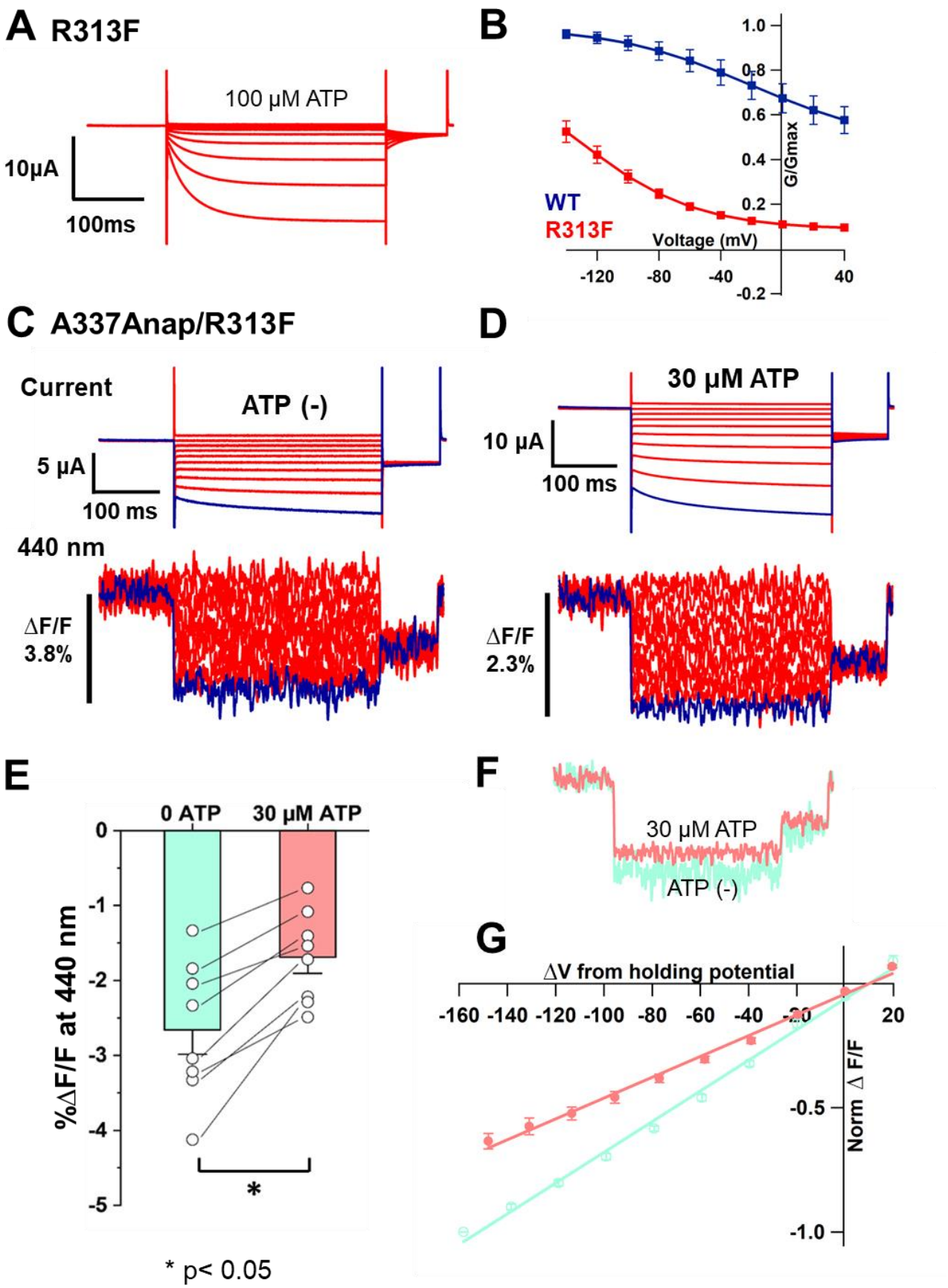
A R313F
100 μM ATP
10μA
100ms
B
1.0
0.8
0.6
0.4
0.2
-0.2
G/Gmax
WT
R313F
Voltage (mV)
-120
-80
-40
40
C A337Anap/R313F
Current
ATP (-)
5 μA
100 ms
440 nm
ΔF/F
3.8%
D
30 μM ATP
10 μA
100 ms
ΔF/F
2.3%
E
0 ATP
30 μM ATP
0
-1
-2
-3
-4
-5
%ΔF/F at 440 nm
*
* p< 0.05
F
30 μM ATP
ATP (-)
G
ΔV from holding potential
-160 -140 -120 -100 -80 -60 -40 -20 20
-0.5
-1.0
Norm Δ F/F

Fig. 13 Fluorescence changes of Anap at A337 with additional R313F mutation upon voltage change was also observed in both 0 ATP condition and in the presence of 30 µM ATP

Additional R313F mutation was introduced on top of A337Anap to lower the basal activity of A337Anap and stabilize the closed state. A337Anap/R313F mutants further confirmed that focused electric field is already present in the absence of ATP. This focused electric field was stronger in the absence of ATP. **(A)** Representative current traces of R313F upon application of 100 µM ATP **(B)** Comparison of G-V relationship between R313F (red) and wildtype (dark blue) for 100 µM ATP (n=3). Normalization was done based on the maximum conductance at the highest [ATP] (300 µM) for each construct. **(C, D)** Representative current traces and fluorescence signal of VCF recordings of A337/R313F in the absence of ATP (ΔF/F= 2.6%±0.3 at 440 nm, n=8) and in the presence of 30 µM ATP (ΔF/F= 1.7%±0.2 at 440 nm, n=8) **(E)** Comparison of the fluorescence changes in the absence and in the presence of 30 µM ATP (* $p<0.05$, paired t-test, n=8) **(F)** Superimposed fluorescence traces at -140 mV of 0 ATP (light green) and 30 µM ATP application (pink) **(G)** F-V relationship comparison for 0 ATP (light green) and 30 µM ATP (pink) with a holding potential +20 mV (n=8). Normalization was done based on the highest ΔF/F in each cell (in the absence of ATP). All error bars are ± s.e.m centered on the mean.

Fig. 14

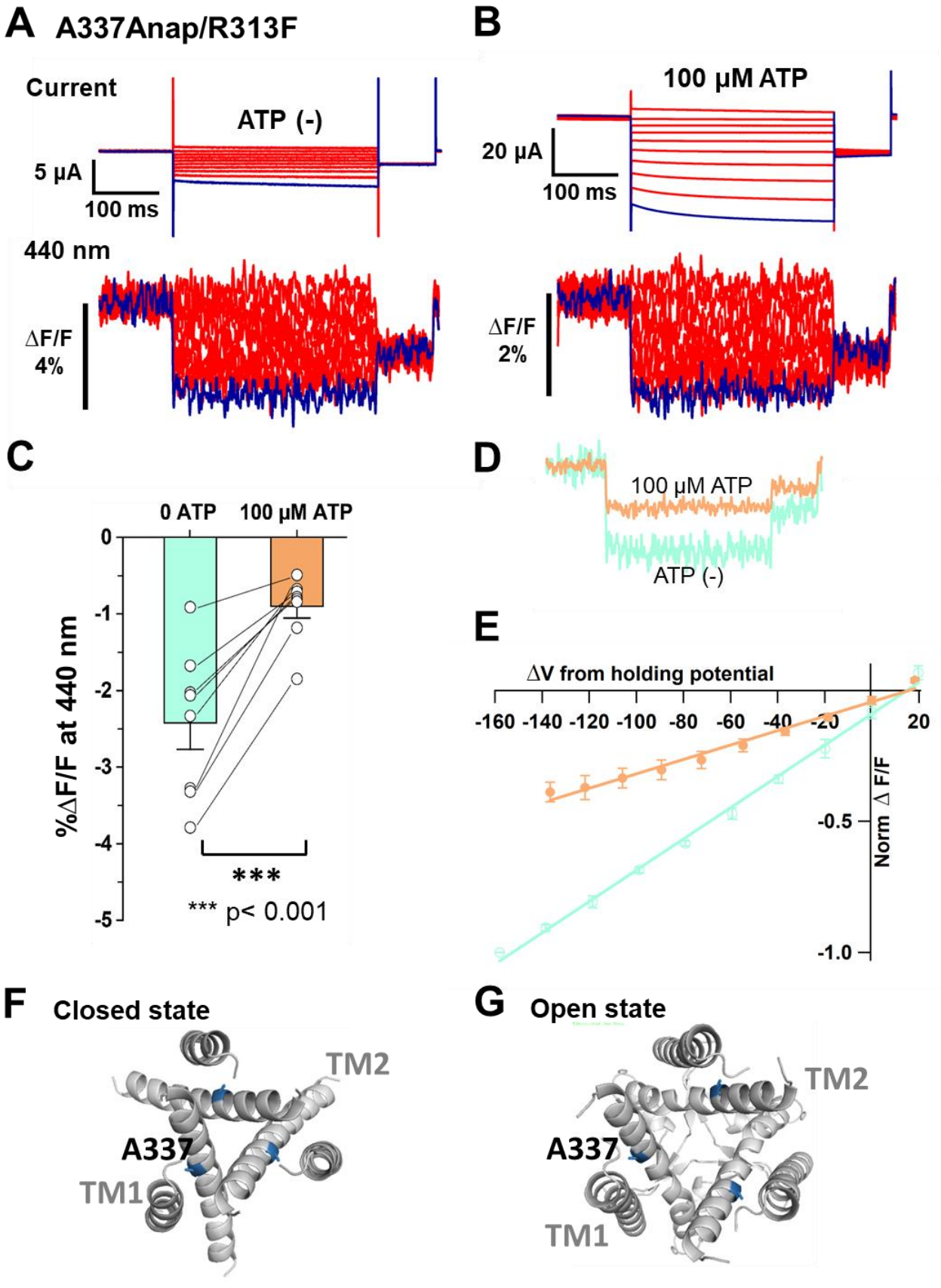
A
A337Anap/R313F
Current
ATP (-)
5 μA
100 ms
440 nm
ΔF/F
4%
B
100 μM ATP
20 μA
100 ms
ΔF/F
2%
C
0 ATP
100 μM ATP
%ΔF/F at 440 nm
0
-1
-2
-3
-4
-5
***
*** p< 0.001
D
100 μM ATP
ATP (-)
E
ΔV from holding potential
-160 -140 -120 -100 -80 -60 -40 -20 20
Norm Δ F/F
-0.5
-1.0
F
Closed state
TM2
A337
TM1
G
Open state
TM2
A337
TM1

Fig. 14 Fluorescence change of A337Anap/R313F upon voltage change was [ATP]-dependent and smaller in the presence of 100 µM ATP

Higher ATP application (100 µM) in A337Anap/R313F mutants further confirmed that the focused electric field at A337 is [ATP]-dependent and stronger in the absence of ATP. **(A, B)** Representative current traces and fluorescence signal of VCF recordings of A337/R313F in the absence of ATP (ΔF/F= 2.4%±0.3 at 440 nm, n=8) and in the presence of 100 µM ATP (ΔF/F= 0.9%±0.1 at 440 nm, n=8). **(C)** Comparison of the fluorescence changes in the absence and in the presence of 100 µM ATP (*** $p<0.001$, paired t-test, n=8). **(D)** Superimposed fluorescence traces at -140 mV of 0 ATP (light green) and 100 µM ATP application (orange). **(E)** F-V relationship comparison for 0 ATP (light green) and 100 µM ATP (orange) with a holding potential +20 mV (n=8). Normalization was done based on the highest ΔF/F in each cell (in the absence of ATP). All error bars are ± s.e.m centered on the mean. **(F, G)** Top view structure of the location of A337 of the closed (F) and open (G) state P2X2 receptor.

Fig. 15

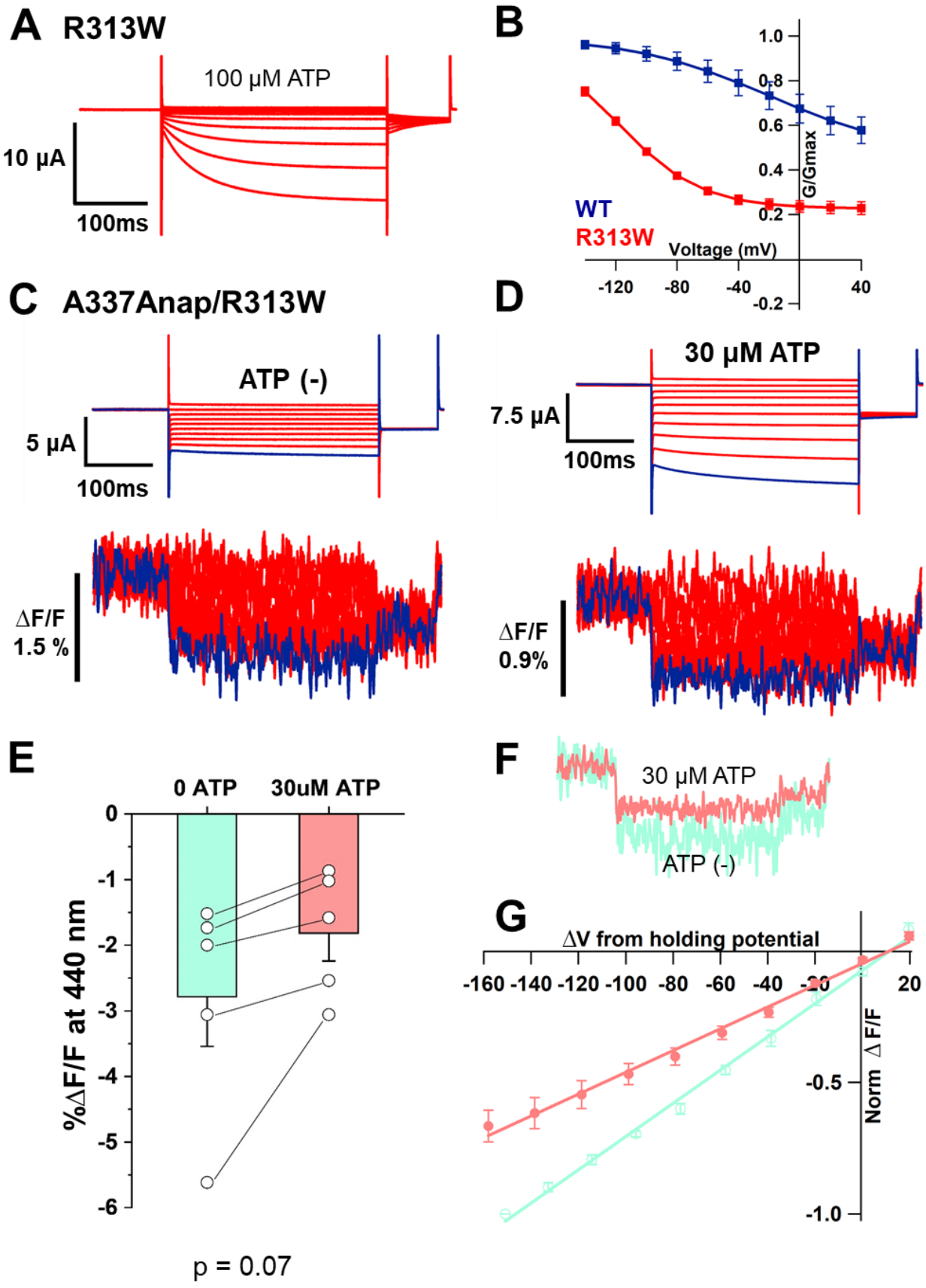
A
R313W
100 μM ATP
10 μA
100ms
B
1.0
0.8
0.6
0.4
0.2
G/Gmax
WT
R313W
Voltage (mV)
-120
-80
-40
40
-0.2
C
A337Anap/R313W
ATP (-)
5 μA
100ms
ΔF/F
1.5 %
D
30 μM ATP
7.5 μA
100ms
ΔF/F
0.9%
E
0 ATP
30uM ATP
0
-1
-2
-3
-4
-5
-6
%ΔF/F at 440 nm
p = 0.07
F
30 μM ATP
ATP (-)
G
ΔV from holding potential
-160 -140 -120 -100 -80 -60 -40 -20 20
-0.5
-1.0
Norm ΔF/F

Fig. 15 Fluorescence changes of Anap at A337 with additional R313W mutation upon voltage change was also observed in both 0 ATP condition and in the presence of 30 µM ATP

Additional R313W mutation was also introduced on top of A337Anap to lower the basal activity of A337Anap and stabilized the closed state. A337Anap/R313W mutants also further confirmed that focused electric field is already present in the absence of ATP. This focused electric field was stronger in the absence of ATP. **(A)** Representative current traces of R313W upon the application of 100 µM ATP. **(B)** G-V relationship comparison between R313W (red) and wildtype (dark blue) in 100 µM ATP (n=3). Normalization was done based on the maximum conductance at the highest [ATP] (300 µM) for each construct. **(C, D)** Representative current traces and fluorescence signal of VCF recordings of A337Anap/R313W in the absence of ATP (ΔF/F= 2.8%±0.7 at 440 nm, n=5) and 30 µM ATP (ΔF/F= 1.8%±0.4 at 440 nm, n=5). **(E)** Comparison of the fluorescence changes in the absence and in the presence of 30 µM ATP (p=0.07, paired t-test, n=5). **(F)** Superimposed fluorescence traces at -140 mV of 0 ATP (light green) and 30 µM ATP application (pink). **(G)** F-V relationship comparison for 0 ATP (light green) and 30 µM ATP (pink) with a holding potential +20 mV (n=5). Normalization was done based on the highest ΔF/F in each cell (in the absence of ATP). All error bars are ± s.e.m centered on the mean.

Fig. 16

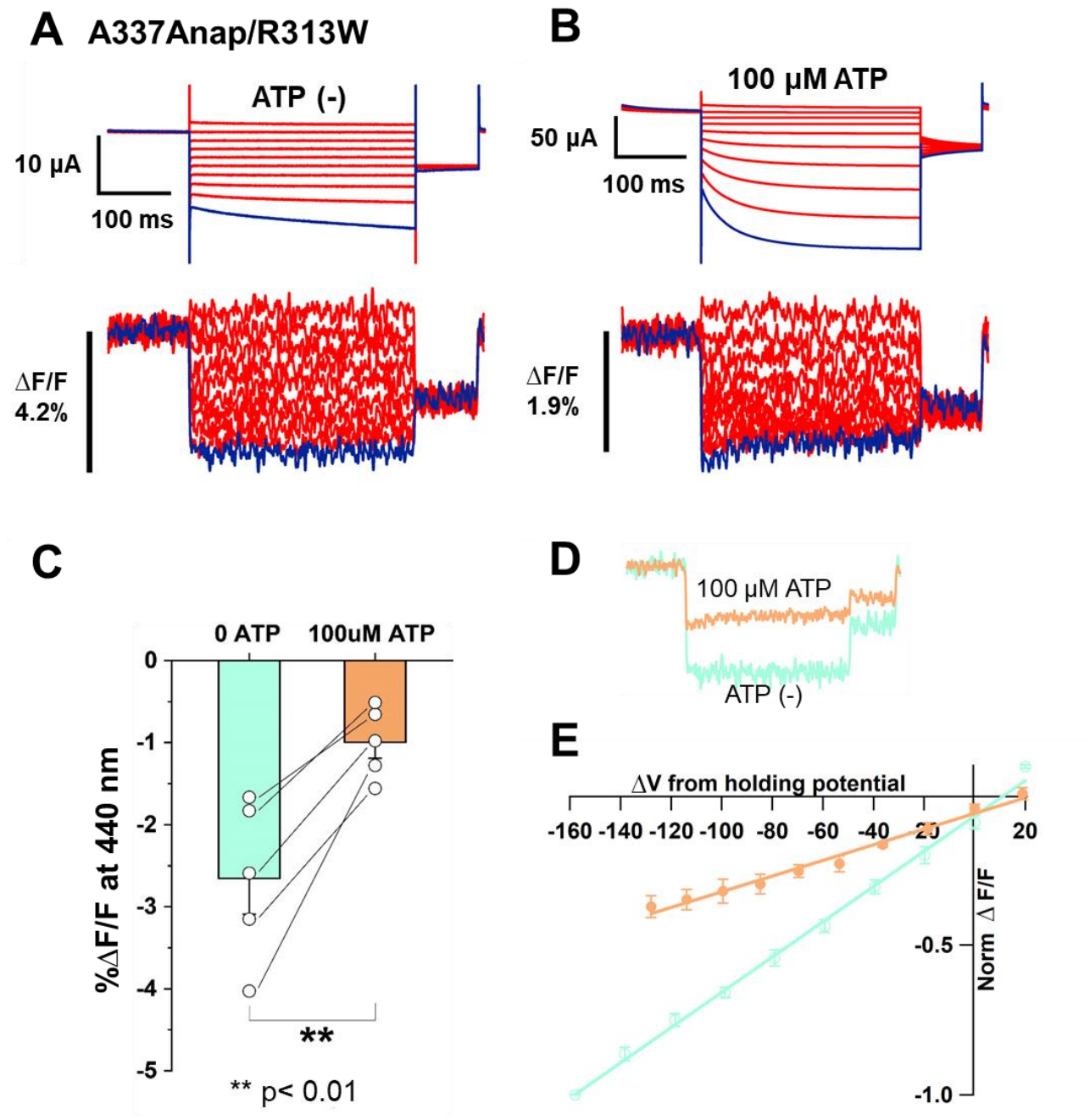
A
A337Anap/R313W
ATP (-)
10 μA
100 ms
ΔF/F
4.2%
B
100 μM ATP
50 μA
100 ms
ΔF/F
1.9%
C
0 ATP
100uM ATP
%ΔF/F at 440 nm
0
-1
-2
-3
-4
-5
**
** p< 0.01
D
100 μM ATP
ATP (-)
E
ΔV from holding potential
-160 -140 -120 -100 -80 -60 -40 -20 20
Norm Δ F/F
-0.5
-1.0

Fig. 16 Fluorescence change of A337Anap/R313W upon voltage change was [ATP]-dependent and smaller in the presence of 100 µM ATP

Higher ATP application (100 µM) in A337Anap/R313F mutants further confirmed that the focused electric field at A337 is [ATP]-dependent and stronger in the absence of ATP. **(A, B)** Representative current traces and fluorescence signal of VCF recordings of A337/R313W in the absence of ATP (ΔF/F= 2.6%±0.4 at 440 nm, n=5) and 100 µM ATP (ΔF/F= 0.9%±0.2 at 440 nm, n=5) **(C)** Comparison of the fluorescence changes in the absence and in the presence of 100 µM ATP (** $p<0.01$, paired t-test, n=5) **(D)** Superimposed fluorescence traces at -140 mV of 0 ATP (light green) and 100 µM ATP application (orange) **(E)** F-V relationship comparison for 0 ATP (light green) and 100 µM ATP (orange) with a holding potential +20 mV (n=5). Normalization was done based on the highest ΔF/F in each cell (in the absence of ATP). All error bars are ± s.e.m centered on the mean.

Fig. 17

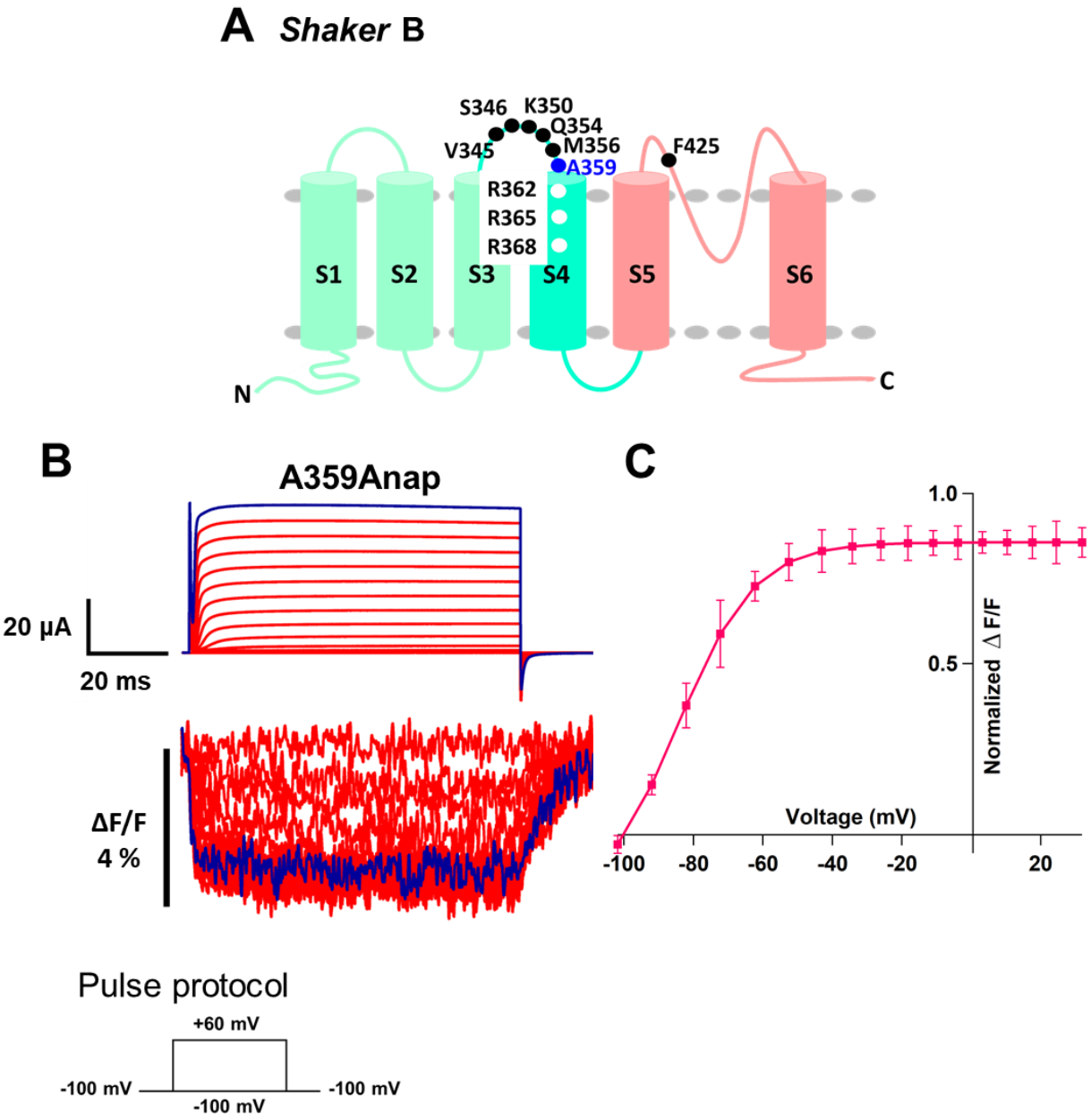
A Shaker B
S346
K350
Q354
V345
M356
F425
A359
R362
R365
R368
S1
S2
S3
S4
S5
S6
N
C
B
A359Anap
20 μA
20 ms
ΔF/F
4 %
C
1.0
0.5
Normalized ΔF/F
Voltage (mV)
-100
-80
-60
-40
-20
20
Pulse protocol
+60 mV
-100 mV
-100 mV
-100 mV

Fig. 17 Anap fluorescence changes at *Shaker* B K^+ channel

The electrochromic effect of Anap was further examined by incorporating it to various positions which have been reportedly to show a site-specific electrochromic effect in *Shaker* B K^+ channel. **(A)** Schematic drawing of Anap introduced sites in *Shaker* B K^+ channel. **(B)** Representative current traces and fluorescence signal of *Shaker* B K_v A359Anap ($\Delta F/F$= 2.4%±0.5 at 440 nm, n=4). Voltage step pulses were applied from -100 mV to +60 mV with a holding potential at -100 mV. **(C)** F-V relationship of A359Anap (n=4). All error bars are ± s.e.m centered on the mean. This approach couldn't give results which support that Anap has electrochromic properties. Based on the F-V relationship, this fluorescence changes reported depolarization-induced conformational changes where the S4 moves up to sense the change in membrane potential.

Fig. 18

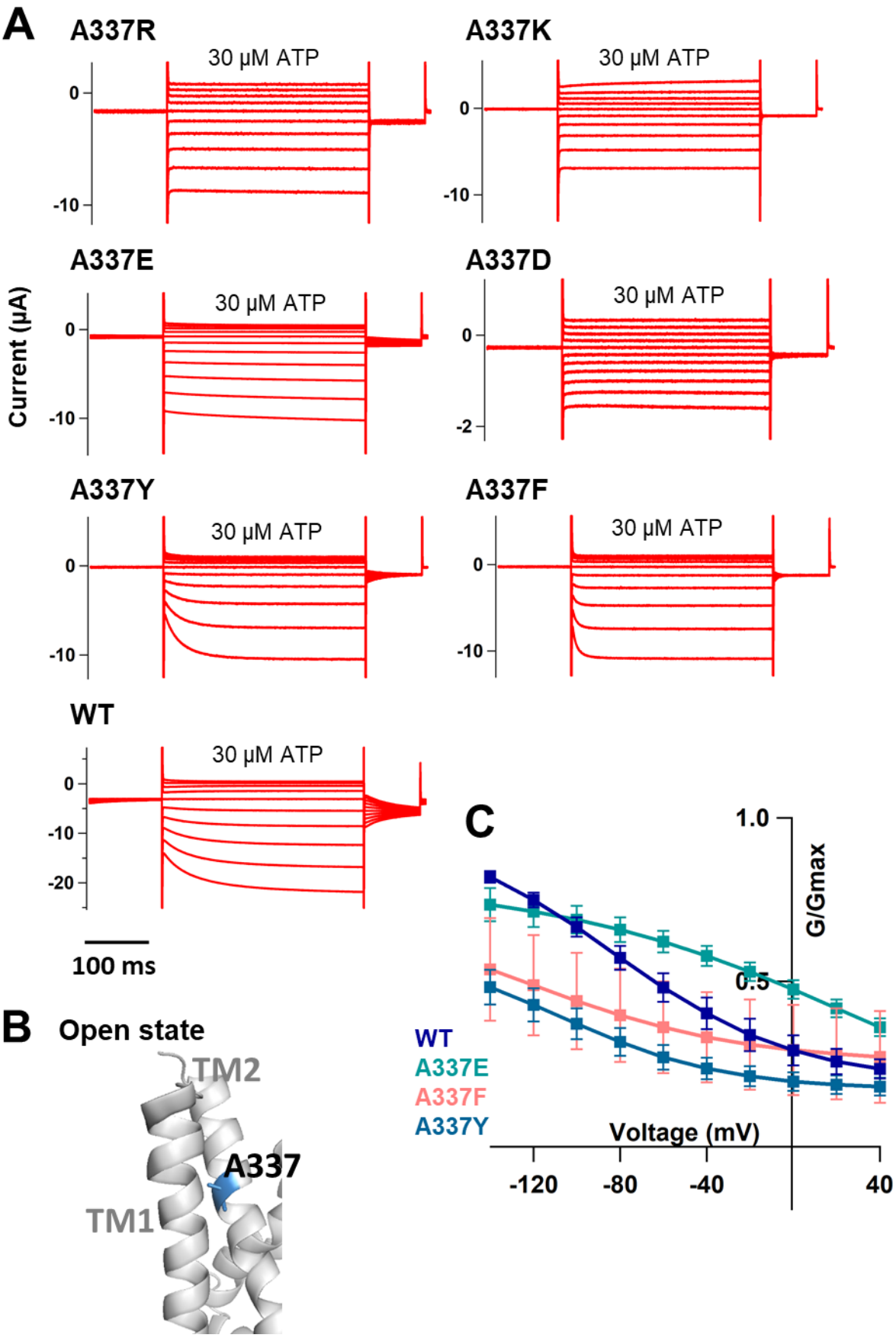
A
A337R
30 μM ATP
0
-10
A337K
30 μM ATP
0
-10
A337E
30 μM ATP
0
-10
A337D
30 μM ATP
0
-2
Current (μA)
A337Y
30 μM ATP
0
-10
A337F
30 μM ATP
0
-10
WT
30 μM ATP
0
-10
-20
100 ms
B
Open state
TM2
A337
TM1
C
1.0
G/Gmax
0.5
WT
A337E
A337F
A337Y
Voltage (mV)
-120
-80
-40
40

Fig. 18 Single amino acid mutations at the position of A337 implies that this position is critical for complex gating

The activation kinetics and gating properties of WT P2X2 were altered by the introduction of single amino acid mutation at A337. Hence, this position was shown to be critical for P2X2 receptor complex gating. **(A)** Representative current traces of single amino acid mutants at the position of A337 upon 30 μM ATP and voltage application (A337R, A337K, A337E, A337D, A337Y, A337F and WT; respectively). **(B)** Side view structure of the position of A337 in the open state. **(C)** Comparison of G-V relationships between WT, A337E, A337F, and A337Y for 30 μM ATP (n=3). Normalization was done based on the maximum conductance in the highest [ATP] (300 μM) for each construct. All error bars are ± s.e.m centered on the mean.

Fig. 19

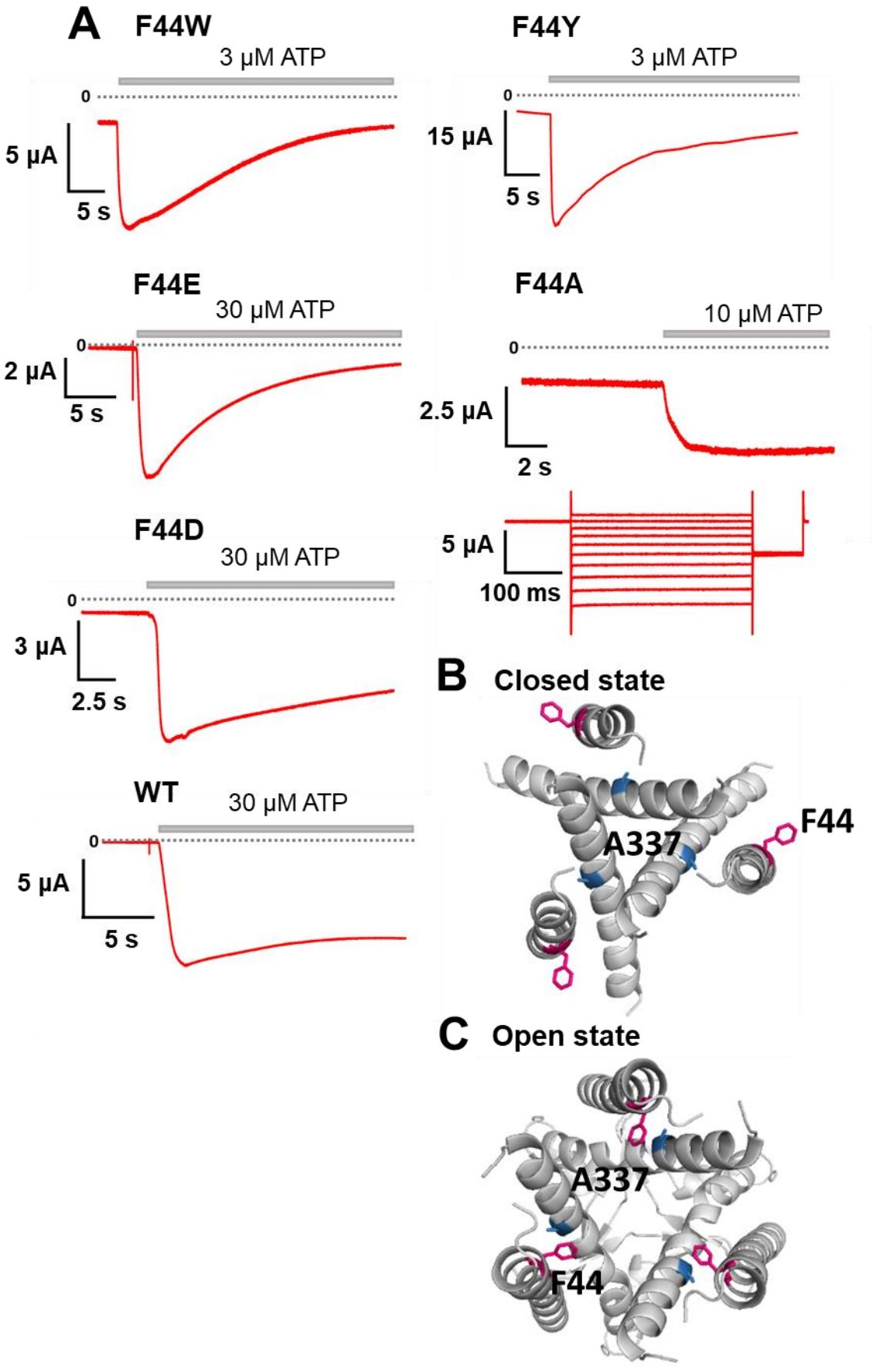
A
F44W
3 μM ATP
0
5 μA
5 s
F44Y
3 μM ATP
0
15 μA
5 s
F44E
30 μM ATP
0
2 μA
5 s
F44A
10 μM ATP
0
2.5 μA
2 s
5 μA
100 ms
F44D
30 μM ATP
0
3 μA
2.5 s
WT
30 μM ATP
0
5 μA
5 s
B
Closed state
A337
F44
C
Open state
A337
F44

Fig. 19 Single amino acid mutations of F44 implies that this position is important for the proper ATP- and voltage-dependent gating

(A) Representative current traces of single amino acid mutants at the position of A337 upon application of various ATP (F44W, F44Y, F44E, F44A, F44D and WT; respectively). Mutation to negatively charged residues (F44E, F44D) and aromatic residues (F44Y, F44W) remarkably changed the gating. All four mutants still opened upon the binding of ATP but current decay appeared to be faster than wildtype. Mutation to F44A also strikingly changed the gating. (n=3-6 for each mutant). **(B, C)** Top view structure of the position of F44 in the closed **(B)** and ATP-bound open state **(C)**, respectively.

Fig. 20

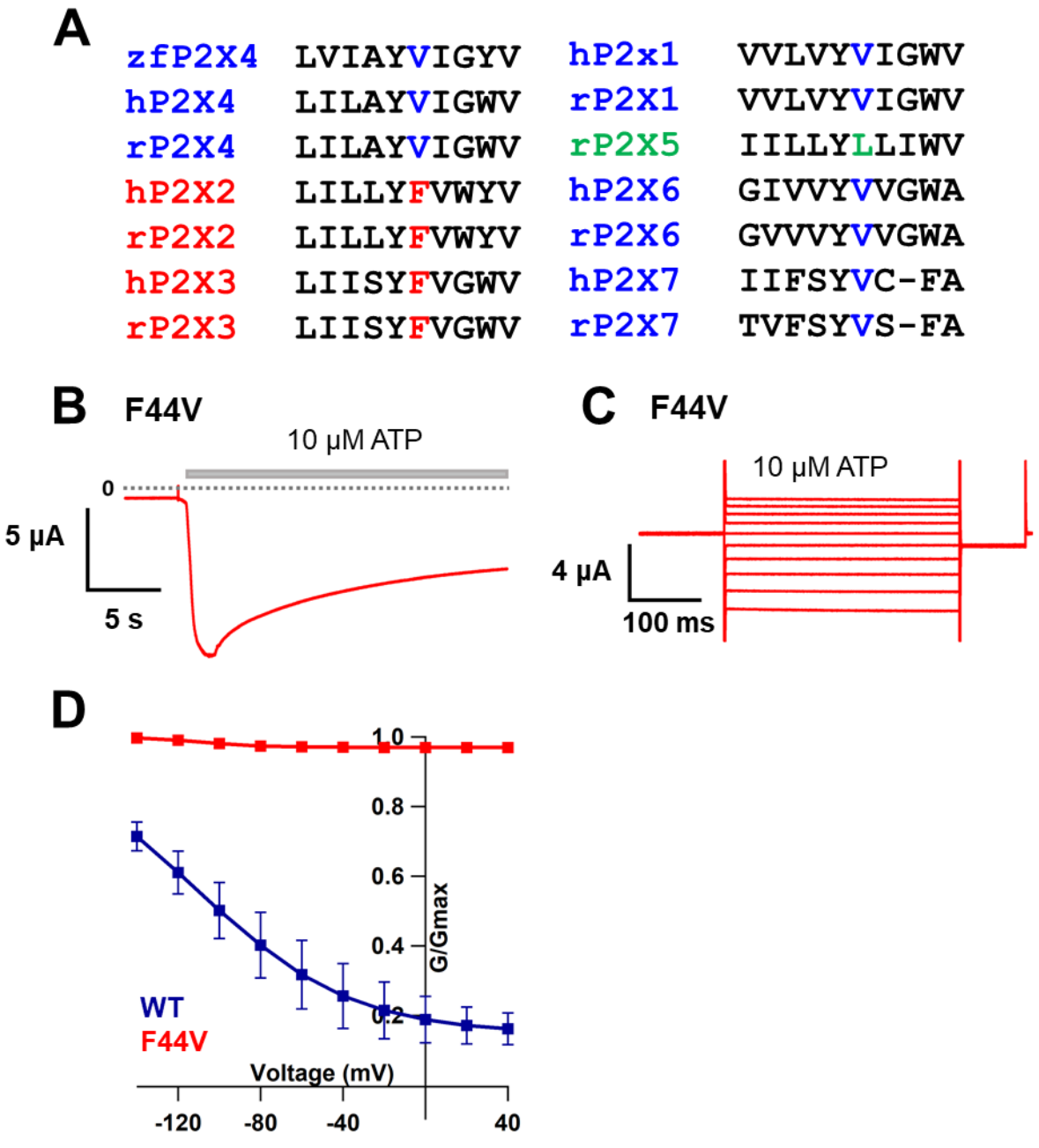
A
zfP2X4 LVIAYVIGYV
hP2X4 LILAYVIGWV
rP2X4 LILAYVIGWV
hP2X2 LILLYFVWYV
rP2X2 LILLYFVWYV
hP2X3 LIISYFVGWV
rP2X3 LIISYFVGWV
hP2x1 VVLVYVIGWV
rP2X1 VVLVYVIGWV
rP2X5 IILLYLLIWV
hP2X6 GIVVYVVGWA
rP2X6 GVVVYVVGWA
hP2X7 IIFSYVC-FA
rP2X7 TVFSYVS-FA
B F44V
10 μM ATP
0
5 μA
5 s
C F44V
10 μM ATP
4 μA
100 ms
D
1.0
0.8
0.6
0.4
0.2
G/Gmax
WT
F44V
Voltage (mV)
-120
-80
-40
40

Fig. 20 A single amino acid mutant F44V showed a faster current decay and also remarkably altered voltage-dependent gating

(A) Sequence alignment of P2X receptor subtypes along with their orthologues of a part of TM1 region adjacent to F44 in *r*P2X2 receptor. Corresponding and identical residues with F44 in *r*P2X2 are highlighted in red. Blue and green highlights indicated corresponding and different residue in other subtypes and various orthologues. **(B, C)** Representative current traces of F44V upon 10 μM ATP and voltage application. Voltage step pulses were applied during the current decay because there was no clear steady-state. **(D)** G-V relationship comparison between WT (dark blue) and F44V (red) for 10 μM ATP (n=3), which showed that this mutant was equally active at all recorded voltage and was far less sensitive to voltage than wildtype. Normalization was done based on the maximum conductance in the highest [ATP] (300 μM) for each construct. All error bars are ± s.e.m centered on the mean.

Fig. 21

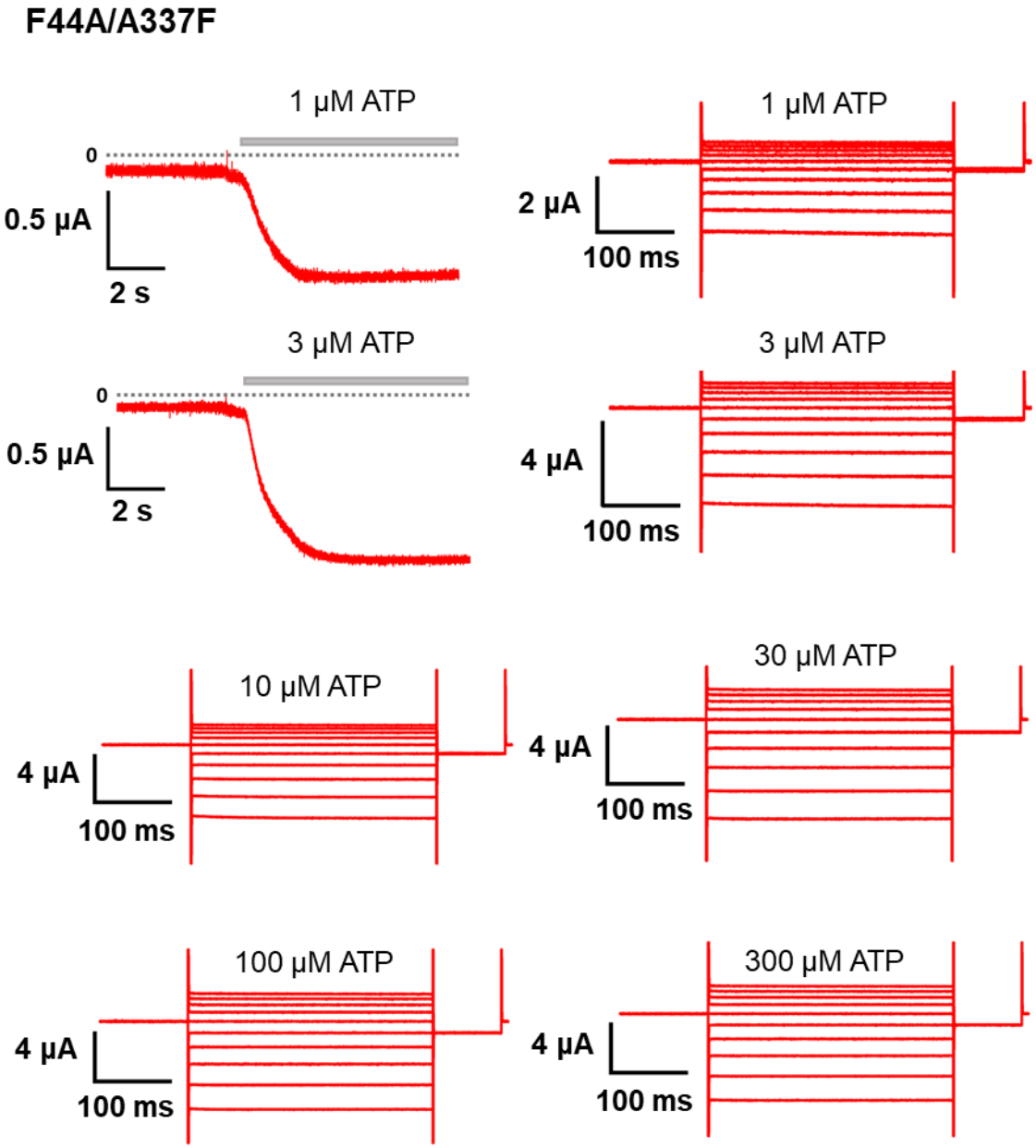
F44A/A337F
1 μM ATP
0
0.5 μA
2 s
1 μM ATP
2 μA
100 ms
3 μM ATP
0
0.5 μA
2 s
3 μM ATP
4 μA
100 ms
10 μM ATP
4 μA
100 ms
30 μM ATP
4 μA
100 ms
100 μM ATP
4 μA
100 ms
300 μM ATP
4 μA
100 ms

Fig. 21 Double mutation of F44A/A337F didn't rescue the wildtype phenotype of the receptor

Representative current traces of F44A/A337F upon various ATP application (1, 3, 10, 30, 100 300 μM) followed by voltage application at each concentration. The phenotype of F44A/A337F was similar to F44A and the wildtype phenotype couldn't be recovered by these double mutations. The double mutation showed no clear voltage-dependent gating, even though the mutant responded normally to the ATP application (n=3).

Fig. 22

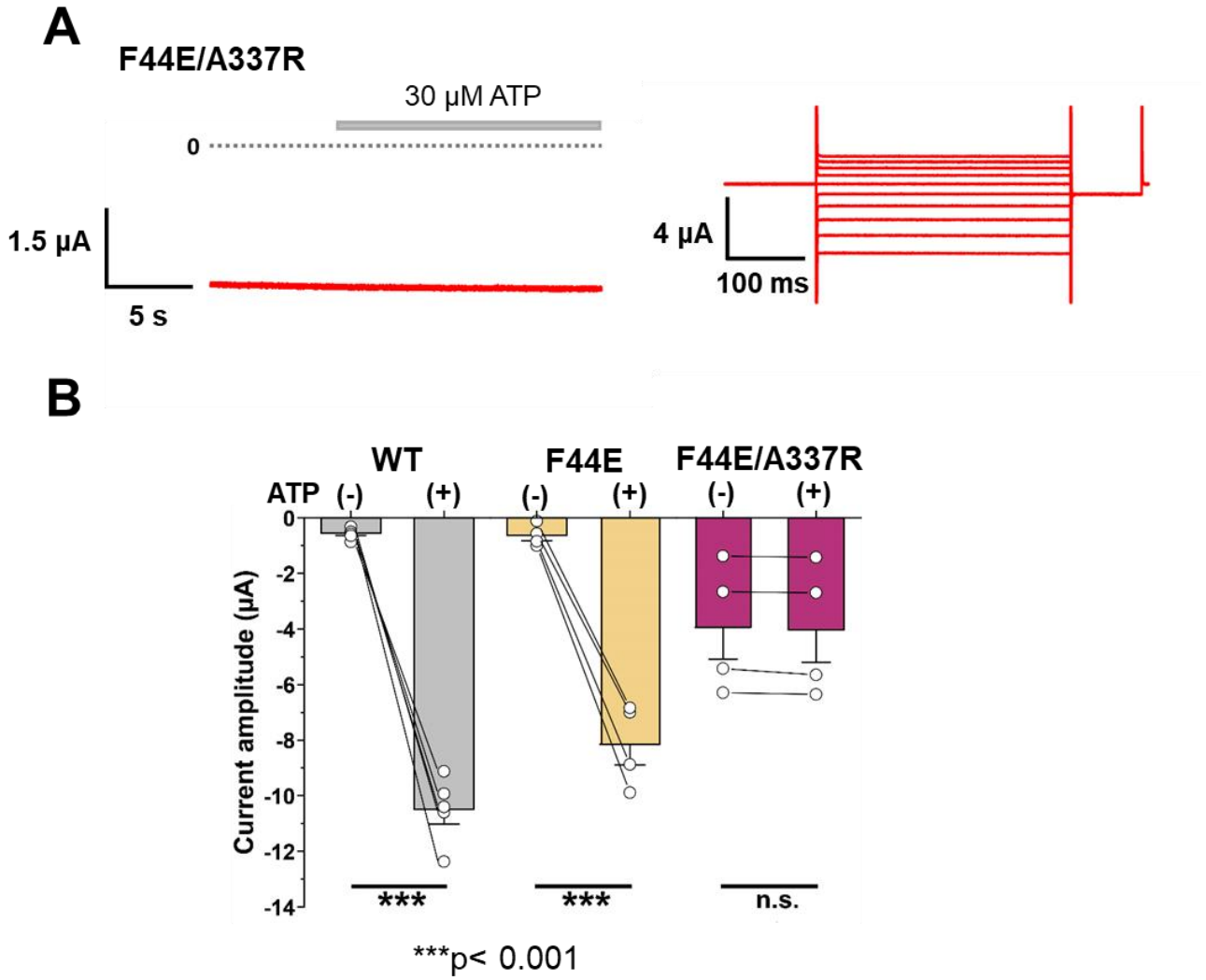
A
F44E/A337R
30 μM ATP
0
1.5 μA
5 s
4 μA
100 ms
B
WT
F44E
F44E/A337R
ATP (-) (+) (-) (+) (-) (+)
Current amplitude (μA)
0
-2
-4
-6
-8
-10
-12
-14
***
***
n.s.
***p< 0.001
C
Closed state
TM2
TM1
A337
F44
D
Open state
TM1
TM2
F44
A337

Fig. 22 Artificial electrostatic bridge introduced between A337 and F44 showed that the interaction is important for stabilizing the open state

(A) Representative current traces of F44E/A337R upon ATP and voltage application. **(B)** Comparison of current amplitude of WT, F44E, and F44E/A337R before and after ATP application (*** $p<0.001$, paired t-test, n=4). All error bars are ± s.e.m centered on the mean. **(C, D)** Side view structure of the position of F44 and A337 in the closed (C) and open (D) state, respectively. Paired electrostatically charged residues were introduced between A337 and F44, in order to see its effect. F44E/A337R already opened before ATP application and didn't give any response to ATP application. When the voltage step pulses were applied, it didn't show voltage dependent gating, but with a rectified permeation property.

Fig. 23

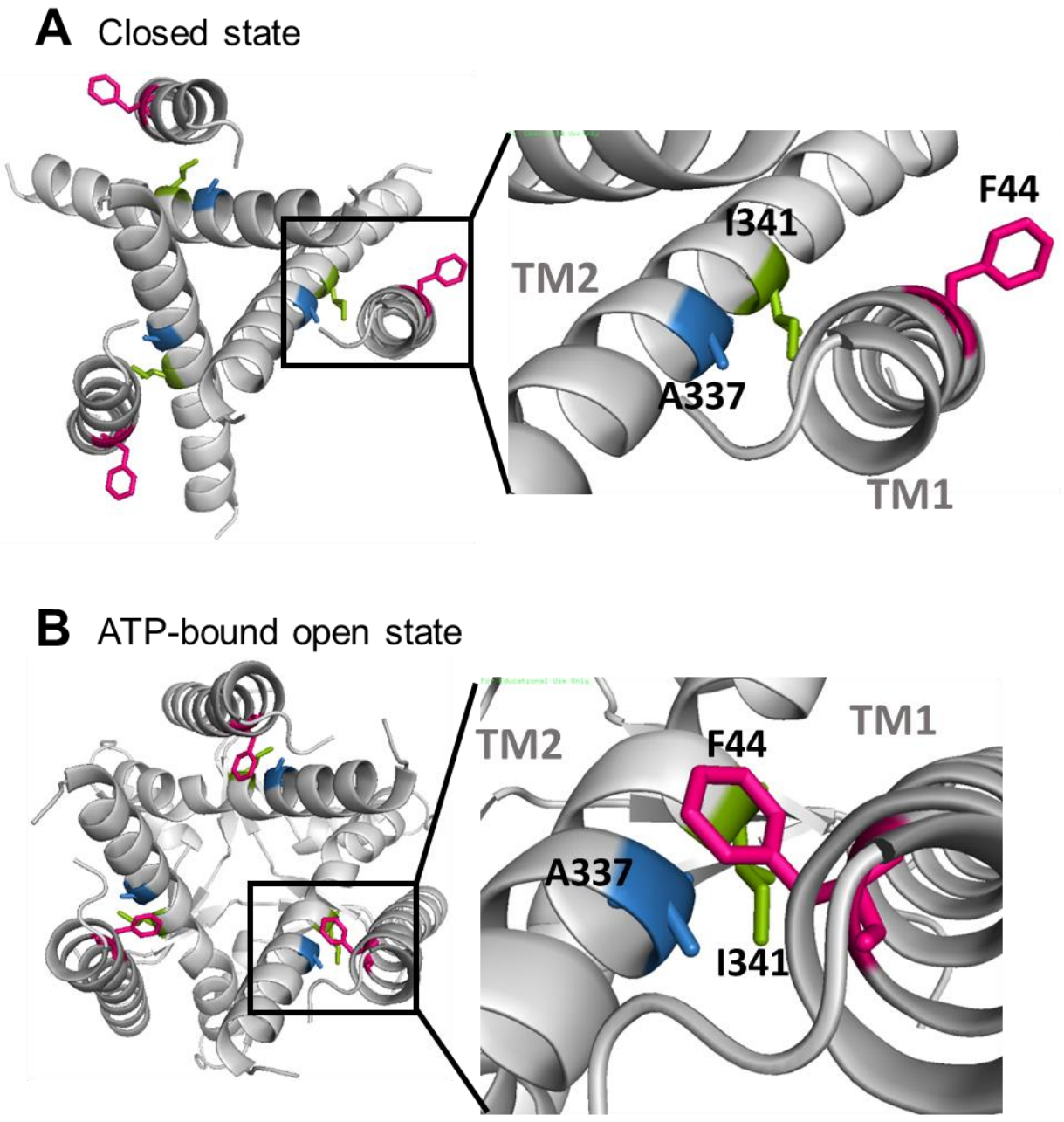
A Closed state
F44
I341
TM2
A337
TM1
B ATP-bound open state
TM2
TM1
F44
A337
I341
C
ATP
A337
I341
Lipid bilayer
Electric field lines

Fig. 23 Mechanisms of P2X2 receptor complex gating

(A, B) Top view structure of P2X2 receptor in the closed (A) and ATP-bound open state (B). Depicted are the proposed initiation mechanisms of P2X2 receptor complex gating as follows. (1) The electric convergence at A337 and I341 and (2) F44 which moves towards A337 in TM2 domain upon ATP binding (3) The interaction between A337 and F44 in the ATP-bound open state is thought to be under the influence of the converged electric field. **(C)** A schematic illustration of the focused electric field at A337 and I341. Ion permeation pathway is not depicted in this scheme.